



CMS-HIN-10-002

Measurement of the elliptic anisotropy of charged particles produced in PbPb collisions at $\sqrt{s_{NN}} = 2.76$ TeV

The CMS Collaboration*

Abstract

The anisotropy of the azimuthal distributions of charged particles produced in $\sqrt{s_{NN}} = 2.76$ TeV PbPb collisions is studied with the CMS experiment at the LHC. The elliptic anisotropy parameter, v_2 , defined as the second coefficient in a Fourier expansion of the particle invariant yields, is extracted using the event-plane method, two- and four-particle cumulants, and Lee–Yang zeros. The anisotropy is presented as a function of transverse momentum (p_T), pseudorapidity (η) over a broad kinematic range: $0.3 < p_T < 20$ GeV/ c , $|\eta| < 2.4$, and in 12 classes of collision centrality from 0 to 80%. The results are compared to those obtained at lower center-of-mass energies, and various scaling behaviors are examined. When scaled by the geometric eccentricity of the collision zone, the elliptic anisotropy is found to obey a universal scaling with the transverse particle density for different collision systems and center-of-mass energies.

Submitted to Physical Review C

*See Appendix A for the list of collaboration members

1 Introduction

The azimuthal anisotropy of emitted charged particles is an important feature of the hot, dense medium produced in heavy-ion collisions, and has contributed to the suggestion of a strongly coupled quark-gluon plasma (sQGP) being produced in nucleus-nucleus collisions at RHIC [1–5]. In noncentral collisions, the beam direction and the impact parameter vector define a reaction plane for each event. If the nucleon density within the nuclei is continuous, the initial nuclear overlap region is spatially asymmetric with an “almond-like” shape. In this approximation, the impact parameter determines uniquely the initial geometry of the collision, as illustrated in Fig. 1. In a more realistic description, where the position of the individual nucleons that participate in inelastic interactions is considered, the overlap region has a more irregular shape and the event-by-event orientation of the almond fluctuates around the reaction plane. Experimentally, the azimuthal distribution of the particles detected in the final state can be used to determine the “event plane” that contains both the beam direction and the azimuthal direction of maximum particle density. Strong rescattering of the partons in the initial state may lead to local thermal equilibrium and the build up of anisotropic pressure gradients, which drive a collective anisotropic expansion. The acceleration is greatest in the direction of the largest pressure gradient, i.e., along the short axis of the almond. This results in an anisotropic azimuthal distribution of the final-state hadrons. The anisotropy is quantified in terms of a Fourier expansion of the observed particle yields relative to the event-by-event orientation of the event plane [6]:

$$E \frac{d^3N}{d^3p} = \frac{d^3N}{p_T dp_T dy d\phi} = \frac{1}{2\pi} \frac{d^2N}{p_T dp_T dy} \left(1 + \sum_{n=1}^{\infty} 2v_n(p_T, y) \cos [n(\phi - \Psi)] \right), \quad (1)$$

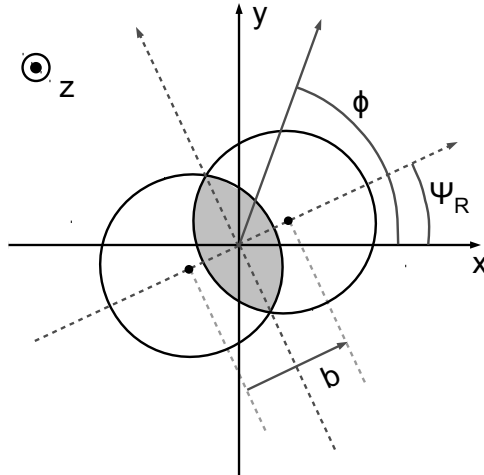


Figure 1: A schematic diagram of a noncentral nucleus-nucleus collision viewed in the plane orthogonal to the beam. The azimuthal angle ϕ , the impact parameter vector \mathbf{b} , and the reaction-plane angle Ψ_R are shown. The event-plane angle Ψ , with respect to which the flow is measured, fluctuates around the reaction-plane angle.

where ϕ , E , y , and p_T are the particle’s azimuthal angle, energy, rapidity, and transverse momentum, respectively, and Ψ is the event-plane angle. The second coefficient of the expansion,

often referred to as the “elliptic flow” strength, carries information about the early collision dynamics [7, 8]. The coefficients in the Fourier expansion may depend on p_T , rapidity, and impact parameter. Typically, the measurements are obtained for a particular class of events based on the centrality of the collisions, defined as a fraction of the total inelastic nucleus-nucleus cross section, with 0% denoting the most central collisions with impact parameter $b = 0$, and 100% the most peripheral collisions. Expressions similar to Eq. (1) can be written for the Fourier expansion of the yield integrated over p_T or rapidity:

$$\frac{d^2N}{dy d\varphi} = \frac{1}{2\pi} \frac{dN}{dy} \left(1 + \sum_{n=1}^{\infty} 2v_n(y) \cos [n(\varphi - \Psi)] \right), \quad (2)$$

and

$$\frac{d^2N}{p_T dp_T d\varphi} = \frac{1}{2\pi} \frac{dN}{p_T dp_T} \left(1 + \sum_{n=1}^{\infty} 2v_n(p_T) \cos [n(\varphi - \Psi)] \right). \quad (3)$$

The Fourier coefficients $v_n(y)$ and $v_n(p_T)$ can be obtained by directly analyzing the yields integrated over p_T or rapidity, or from the coefficients of the triple-differential invariant yield in Eq. (1), $v_n(p_T, y)$, by performing the following yield-weighted average over the ranges of transverse momentum Δp_T and rapidity Δy , from which the particles are taken:

$$v_n(y) = \frac{\int_{\Delta p_T} p_T dp_T \frac{d^2N}{p_T dp_T dy} v_n(p_T, y)}{\int_{\Delta p_T} p_T dp_T \frac{d^2N}{p_T dp_T dy}} \quad (4)$$

or

$$v_n(p_T) = \frac{\int_{\Delta y} dy \frac{d^2N}{p_T dp_T dy} v_n(p_T, y)}{\int_{\Delta y} dy \frac{d^2N}{p_T dp_T dy}}. \quad (5)$$

The coefficients of the Fourier expansion of the particles’ invariant yield integrated over a broad rapidity and p_T window, are often referred to as “integrated flow”:

$$\frac{dN}{d\varphi} = \frac{1}{2\pi} N \left(1 + \sum_{n=1}^{\infty} 2v_n \cos [n(\varphi - \Psi)] \right), \quad (6)$$

where

$$v_n = \frac{\int_{\Delta y} dy \int_{\Delta p_T} p_T dp_T \frac{d^2N}{p_T dp_T dy} v_n(p_T, y)}{\int_{\Delta y} dy \int_{\Delta p_T} p_T dp_T \frac{d^2N}{p_T dp_T dy}}. \quad (7)$$

In obtaining the Fourier coefficients, the absolute normalization in the particle yields is not important, as long as the particle detection efficiency is constant over the chosen transverse momentum and rapidity range. However, if the efficiency varies, the appropriate efficiency corrections need to be applied. This often leads to a two-step procedure in which first $v_n(p_T, y)$ is obtained in a narrow phase-space window where the efficiency is constant, and then a yield-weighted average is performed using Eqs. (4), (5), or (7), folding in the efficiency-corrected

particle spectra. When the particle mass is not determined in the measurement, the pseudorapidity $\eta = -\ln[\tan(\theta/2)]$, with θ being the polar angle, is used instead of the rapidity.

Elliptic flow has been measured at the AGS, SPS, and RHIC. A notable feature in these measurements is that the elliptic flow measured as a function of transverse momentum, $v_2(p_T)$, increases with the nucleon-nucleon center-of-mass energy ($\sqrt{s_{NN}}$) up to about 22 GeV [9, 10], and then saturates at a value compatible with predictions from ideal hydrodynamics [11, 12]. The most extensive experimental studies have been performed at the highest RHIC energy of $\sqrt{s_{NN}} = 200$ GeV in AuAu collisions [1–3]. First results from PbPb collisions at $\sqrt{s_{NN}} = 2.76$ TeV from the Large Hadron Collider (LHC) [13, 14] indicate that there is little or no change in the transverse momentum dependence of the elliptic flow measured at the highest RHIC energy and the LHC, despite the approximately 14-fold increase in the center-of-mass energy. Recent theoretical studies of elliptic flow have focused on quantifying the ratio of the shear viscosity to the entropy density of the produced medium assuming viscous hydrodynamics [15, 16], and taking into account a variety of possible initial conditions.

Based on experimental results and the corresponding theoretical descriptions of the data, the underlying physics processes that generate the elliptic anisotropy are thought to vary for different kinematic regions:

- **Elliptic flow in the bulk system**

Hadrons produced in soft processes, carrying low transverse momentum ($p_T \lesssim 2$ GeV/c for mesons, and $p_T \lesssim 3$ GeV/c for baryons [17–20]), exhibit azimuthal anisotropies that can be attributed to collective flow driven by the pressure gradients in the system. The description of elliptic flow is amenable to hydrodynamic calculations [12, 15, 21, 22]. Comparisons to theory indicate that the flow is primarily generated during an early stage of the system evolution.

- **Recombination region**

At intermediate transverse particle momentum ($2 \lesssim p_T \lesssim 4$ GeV/c), the RHIC data show that the elliptic anisotropies for various identified hadron species approximately follow a common behavior when both the $v_2(p_T)$ value and the p_T of the particle are divided by the number of valence quarks in the hadron [17, 18, 23]. This behavior is successfully reproduced by models invoking quark recombination as the dominant hadronization mechanism in this momentum range [24–26]. The quark-number scaling of the elliptic flow has been interpreted as evidence that quark degrees of freedom dominate in the early stages of heavy-ion collisions, when the collective flow develops [27]. The quark recombination may involve both thermally produced quarks and quarks originating in jet fragmentation. Therefore, the elliptic anisotropy in the recombination region results from an interplay between the bulk flow of the system and the azimuthal anisotropy in hadron production induced by jet quenching.

- **Jet-fragmentation region**

At intermediate and high transverse momentum ($p_T \gtrsim 3$ GeV/c), where fragments from increasingly harder partons begin to contribute to the particle spectra, anisotropy in the azimuthal distributions may be generated from the stronger jet quenching in the direction of the long axis of the almond-shaped reaction zone [28–31]. It is expected that this mechanism will dominate the elliptic anisotropy of hadrons with momenta in excess of 8 GeV/c. Thus, measurements extending beyond this p_T range carry information about the path-length dependence of energy loss in the produced medium.

The measurements presented in this paper span the transverse momentum range of $0.3 < p_T < 20 \text{ GeV}/c$ and provide the basis for comparisons to theoretical descriptions of the bulk properties of the system and the quenching of jets. Such comparisons may give insight in determining the transport properties of sQGP, namely: the shear viscosity, and the opacity of the plasma. The theoretical interpretation of the elliptic anisotropy in the recombination region requires identified-hadron measurements that are not included in this analysis.

In ideal hydrodynamics, the integrated elliptic flow is directly proportional to the initial spatial eccentricity of the overlap zone [32]. There are many factors that can change this behavior, including viscosity in the sQGP and the hadronic stages of the system evolution, incomplete thermalization in peripheral collisions, and variations in the equation-of-state. Event-by-event fluctuations in the overlap zone [33–38] could also influence the experimental results, depending on the method that is used to extract the v_2 signal. Invoking multiple methods with different sensitivities to the initial-state fluctuations is important for disentangling the variety of physics processes that affect the centrality dependence of the elliptic flow. Comparisons to results from lower-energy measurements and explorations of empirical scaling behaviors could provide additional insights into the nature of the matter produced in high-energy heavy-ion collisions.

The pseudorapidity dependence of the elliptic flow, $v_2(\eta)$, provides information on the initial state and the early-time development of the collision, constraining the theoretical models and the description of the longitudinal dynamics in the collisions [39, 40]. Longitudinal scaling in $v_2(\eta)$ extending over several units of pseudorapidity (extended longitudinal scaling) has been reported at RHIC [41] for a broad range of collision energies ($\sqrt{s_{NN}} = 19.6\text{--}200 \text{ GeV}$). Studies of the evolution of $v_2(\eta)$ from RHIC to LHC energies may have implications for the unified description of sQGP in both energy regimes.

The paper is organized as follows: Section 2 gives the experimental details of the measurement including the Compact Muon Solenoid (CMS) detector, triggering and event selection, centrality determination, Glauber-model calculations, reconstruction of the charged-particle transverse momentum spectra, methods of measuring the elliptic anisotropy, and the studies of the systematic uncertainties. In Section 3 we present results of v_2 as a function of transverse momentum, centrality, and pseudorapidity, and the measurement of the charged-particle transverse momentum spectra. The elliptic flow results are obtained with the event-plane method [6], two- and four-particle cumulants [42], and Lee–Yang zeros [43, 44]. The analysis is performed in 12 classes of collision centrality covering the most central 80% of inelastic collisions. We study the eccentricity scaling of v_2 , and investigate the differences in the results obtained from different methods, taking into account their sensitivity to initial-state fluctuations. Section 4 is devoted to detailed comparisons with results obtained by other experiments at lower energies and the exploration of different scaling behaviors of the elliptic flow. The results of our studies are summarized in Section 5.

2 Experimental method

2.1 CMS detector

The central feature of the CMS apparatus is a superconducting solenoid of 6 m internal diameter, providing a 3.8 T field. Within the field volume are a silicon tracker, a crystal electromagnetic calorimeter, and a brass/scintillator hadron calorimeter. Muons are measured in gas-ionization detectors embedded in the steel return yoke. In addition to these detectors, CMS has extensive forward calorimetry. The inner tracker measures charged particles within

the pseudorapidity range $|\eta| < 2.5$, and consists of silicon pixel and silicon strip detector modules. The beam scintillation counters (BSC) are a series of scintillator tiles which are sensitive to almost the full PbPb interaction cross section. These tiles are placed along the beam line at a distance of ± 10.9 m and ± 14.4 m from the interaction point, and can be used to provide minimum-bias triggers. The forward hadron calorimeter (HF) consists of a steel absorber structure that is composed of grooved plates with quartz fibers inserted into these grooves. The HF calorimeters have a cylindrical shape and are placed at a distance of 11.2 m from the interaction point, covering the pseudorapidity range of $2.9 < |\eta| < 5.2$. A more detailed description of the CMS detector can be found elsewhere [45].

The detector coordinate system has the origin centered at the nominal collision point inside the experiment, with the y axis pointing vertically upward, the x axis pointing radially inward towards the center of the LHC ring, and the z axis pointing along the counterclockwise beam direction.

2.2 Event selection

The measurements presented are performed by analyzing PbPb collision events recorded by the CMS detector in 2010. From these data, the minimum-bias event sample is collected using coincidences between the trigger signals from both the $+z$ and $-z$ sides of either the BSC or HF. The minimum-bias trigger used for this analysis is required to be in coincidence with the presence of both colliding ion bunches in the interaction region. This requirement suppresses noncollision-related noise, cosmic rays, and beam backgrounds (beam halo and beam-gas collisions). The total hadronic collision rate varied between 1 and 210 Hz, depending on the number of colliding bunches and the bunch intensity.

In order to obtain a pure sample of inelastic hadronic collisions, several offline selections are applied to the triggered event sample. These selections remove contamination from noncollision beam backgrounds and from ultraperipheral collisions (UPC) that lead to an electromagnetic breakup of one or both of the Pb nuclei [46]. First, beam-halo events are vetoed based on the BSC timing. Then, to remove UPC and beam-gas events, an offline HF coincidence of at least three towers on each side of the interaction point is required, with a total deposited energy of at least 3 GeV in each tower. A reconstructed primary vertex made of at least two tracks and consistent with the nominal interaction point position is required. To further reject beam-gas and beam-halo events, the pixel clusters are required to have a length along the beam direction compatible with being produced by particles originating from the primary vertex, as for the study in [47]. Additionally, a small number of noisy events with uncharacteristic hadron calorimeter responses are removed.

The acceptance of the silicon tracker for $|\eta| > 0.8$ is found to vary significantly with respect to the longitudinal position of the collision point relative to the geometric center of the detector. This event-by-event variance in the tracking efficiency contributes to a systematic bias of the elliptic flow measurements at forward pseudorapidity. In order to remove this bias, events in this analysis are required to have a longitudinal vertex position within 10 cm of the geometric center of the detector. After all selections, 22.6 million minimum-bias events, corresponding to an integrated luminosity of approximately $3 \mu\text{b}^{-1}$, remain in the final sample.

2.3 Centrality determination and Glauber model calculations

In this analysis, the observable used to determine centrality is the total energy in both HF calorimeters. The distribution of this total energy is used to divide the event sample into 40 centrality bins, each representing 2.5% of the total nucleus-nucleus interaction cross section. The

events are then regrouped to form 12 centrality classes used in the analysis: 0–5% (most central), 5–10%, 10–15%, 15–20%, 20–25%, 25–30%, 30–35%, 35–40%, 40–50%, 50–60%, 60–70%, and 70–80% (see Table 1). Using Monte Carlo (MC) simulations, it is estimated that the minimum-bias trigger and the event selections include $(97 \pm 3)\%$ of the total inelastic cross section. For the events included in this analysis (0–80% centrality), the trigger is fully efficient.

For each group of events that comprises a centrality class, we evaluate a set of quantities that characterize the initial geometry of the collisions using a MC Glauber model. The Glauber model is a multiple-collision model that treats a nucleus-nucleus collision as an independent sequence of nucleon-nucleon collisions (see Ref. [48] and references therein). The nucleons that participate in inelastic interactions are called “participants”. A schematic view of a PbPb collision with an impact parameter $b = 6$ fm, as obtained from the Glauber model, is shown in Fig. 2. The direction and the magnitude of the impact parameter vector and the corresponding reaction-plane angle Ψ_R , are the same as in Fig. 1. However, the initial interaction zone as determined by the spatial distribution of the participants (filled circles) is no longer regular in shape and is not necessarily symmetric with respect to the reaction plane. In each event one can evaluate the variances σ_x^2 and σ_y^2 , and the covariance $\sigma_{xy} = \langle xy \rangle - \langle x \rangle \langle y \rangle$ of the participant distributions projected on the x and y axes. One can then find a frame $x'-y'$ that minimizes $\sigma_{x'y'}$, and define a “participant plane” using the beam direction and the x' axis [34, 49]. In this frame, the covariance $\sigma_{x'y'}$ of the participant spatial distribution vanishes. To characterize the geometry of the initial state of the collision, we define [34, 49] the eccentricity of the participant zone ϵ_{part} , its cumulant moments $\epsilon\{2\}$ and $\epsilon\{4\}$, and the transverse overlap area of the two nuclei S :

$$\epsilon_{\text{part}} \equiv \frac{\sigma_y^2 - \sigma_x^2}{\sigma_y^2 + \sigma_x^2} = \frac{\sqrt{(\sigma_y^2 - \sigma_x^2)^2 + 4\sigma_{xy}^2}}{\sigma_y^2 + \sigma_x^2}, \quad (8)$$

$$\epsilon\{2\}^2 \equiv \langle \epsilon_{\text{part}}^2 \rangle, \quad (9)$$

$$\epsilon\{4\}^4 \equiv 2\langle \epsilon_{\text{part}}^2 \rangle^2 - \langle \epsilon_{\text{part}}^4 \rangle, \text{ and} \quad (10)$$

$$S \equiv \pi\sigma_{x'}\sigma_{y'} = \pi\sqrt{\sigma_x^2\sigma_y^2 - \sigma_{xy}^2}. \quad (11)$$

In Eqs. (9) and (10), the average is taken over many events from the same centrality interval.

To implement the Glauber model for PbPb collisions at $\sqrt{s_{NN}} = 2.76$ TeV, we utilize the foundation of a published Glauber MC software package TGLAUBERMC [50], which was developed for the PHOBOS Collaboration at RHIC. Standard parameters of the Woods-Saxon function used for modeling the distribution of nucleons in the Pb nuclei are taken from Ref. [51]. The nucleon-nucleon inelastic cross section, which is used to determine how close the nucleon trajectories need to be in order for an interaction to occur, is taken as 64 ± 5 mb, based on a fit of the existing data for total and elastic cross sections in proton-proton and proton-antiproton collisions [52]. The uncertainties in the parameters involved in these calculations contribute to the systematic uncertainty in N_{part} , S , and ϵ_{part} for a given centrality bin. The connection between the experimentally defined centrality classes using the HF energy distribution and N_{part} from the Glauber model is obtained [53] from fully simulated and reconstructed MC events generated with the AMPT [54] event generator. The calculated Glauber model variables for each centrality class are shown in Table 1.

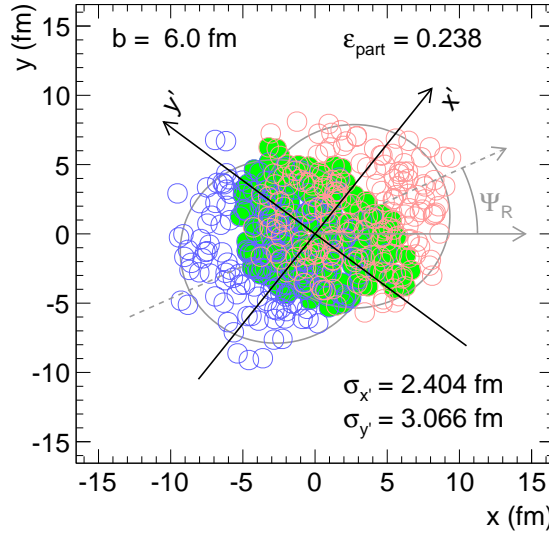


Figure 2: (Color online) A schematic view of a PbPb collision with an impact parameter $b = 6$ fm as obtained from the Glauber model. The nucleons that participate in inelastic interactions are marked with filled circles. The x and y coordinates represent the laboratory frame, while x' and y' represent the frame that is aligned with the axes of the ellipse in the participant zone. The participant eccentricity ϵ_{part} and the standard deviations of the participant spatial distribution $\sigma_{y'}$ and $\sigma_{x'}$ from which the transverse overlap area of the two nuclei is calculated are also shown. The angle Ψ_R denotes the orientation of the reaction plane.

2.4 Reconstruction of the charged-particle transverse momentum distributions and the mean transverse momentum

To determine the transverse momentum distributions of the charged particles produced in the collisions, we first need to reconstruct the particles' trajectories ("tracks") through the 3.8 T solenoidal magnetic field. The tracks are reconstructed by starting with a "seed" comprising two or three reconstructed signals ("hits") in the inner layers of the silicon strip and pixel detectors that are compatible with a helical trajectory of some minimum p_T and a selected region around the reconstructed primary vertex or nominal interaction point. This seed is then propagated outward through subsequent layers using a combinatorial Kalman-filter algorithm. Tracking is generally performed in multiple iterations, varying the layers used in the seeding and the parameters used in the pattern recognition, and removing duplicate tracks between iterations. This algorithm is described in detail in Ref. [55]. The algorithm used in most of the CMS proton-proton analyses, as well as the tracking detector performance for the 2010 run, are described in Ref. [56].

The six-iteration process used in proton-proton collisions is computationally not feasible in the high-multiplicity environment of very central PbPb collisions. In place of this, a simple two-iteration process is used. The first iteration builds seeds from hits in some combination of three layers in the barrel and endcap pixel detectors compatible with a trajectory of $p_T > 0.9$ GeV/ c and a distance of closest approach to the reconstructed vertex of no more than 0.1 cm in the transverse plane and 0.2 cm longitudinally. These tracks are then filtered using selection criteria based on a minimum number of reconstructed hits, vertex compatibility along the longitudinal direction and in the transverse plane, and low relative uncertainty on the reconstructed momentum.

Table 1: For the centrality bins used in the analysis, the average values of the number of participating nucleons, transverse overlap area of the two nuclei, participant eccentricity, and cumulant moments of the participant eccentricity, along with their systematic uncertainties from the Glauber model.

Centrality	$\langle N_{\text{part}} \rangle$	$\langle S \rangle [\text{fm}^2]$	$\langle \epsilon_{\text{part}} \rangle$	$\epsilon\{2\}$	$\epsilon\{4\}$
0–5%	381 ± 2	29.4 ± 1.2	0.074 ± 0.003	0.084 ± 0.003	0.053 ± 0.002
5–10%	329 ± 3	26.6 ± 1.1	0.111 ± 0.005	0.128 ± 0.005	0.060 ± 0.003
10–15%	283 ± 3	24.0 ± 1.0	0.154 ± 0.007	0.175 ± 0.007	0.122 ± 0.005
15–20%	240 ± 3	21.6 ± 1.0	0.198 ± 0.009	0.219 ± 0.009	0.171 ± 0.007
20–25%	204 ± 3	19.5 ± 0.9	0.238 ± 0.009	0.262 ± 0.010	0.214 ± 0.008
25–30%	171 ± 3	17.5 ± 0.8	0.276 ± 0.010	0.302 ± 0.012	0.253 ± 0.010
30–35%	143 ± 3	15.7 ± 0.8	0.312 ± 0.011	0.339 ± 0.012	0.288 ± 0.010
35–40%	118 ± 3	14.1 ± 0.7	0.346 ± 0.010	0.375 ± 0.011	0.322 ± 0.009
40–50%	86.2 ± 2.8	12.0 ± 0.6	0.395 ± 0.010	0.429 ± 0.011	0.370 ± 0.010
50–60%	53.5 ± 2.5	9.4 ± 0.5	0.465 ± 0.008	0.501 ± 0.009	0.437 ± 0.007
60–70%	30.5 ± 1.8	7.1 ± 0.4	0.543 ± 0.011	0.581 ± 0.012	0.514 ± 0.010
70–80%	15.7 ± 1.1	4.8 ± 0.3	0.630 ± 0.016	0.662 ± 0.017	0.598 ± 0.015

In the second iteration, seeding is also performed using three layers of the pixel detector, but the minimum transverse momentum requirement is relaxed to $p_T > 0.2 \text{ GeV}/c$. These tracks are not propagated through the silicon-strip detector, but simply refitted using the transverse position of the beam spot as an additional constraint. These pixel-only tracks are then filtered using selection criteria of vertex compatibility along the longitudinal axis and statistical goodness of fit.

The tracks from both collections are checked for duplicate tracks using the number of hits in common between the two tracks, and duplicates are removed giving preference to the first-iteration tracks. The tracking algorithm may sometimes misidentify tracks by combining silicon detector signals that do not originate from the same charged particle. It is important to keep the proportion of misidentified tracks (referred to as “fake tracks”), or fake rate, as low as possible. To create the final collection, first-iteration tracks with $p_T > 1.5 \text{ GeV}/c$ are combined with second-iteration pixel-only tracks with $p_T < 1.8 \text{ GeV}/c$. These p_T limits were chosen to exclude kinematic regions where a given iteration has a high fake rate. The efficiency and fake rate of this modified tracking collection are found both by using a full MC simulation of PbPb collisions based on the HYDJET event generator [57] and by embedding simulated charged pions into PbPb data events. The efficiency, fake rate, and momentum resolution of this final collection determined by the simulated events from the HYDJET event generator are shown in Fig. 3 for events of five different centrality classes. The abrupt change in efficiency, fake rate, and momentum resolution seen in the figure occurs at the transverse momentum where the two track collections are merged.

The charged-particle transverse momentum distributions are corrected for the loss of acceptance, efficiency, and the contributions from fake tracks. Each detected track is weighted by a factor w_{tr} according to its centrality, transverse momentum, and pseudorapidity:

$$w_{tr}(\text{centrality}, p_T, \eta) = \frac{1 - f}{e}. \quad (12)$$

Here f is the fraction of fake tracks that do not correspond to any charged particle, and e is the absolute tracking efficiency accounting for both geometric detector acceptance and algorithm-

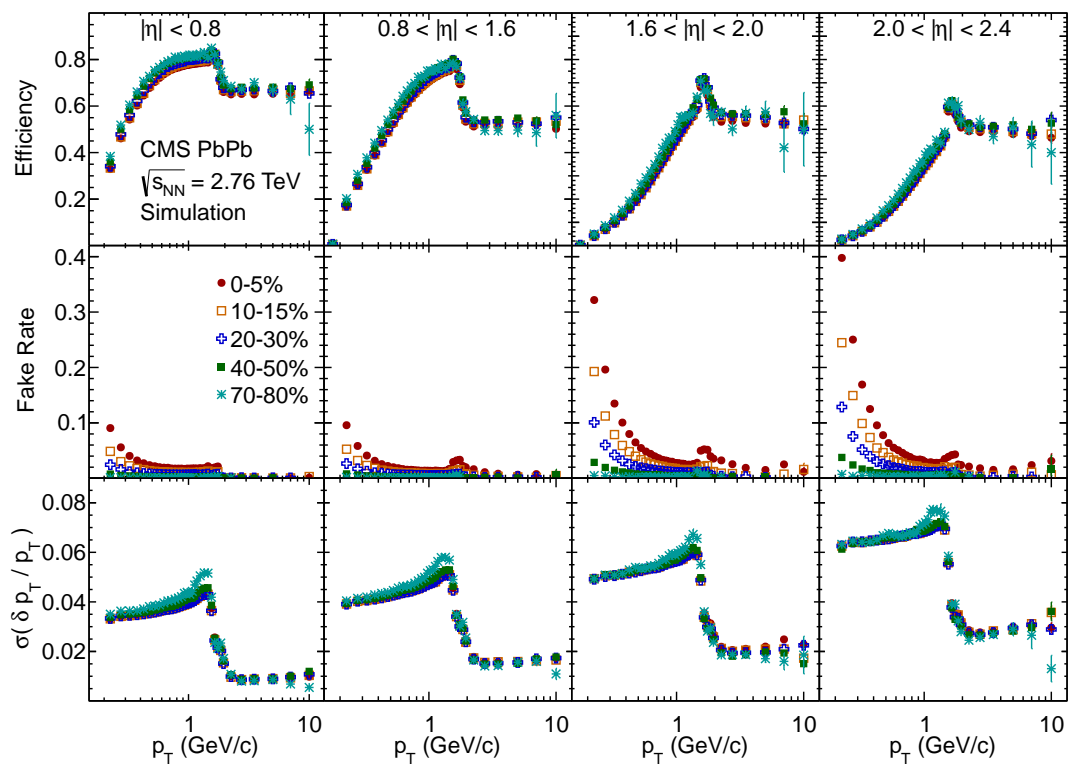


Figure 3: (Color online) Efficiency (top), fake rate (middle), and momentum resolution (bottom) of charged tracks obtained from HYDJET simulated events in four pseudorapidity regions: $|\eta| < 0.8$, $0.8 < |\eta| < 1.6$, $1.6 < |\eta| < 2.0$, and $2.0 < |\eta| < 2.4$ displayed from left to right, and for the five centrality classes given in the legend.

mic tracking efficiency. The proportion of multiply reconstructed particles and reconstructed particles from secondary decays is negligible and is not included in the correction factor. The fully corrected transverse momentum distributions are measured in 12 centrality classes over the pseudorapidity range $|\eta| < 2.4$ in bins of $\Delta\eta = 0.4$, as discussed in Section 3.4. These distributions are used in obtaining integrated v_2 values. We also study the evolution of $\langle p_T \rangle$ with pseudorapidity and centrality (Section 3.4), and center-of-mass energy (Section 4).

To evaluate $\langle p_T \rangle$, the spectra need to be extrapolated down to $p_T = 0$ GeV/ c . The extrapolation is performed using a Tsallis distribution [58–60]:

$$E \frac{d^3 N_{\text{ch}}}{dp^3} = \frac{1}{2\pi p_T} \frac{E}{p} \frac{d^2 N_{\text{ch}}}{d\eta dp_T} = C \left(1 + \frac{E_T}{nT} \right)^{-n}, \quad (13)$$

where $E_T = \sqrt{m^2 + p_T^2} - m$, and m is taken to be the charged pion mass. The measured spectra are fitted in the range $0.3 < p_T < 3.0$ GeV/ c , and the fit parameters C , n , and T are determined. The mean transverse momentum is then evaluated using the fit function in the extrapolation region of $0 \leq p_T < 0.3$ GeV/ c , and the data from the range $0.3 \leq p_T \leq 6.0$ GeV/ c . This method has been previously applied in CMS [47] in the measurement of $\langle p_T \rangle$ in pp collisions at $\sqrt{s} = 7$ TeV.

2.5 Methods for measuring the anisotropy parameter v_2

Anisotropic flow aims to measure the azimuthal correlations of the particles produced in heavy-ion collisions in relation to the initial geometry of the collisions. Originally, the flow was defined as a correlation of the particle emission angles with the reaction plane [6, 7]. More recently, it was recognized [34, 49] that the initial geometry is better characterized by the positions of the individual nucleons that participate in inelastic interactions, and thus define a participant plane that fluctuates around the reaction plane on an event-by-event basis. Neither the reaction plane nor the participant plane are directly measurable experimentally. Instead, there are several experimental methods that have been developed to evaluate the anisotropic flow based on the final-state particle distributions. In the present analysis, we use the event-plane method, two-particle and four-particle cumulants [42], and the Lee–Yang zeros method [43, 44] the last of which is based on correlations involving all the particles in the event.

The anisotropic flow measurements are affected by fluctuations that come from several sources. Statistical fluctuations arise due to the fact that a finite number of particles is used to determine a reference plane for the flow and the multiplicity fluctuations within the chosen centrality interval. The effect of these fluctuations is to reduce the measured flow signal and is largely compensated for by the resolution corrections described below. Any remaining effects from statistical fluctuations on our measurements are included in the systematic uncertainties (see Section 2.7). Another more important source of fluctuations comes from the event-by-event fluctuations in the participant eccentricity that are present even at fixed N_{part} . These dynamical fluctuations have been shown [34–38] to affect the various methods for estimating the flow differently, since each of them is based on a different moment of the final-particle momentum distribution. For example, the two-particle cumulant method measures an r.m.s. value of the flow that is higher than the mean value. Conversely, the four-particle cumulant and other multiparticle correlation methods return a value that is lower than the mean value. For the event-plane method, the results vary between the mean and the r.m.s. value depending on the event-plane resolution, which varies in each centrality interval.

In addition, there exist other sources of correlations in azimuth, such as those from resonance

decays, jets, and Bose–Einstein correlations between identical particles. These correlations, which are not related to the participant plane, are called nonflow correlations. The various methods proposed to estimate the magnitude of anisotropic flow have different sensitivities to the nonflow correlations, thus allowing systematic checks on the flow measurements. The multiparticle correlation methods are least affected by nonflow correlations, but they do not work reliably when either the flow anisotropy (v_2) or the multiplicity in the selected phase-space window is small. This happens in the most central and in the most peripheral events [42, 43]. Thus, the two-particle cumulant and the event-plane methods provide an extended centrality range, albeit with a larger nonflow contribution.

All four methods used here have been extensively studied and applied in different experiments. Thus, we limit our description in the following subsections only to the features that are specific for our implementations of these methods.

2.5.1 Event-plane method

The event-plane method estimates the magnitude of anisotropic flow by reconstructing an “event-plane” containing both the beam direction and the direction of the maximal flow determined from the azimuthal distributions of the final-state particles. Under the assumption that the flow is driven by the initial-state asymmetry in the nuclear overlap zone, and that there are no other sources of azimuthal correlations in the final-state particles, the event-plane is expected to coincide with the participant plane [34] defined in Fig. 2. Recent theoretical calculations [38, 61–63] confirm that the event plane and the participant plane are strongly correlated event by event. Since the event plane is determined using a finite number of particles, and detected with finite angular resolution, the measured event-plane angle fluctuates about its true value. As a result, the observed particle azimuthal anisotropy with respect to the event-plane is smeared compared to its true value. The true elliptic flow coefficient v_2 in the event-plane method is evaluated by dividing the observed v_2^{obs} value by a resolution correction factor, R , which accounts for the event-plane resolution.

To determine the event-plane resolution correction, a technique that sorts the particles from each event into three subevents based on their pseudorapidity values [6] is used. For subevents A, B, C in three different pseudorapidity windows, the event-plane resolution correction factor R_A for subevent A is found as:

$$R_A = \sqrt{\frac{\langle \cos[2(\Psi^A - \Psi^B)] \rangle \langle \cos[2(\Psi^A - \Psi^C)] \rangle}{\langle \cos[2(\Psi^B - \Psi^C)] \rangle}}, \quad (14)$$

where Ψ^A, Ψ^B , and Ψ^C are the event-plane angles determined from the corresponding subevents, and the average is over all events in a selected centrality class used in the v_2 analysis.

In our implementation of the method, the event-plane angle determined for the subevent furthest in η from the track being used in the elliptic flow analysis is used, and the corresponding resolution correction is employed. This selection minimizes the contributions of auto-correlations and other nonflow effects that arise if the particles used in the event-plane determination and those used in the flow analysis are close in phase space.

To achieve the largest pseudorapidity gap possible, two event planes are defined, with calorimeter data covering the pseudorapidity ranges of $-5 < \eta < -3$ and $3 < \eta < 5$, labeled “HF-” and “HF+”, respectively. These pseudorapidity ranges are primarily within the coverage of the HF calorimeters. A third event plane, found using charged particles detected in the tracker in the pseudorapidity range $-0.8 < \eta < 0.8$, is also defined and used in the three-subevent

technique for determining the resolution corrections for HF^- and HF^+ . The resulting resolution corrections are presented in Fig. 4. Particles detected in the tracker with $\eta > 0$ are then correlated with the HF^- event plane, and those with $\eta < 0$ with the HF^+ plane. In this manner, the minimum pseudorapidity gap between particles used in the event-plane determination and those for which the v_2 signal is measured is 3 units. A two-subevent technique based on HF^- and HF^+ , with a resolution parameter defined as $R_{A/B} = \sqrt{\langle \cos[2(\Psi^A - \Psi^B)] \rangle}$, is also implemented and used for systematic studies. The values of $R_{A/B}$ are shown for comparison in Fig. 4.

A standard flattening procedure [64] using a Fourier decomposition of the distribution of the event-plane angles to 21st order is used to shift the event-by-event plane angle to correct for asymmetries in the event-plane distribution that arise from the detector acceptance and other instrumental effects. Although most of these effects are already accounted for with a correction involving just the first four coefficients in the expansion, the larger order was used for data quality monitoring purposes. For each centrality class in the analysis, the flattening parameters are calculated by grouping events according to the longitudinal location of their primary collision vertex in 5 cm-wide bins.

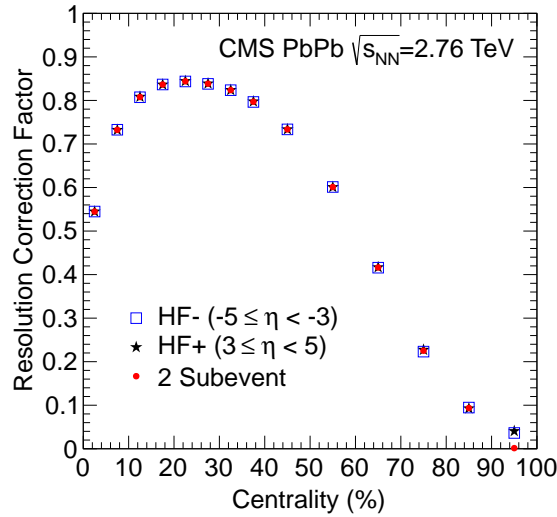


Figure 4: (Color online) Event-plane resolution correction factors as a function of centrality for the two event-planes (HF^- and HF^+) used in determining the elliptic anisotropy parameter v_2 . The corrections determined with the three-subevent method used in the analysis are shown as open squares and star symbols. The results from a two-subevent method used in evaluating the systematic uncertainties are shown as filled circles, though they overlap the other points in all but the most peripheral bin.

2.5.2 Cumulant method

The cumulant method measures flow utilizing a cumulant expansion of multiparticle azimuthal correlations, without determining the orientation of the event plane. The idea is that if the particles are correlated with the event-plane orientation, then there also exist correlations between them. In our analysis, we utilize two- and four-particle correlations. To calculate the cumulants of these correlations, from which the flow coefficient is extracted, we use a generating function of the multiparticle correlations in a complex plane [42]. First, we evaluate the “integrated”, or

reference, flow by constructing the corresponding generating function including all particles from a broad (p_T, η) window, and averaging over the events in a given centrality class. The reference flow may not be corrected for tracking efficiency and should not be equated with the fully corrected integrated flow of the events. Then, the differential flow, i.e., the flow in a narrower phase-space window, either in p_T or η , is measured with respect to the reference flow. In the cumulant and Lee–Yang zeros methods, the reference flow serves the same purpose as the determination of the event-plane angle and the resolution correction factors in the event-plane method. In our analysis of $v_2(p_T)$, the p_T and η ranges for the reference flow are $0.3 < p_T < 3 \text{ GeV}/c$ and $|\eta| < 0.8$, respectively. In the analysis of $v_2(\eta)$, the reference flow is obtained for the range $0.3 < p_T < 3 \text{ GeV}/c$ and $|\eta| < 2.4$ in order to maximize the resolution parameter, which improves as the charged hadron multiplicity M in the selected phase-space window increases. The transverse momentum restriction of $p_T < 3 \text{ GeV}/c$ is imposed to limit the contributions from hadrons originating in jets, and thus reduce the nonflow correlations contributing to the measured elliptic anisotropy parameter. To avoid auto-correlations, the particles used for determining differential flow are not included in evaluating the reference flow. The generating function for the reference flow is calculated at several different points in the complex plane, and we then interpolate between these points. We use three values for the radius parameter, r_0 , and seven values for the polar angle, as described in Ref. [42]. The radius parameters are determined according to the detected charged particle multiplicity and the number of events analyzed in each centrality class. Each particle in the differential p_T or η bin is correlated to the particles used for the reference flow through a differential generating function. To account for the fact that the track reconstruction efficiency may vary across the chosen bin, we implement an efficiency correction that is applied as a track-by-track weight in the construction of the differential generating function.

2.5.3 Lee–Yang zeros method

The Lee–Yang zeros (LYZ) method [43, 44] for directly measuring the flow is based on multiparticle correlations involving all particles in the event. It uses the asymptotic behavior of the cumulant expansion to relate the location of the zeros of a complex function to the magnitude of the integrated flow in the system. For a detector with a uniform detection efficiency for all particles in the chosen η and p_T window, it is thus possible to obtain the integrated flow in a simple one-step procedure. Since this is not the case for the CMS measurements presented here, we replace the term “integrated flow” that is used in the literature describing the method [43, 44] with “reference flow”. In the generating function (i.e., $G^\theta(ir)$, where r is the imaginary axis coordinate), the flow vector, constructed from all particles in the event, is projected onto a direction that makes an arbitrary angle θ with respect to the x axis. We use five different projection angles and then average the results over events from the same centrality class to reduce the statistical uncertainties. Subsequently, the minimum of the generating function is found, and the differential flow is determined with respect to the reference flow. There are different ways to define the generating function that involve either a sum or a product of the individual particle contributions. An example is given in Fig. 5, showing how the minimum of the generating function is determined using both definitions. The results presented here are based on the product generating function. In our analysis of $v_2(p_T)$, the p_T and η ranges for the reference flow are $0.3 < p_T < 12 \text{ GeV}/c$ and $|\eta| < 0.8$, respectively. Since the Lee–Yang zeros method is less sensitive to jet-induced charged-particle correlations than the two-particle cumulant method, the p_T range of the tracks included in the determination of the reference flow is not restricted to low p_T . In the analysis of $v_2(\eta)$, the pseudorapidity range for the particles included in the reference flow is extended to $|\eta| < 2.4$.

The Lee–Yang zeros method is sensitive to multiplicity fluctuations. To evaluate the effects of

these fluctuations we perform a toy-model MC study. Event ensembles are generated sampling the multiplicity for each event from Gaussian distributions with mean and r.m.s. values comparable to the ones measured in the centrality bins used in the measurement. For each particle, the corresponding p_T , η , and ϕ values are sampled from a realistic input $v_2(p_T, \eta)$ distribution. These events are then analyzed using the same procedure as in the data and the resulting $v_2(p_T, \eta)$ values are compared to the input. We find that the Lee–Yang zeros method tends to underestimate the results if the r.m.s. of the multiplicity distribution is more than about 14% of the mean. In order to keep the systematic uncertainties below 2%, the data are analyzed in 5%-wide centrality classes and then averaged and weighted with the charged-particle yield, to obtain results in wider centrality intervals needed for comparisons with other methods. Efficiency corrections are implemented as a track-by-track weight in the differential generating function.

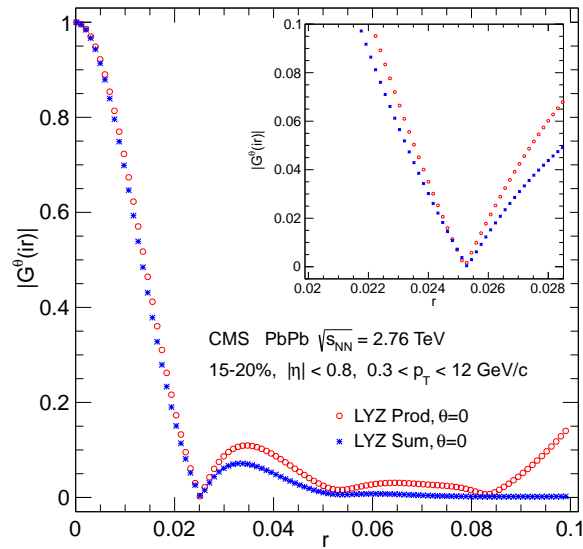


Figure 5: (Color online) An example of the modulus of the second harmonic Lee–Yang zero generating function $G^\theta(ir)$ as a function of the imaginary axis coordinate r for $\theta = 0$. Both the sum and product generating functions are shown, calculated from events with centrality 15–20%, $|\eta| < 0.8$, and $0.3 < p_T < 12$ GeV/c. An enlargement of $|G^\theta(ir)|$ around its first minimum is shown in the inset.

2.6 Corrections to the anisotropy parameter v_2

In determining the $v_2(p_T)$ distributions for particles detected in the tracker, it is necessary to correct for the influence of misidentified (i.e., “fake”) tracks on the measurements. As shown in Section 2.4, the fake-track contribution is particularly significant at low- p_T values and for pseudorapidities $|\eta| > 1.6$. Of particular concern is the observation that the fake tracks can carry a v_2 signal at low p_T similar to that of properly reconstructed (i.e., “real”) tracks at a higher p_T . Since the true v_2 signal is very small at low p_T , but increases at higher p_T , the fake tracks may contribute a significant fraction of the measured v_2 signal at low p_T .

Studies using a full MC CMS simulation of PbPb collisions based on the HYDJET event generator [57] indicate that the component of the v_2 signal due to fake tracks is relatively constant for $p_T < 0.8$ GeV/c, where the fraction of fake tracks is largest. For higher p_T , where the fraction of fake tracks is quite small, the value of v_2 is consistent with the measured value from correctly reconstructed tracks. This suggests the following simple correction scheme. Let $N_{\text{det}}(p_T)$

be the number of reconstructed tracks in a given p_T bin, f the fraction of these tracks that are “fake,” N_{true} the number of “true” tracks in the p_T bin, and e the efficiency for reconstructing a true track in the bin. Then $N_{\text{det}} - fN_{\text{det}} = eN_{\text{true}}$. The fN_{det} fake tracks are characterized by a constant v_2 value given by v_2^{fake} . The $N_{\text{det}} - fN_{\text{det}}$ real tracks are characterized by v_2^{real} . Then the observed value v_2^{obs} of v_2 will be

$$v_2^{\text{obs}} = (1 - f)v_2^{\text{real}} + fv_2^{\text{fake}} \quad (15)$$

and so

$$v_2^{\text{real}} = \frac{v_2^{\text{obs}} - fv_2^{\text{fake}}}{1 - f}. \quad (16)$$

This correction for the fake-track signal is only significant for p_T values less than $\approx 1 \text{ GeV}/c$. In this range, an empirical correction that results in values of v_2 that are independent of the track selection requirements or fraction of fake tracks is applied using $v_2^{\text{fake}} = 1.3 \langle v_2 \rangle$, where the yield-weighted average is performed over the transverse momentum range 0.3 to 3 GeV/c , folding in the efficiency-corrected spectra. This value for v_2^{fake} is also supported by MC studies using HYDJET.

2.7 Systematic uncertainties

2.7.1 Systematic uncertainties in the measurements of v_2

The systematic uncertainties in the measurements of v_2 include those common to all methods, as well as method-specific uncertainties. They are evaluated as relative uncertainties and are reported as percentages relative to the measured v_2 values. Since we are reporting the results on v_2 for nonidentified charged particles, it is important to investigate the tracking efficiency as a function of particle species. The tracking efficiencies for charged pions, kaons, protons, and antiprotons are determined using a full simulation of CMS. Subsequently, the value of $v_2(p_T)$ for charged particles is obtained using different assumptions for the p_T -dependence of v_2 and the transverse momentum spectra of each particle type, taking into account the corresponding reconstruction efficiencies. The results are compared to those obtained with the assumption of a particle-species-independent efficiency. The uncertainties in the charged particle v_2 results are estimated to be $\lesssim 0.5\%$, independent of the p_T , η , and centrality ranges. This uncertainty is listed as “Part. composition” in Tables 2–9.

Since the v_2 value changes with centrality, an uncertainty in the centrality determination can lead to a shift in the v_2 measurement. This uncertainty is evaluated by varying the value of the minimum-bias trigger efficiency to include $(97 \pm 3)\%$ of the total inelastic cross section. The resulting uncertainty on v_2 is of the order 1%, independent of the p_T , η , and centrality ranges. This uncertainty is listed as “Cent. determination” in Tables 2–9.

The kinematic requirements used to select tracks can affect the efficiency of track finding and the relative fraction of fake tracks in an event. The requirements are varied from their default values to estimate the systematic uncertainty. For each set of requirements, corresponding corrections are obtained for the fake-track contribution to the v_2 signal, as described in Section 2.6. For a given centrality and p_T range, the systematic uncertainty is estimated based on the stability of the v_2 value after corrections for fake tracks, independent of the track selection requirements. The uncertainty is found to be directly related to the magnitude of the fake-track contribution, with the final results deemed unreliable when the fake-rate is higher than $\approx 20\%$.

For the results presented in Section 3, the systematic uncertainties from this source remain below 4% over the entire range of p_T , η , and centrality, and are significantly below this value for $p_T > 0.5 \text{ GeV}/c$, centrality above 10%, and $|\eta| < 1.6$. The uncertainty in the efficiency corrections is evaluated by determining the efficiency based on the HYDJET model, and by embedding simulated pions into PbPb events in data. Although the two resulting efficiencies do have differences, the uncertainty on the v_2 value is small, at most 0.5%. Variations in the v_2 results due to changing detector conditions throughout the data-taking period are studied by dividing the data into three subgroups and are found to be below 1% for all measurements. The combined uncertainties from the efficiency corrections, fake-track corrections, and variations in detector conditions are listed under ‘‘Corrections’’ in Tables 2–9.

Additional studies of the systematic uncertainty are conducted for each method. In the event-plane method, flattening corrections are obtained using different procedures. The vertex dependence of the flattening parameters is examined and different subevent η gaps are used in obtaining the resolution corrections. The uncertainties from these sources are found to be negligible. The resolution corrections are measured with the three-subevent and two-subevent methods and are found to be consistent within the statistical uncertainties. The statistical uncertainties for the resolution correction factor are less than 1%, except for the most peripheral 70–80% centrality events, where the statistical uncertainty reaches a value of 2%. We include the statistical uncertainties associated with the resolution-correction factors as part of the overall systematic uncertainty on tracking efficiency and fake-track corrections for the event-plane method.

In the cumulant method, we examine the numerical stability of the result when the radius parameter r_0 used in the interpolations of the generating function is increased or decreased by half of its central value. The effects of multiplicity fluctuations are studied for the Lee–Yang zeros and the cumulant methods by analyzing the events in finer 2.5% centrality bins, and by using a fixed number of particles chosen at random from each event in a given centrality class.

The systematic uncertainties are smallest for the mid-rapidity region $|\eta| < 0.8$, $p_T > 0.5 \text{ GeV}/c$, and in the mid-central events (10–40%), and range from 2.0 to 4.5% for the different methods. At low p_T for the most central events, and in the forward pseudorapidity region where the fake-track contributions are larger, the uncertainties increase to 2.4–6.8%. Similarly, in the most peripheral events the uncertainties increase mostly due to multiplicity fluctuations and reach up to 3.2–7%, depending on the experimental method. A summary of the systematic uncertainties is presented in Tables 2–9.

Table 2: Systematic uncertainties in the measurement of $v_2(p_T)$ for $|\eta| < 0.8$ with the event-plane method for different p_T and centrality ranges.

Source	p_T (GeV/c)	Centrality		
		0 – 10%	10 – 70%	70 – 80%
Part. composition	All	0.5%	0.5%	0.5%
Cent. determination	All	1.0%	1.0%	1.0%
Corrections	< 0.3	4.0%	2.0%	3.0%
	0.3 – 0.5	2.0%	< 1.0%	2.0%
	0.5 – 22.0	< 1.0%	< 1.0%	2.0%
Total	< 0.3	4.2%	2.3%	3.2%
	0.3 – 0.5	2.3%	1.5%	2.3%
	0.5 – 22.0	1.5%	1.5%	2.3%

Table 3: Systematic uncertainties in the measurement of $v_2(\eta)$ for $0.3 < p_T < 3 \text{ GeV}/c$ with the event-plane method for different η and centrality ranges.

Source	$ \eta $	Centrality		
		0 – 10%	10 – 70%	70 – 80%
Part. composition	All	0.5%	0.5%	0.5%
Cent. determination	All	1.0%	1.0%	1.0%
Corrections	0.0 – 1.6	2.0%	< 1.0%	2.0%
	1.6 – 2.4	4.0%	2.0%	3.0%
Total	0.0 – 1.6	3.2%	1.5%	2.3%
	1.6 – 2.4	4.2%	2.3%	3.2%

Table 4: Systematic uncertainties in the measurement of $v_2(p_T)$ for $|\eta| < 0.8$ with the two-particle cumulant method for different p_T and centrality ranges.

Source	p_T (GeV/c)	Centrality			
		0 – 5%	5 – 10%	10 – 70%	70 – 80%
Part. composition	All	0.5%	0.5%	0.5%	0.5%
Cent. determination	All	1.0%	1.0%	1.0%	1.0%
Multiplicity fluct.	All	0.5%	1.5%	4.0%	4.0%
r_0 parameter	All	0.2%	0.2%	0.2%	0.1%
Corrections	0.3 – 0.5	3.8%	1.7%	0.6%	4.0%
	0.5 – 22.0	2.9%	2.1%	0.6%	3.0%
Total	0.3 – 0.5	4.0%	2.6%	4.2%	5.8%
	0.5 – 22.0	3.2%	2.9%	4.2%	5.1%

2.7.2 Systematic uncertainties in the measurements of the transverse momentum spectra and the mean transverse momentum $\langle p_T \rangle$

Several sources of systematic uncertainty are considered in obtaining the inclusive charged-particle transverse momentum distributions and their mean values, $\langle p_T \rangle$. These include the uncertainties in the efficiency and fake-track correction factors, the particle-species-dependent efficiency, and the uncertainty in the minimum-bias trigger efficiency. The effect on the overall normalization of the spectra is considered separately from the smaller effect on the shape of the spectra as a function of p_T . To obtain the mean transverse momentum, different functional forms are used to extrapolate the spectra down to $p_T = 0$, and the p_T range over which the spectra are fitted is varied. The combined point-to-point systematic uncertainties on the spectra are presented as a function of pseudorapidity in Table 10. The total normalization uncertainty of the charged-particle spectra measured in each centrality interval is given in Table 11. The systematic uncertainties in the measurement of $\langle p_T \rangle$ in different pseudorapidity intervals are summarized in Table 12.

3 Results

The main results of the analysis using the four methods described above are as follows:

- $v_2(p_T)$ at mid-rapidity $|\eta| < 0.8$.
- Integrated v_2 at mid-rapidity $|\eta| < 0.8$ and $0.3 < p_T < 3 \text{ GeV}/c$.
- $v_2(\eta)$ for $0.3 < p_T < 3 \text{ GeV}/c$.

Table 5: Systematic uncertainties in the measurement of $v_2(\eta)$ for the range $0.3 < p_T < 3 \text{ GeV}/c$ with the two-particle cumulant method for different η and centrality ranges.

Source	$ \eta $	Centrality	
		5 – 10%	10 – 70%
Part. composition	All	0.5%	0.5%
Cent. determination	All	1.0%	1.0%
Multiplicity fluct.	All	1.5%	4.0%
r_0 parameter	All	0.2%	0.2%
Corrections	0.0 – 1.6	0.8%	1%
	1.6 – 2.4	1.5%	1.6%
Total	0.0 – 1.6	2.0%	4.2%
	1.6 – 2.4	2.4%	4.4%

Table 6: Systematic uncertainties in the measurement of $v_2(p_T)$ for $|\eta| < 0.8$ with the four-particle cumulant method for different p_T and centrality ranges.

Source	p_T (GeV/c)	Centrality			
		5 – 10%	10 – 40%	40 – 60%	60 – 70%
Part. composition	All	0.5%	0.5%	0.5%	0.5%
Cent. determination	All	1.0%	1.0%	1.0%	1.0%
Multiplicity fluct.	All	5.0%	3.0%	5.0%	5.0%
r_0 parameter	All	2.0%	3.0%	1.0%	0.1%
Corrections	0.3 – 0.5	4.1%	1.4%	3.0%	4.5%
	0.5 – 22.0	2.2%	1.2%	1.1%	3.0%
Total	0.3 – 0.5	6.8%	4.6%	6.0%	6.8%
	0.5 – 22.0	5.9%	4.5%	5.3%	6.0%

We also measure the charged-particle transverse momentum spectra and their mean p_T for the centrality and pseudorapidity ranges in which the flow is studied.

The flow studies are performed in the 12 centrality classes listed in Table 1. Using these results, we examine the scaling of the integrated v_2 with the participant eccentricity, as well as perform comparisons to measurements from other experiments. Centrality classes are regrouped to perform these comparisons, i.e., the results of $v_2(p_T)$, $v_2(\eta)$, or integrated v_2 obtained in the finer bins of centrality are averaged over wider bins, weighted using the corresponding $d^2N/dp_T d\eta$ spectra. The evolution of the measured elliptic anisotropy as a function of centrality, center-of-mass energy, and transverse particle density is studied. The scaling of $v_2(\eta)$ in the longitudinal dimension is also examined through comparisons to RHIC data.

3.1 Transverse momentum dependence of v_2

In Figs. 6–9, we present the measurement of v_2 for charged particles as a function of transverse momentum at mid-rapidity, obtained by each analysis method. We use the notation $v_2\{\text{EP}\}$ to refer to the measurement of v_2 using the event-plane method, and $v_2\{2\}$, $v_2\{4\}$, $v_2\{\text{LYZ}\}$ to refer to those using the two-particle cumulant, four-particle cumulant, and Lee–Yang zeros methods, respectively. Several trends can be observed and related to the physics processes dominating hadron production in different p_T ranges. The value of v_2 increases from central to peripheral collisions up to 40% centrality, as expected if the anisotropy is driven by the spatial anisotropy in the initial state [12, 15, 21]. The transverse momentum dependence shows

Table 7: Systematic uncertainties in the measurement of $v_2(\eta)$ for the range $0.3 < p_T < 3 \text{ GeV}/c$ with the four-particle cumulant method for different η and centrality ranges.

Source	$ \eta $	Centrality		
		5 – 10%	10 – 40%	40 – 70%
Part. composition	All	0.5%	0.5%	0.5%
Cent. determination	All	1.0%	1.0%	1.0%
Multiplicity fluct.	All	5.0%	3.0%	5.0%
r_0 parameter	All	2.0%	3.0%	1.0%
Corrections	0.0 – 1.6	1.5%	1.5%	1.5%
	1.6 – 2.4	1.8%	2.1%	1.9%
Total	0.0 – 1.6	5.8%	4.8%	5.4%
	1.6 – 2.4	5.8%	5.0%	5.6%

Table 8: Systematic uncertainties in the measurement of $v_2(p_T)$ for $|\eta| < 0.8$ with the Lee–Yang zeros method for different p_T and centrality ranges.

Source	p_T (GeV/c)	Centrality		
		5 – 10%	10 – 40%	40 – 50%
Part. composition	All	0.5%	0.5%	0.5%
Cent. determination	All	1.0%	1.0%	1.0%
Multiplicity fluct.	All	0.1%	0.9%	1.9%
Corrections	0.3 – 0.5	2.5%	1.7%	0.7%
	0.5 – 22.0	1.5%	1.0%	0.6%
Total	0.3 – 0.5	2.7%	2.2%	2.3%
	0.5 – 22.0	1.9%	1.8%	2.3%

a rise of v_2 up to $p_T \approx 3 \text{ GeV}/c$ and then a decrease. As a function of centrality, a tendency for the peak position of the $v_2(p_T)$ distribution to move to higher p_T in more central collisions is observed, with the exception of the results from the most peripheral collisions in the two-particle cumulant and the event-plane methods.

In ideal hydrodynamics the azimuthal anisotropy continuously increases with increasing p_T [12, 21]. The deviation of the theory from the RHIC data at $p_T \gtrsim 2\text{--}3 \text{ GeV}/c$ has been attributed to incomplete thermalization of the high- p_T hadrons, and the effects of viscosity. Indeed, viscous hydrodynamic calculations [15, 16, 65] show that the shear viscosity has the effect of reducing the anisotropy at high p_T . At $p_T \gtrsim 8 \text{ GeV}/c$, where hadron production is dominated by jet fragmentation, the collective-flow effects are expected to disappear [15, 21]. Instead, an asymmetry in the azimuthal distribution of hadron emission with respect to the reaction plane could be generated by path-length-dependent parton energy loss [28, 30, 31]. For events with similar charged-particle suppression [66], but different reaction-zone eccentricity, one might expect that the geometric information would be imprinted in the elliptic anisotropy signal. The upper panels of Figs. 6–9 (centrality 0–35%) show a trend that is consistent with this expectation. In more central events, where the eccentricity is smaller, the elliptic anisotropy value is systematically lower. In more peripheral collisions (centrality 35–80%), there is a complex interplay between the reduced energy loss and the increase in eccentricity that influence the $v_2(p_T)$ value in opposite directions. The data presented here provide the basis for future detailed comparisons to theoretical models.

An important consideration in interpreting the $v_2(p_T)$ results is the contribution from non-

Table 9: Systematic uncertainties in the measurement of $v_2(\eta)$ for $0.3 < p_T < 3 \text{ GeV}/c$ with the Lee–Yang zeros method for different η and centrality ranges.

Source	$ \eta $	Centrality		
		5 – 10%	10 – 40%	40 – 50%
Part. composition	All	0.5%	0.5%	0.5%
Cent. determination	All	1.0%	1.0%	1.0%
Multiplicity fluct.	All	0.1%	0.9%	1.9%
Corrections	0.0 – 1.6	1.3%	1.0%	0.8%
	1.6 – 2.4	1.5%	1.4%	1.3%
Total	0.0 – 1.6	1.7%	1.8%	2.4%
	1.6 – 2.4	1.9%	2.0%	2.5%

Table 10: Point-to-point systematic uncertainties in the measurement of the charged-particle spectra in different pseudorapidity intervals.

Source of Uncertainty	$ \eta < 0.8$	$0.8 < \eta < 1.2$	$2.0 < \eta < 2.4$
Tracking Efficiency	5%	8%	13%
Particle Composition	1%	1%	2%
Trigger Efficiency	3%	3%	3%
Total	6%	9%	14%

flow correlations and initial-state eccentricity fluctuations. To aid in assessing the magnitude of these effects and their evolution with the centrality of the collisions, the results of $v_2(p_T)$ obtained by all methods at mid-rapidity are compared in Fig. 10 for 12 centrality classes. The four methods show differences as expected due to their sensitivities to nonflow contributions [37, 42, 43] and eccentricity fluctuations [34, 35, 38].

The method that is most affected by nonflow correlations is the two-particle cumulant, because of the fact that the reference and the differential flow signals are determined in the same pseudorapidity range. The event-plane method is expected to be similarly affected if dedicated selections are not applied to reduce these contributions. In our analysis, the particles used in the event-plane determination and the particles used to measure the flow are at least 3 units of pseudorapidity apart, which suppresses most nonflow correlations. The differences between the two-particle cumulant and the event-plane methods are most pronounced at high p_T and in peripheral collisions, where jet-induced correlations dominate over the collective flow.

In a collision where M particles are produced, direct k -particle correlations are typically of order $1/M^{k-1}$, so that they become smaller as k increases. Therefore, the fourth-order cumulant and the Lee–Yang zeros methods are expected to be much less affected by nonflow contributions than the second-order cumulant method [37, 42, 43]. This trend is seen in our data.

3.2 Centrality dependence of integrated v_2 and eccentricity scaling

To obtain the integrated v_2 values as a function of centrality at mid-rapidity, $v_2(p_T)$ measurements are averaged over p_T , weighted by the corresponding charged-particle spectrum. The integration range $0.3 < p_T < 3 \text{ GeV}/c$ is limited to low p_T to maximize the contribution from soft processes, which facilitates comparisons to hydrodynamic calculations.

The centrality dependence of the integrated v_2 at mid-rapidity $|\eta| < 0.8$ is presented in Fig. 11, for the four methods. The v_2 values increase from central to peripheral collisions, reaching

Table 11: Normalization uncertainty in the measurement of the charged-particle spectra in different centrality intervals resulting from the uncertainty in the minimum-bias trigger efficiency.

Centrality Range	Normalization Uncertainty
0-5%	0.4%
5-10%	1.0%
10-15%	1.7%
15-20%	2.3%
20-25%	3.1%
25-30%	4.1%
30-35%	5.0%
35-40%	6.1%
40-50%	8.0%
50-60%	12%
60-70%	16%
70-80%	21%

Table 12: Systematic uncertainty of the mean p_T of charged particles from each source and in total as a function of pseudorapidity.

Source of Uncertainty	$ \eta < 0.4$	$0.8 < \eta < 1.2$	$2.0 < \eta < 2.4$
Fit function	3%	3%	4%
Trigger Efficiency	1.5%	1.5%	1.5%
Tracking Efficiency	2%	2%	2.5%
Total	3.9%	3.9%	4.9%

a maximum in the 40–50% centrality range. In the more peripheral collisions, a decrease in v_2 is observed in the event-plane and four-particle cumulant measurements, while the values obtained with the two-particle cumulant method remain constant within their uncertainties. The results for $v_2\{2\}$ are larger than those for $v_2\{EP\}$, while the $v_2\{4\}$ and $v_2\{LYZ\}$ values are smaller. To facilitate a quantitative comparison between the methods, including their respective systematic uncertainties, the bottom panel of Fig. 11 shows the results from the cumulant and the Lee–Yang zeros methods divided by those obtained from the event-plane method. The boxes represent the systematic uncertainty in the ratios, excluding sources of uncertainty common to all methods. The ratios are relatively constant in the 10-60% centrality range, but the differences between the methods increase for the most central and the most peripheral collisions. These findings are similar to results obtained by the STAR experiment at RHIC [67]. Below, we further investigate the differences in the v_2 values returned by each method.

The collective motion of the system, and therefore the anisotropy parameter, depend on the initial shape of the nucleus-nucleus collision area and the fluctuations in the positions of the interacting nucleons. By dividing v_2 by the participant eccentricity, one may potentially remove this dependence across centralities, colliding species, and center-of-mass energies, enabling a comparison of results in terms of the underlying physics driving the flow.

In Fig. 12, we examine the centrality dependence of the eccentricity-scaled anisotropy parameter obtained with the event-plane and cumulant methods at mid-rapidity, $|\eta| < 0.8$. The participant eccentricity and its cumulant moments are obtained from a Glauber-model simulation, as discussed in Section 2.3. The statistical and systematic uncertainties in the integrated v_2 mea-

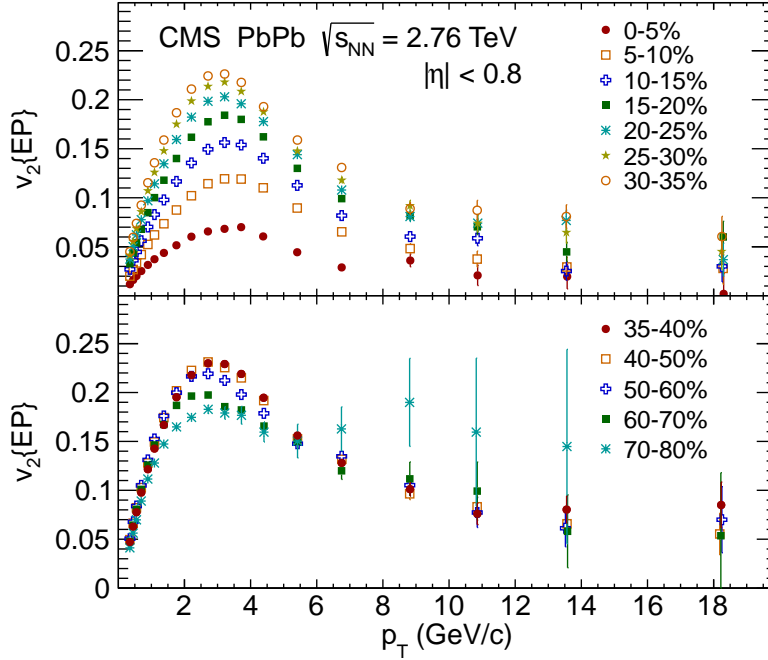


Figure 6: (Color online) Results from the event-plane (EP) method for v_2 as a function of p_T at mid-rapidity $|\eta| < 0.8$ for the 12 centrality classes given in the legend. The error bars show the statistical uncertainties only.

measurements are added in quadrature and represented by the error bars. The dashed lines show the systematic uncertainties in the eccentricity determination. In the left panel of Fig. 12, the results from each method are divided by the participant eccentricity, ϵ_{part} . The data show a near-linear decrease from central to peripheral collisions, with differences between methods that were already observed in Fig. 11. In the right panel, the v_2 values for the cumulant measurements are scaled by their respective moments of the participant eccentricity, thus taking into account the corresponding eccentricity fluctuations [34–38]. With this scaling, the two-particle cumulant and the event-plane results become nearly identical, except for the most central and the most peripheral collisions, where the cumulant results are more affected by nonflow contributions. This is expected [37] because in our application of the method there is no separation in rapidity between the particles used for the reference flow and those used in the differential flow measurement. In the centrality range of 15–40%, the four-particle cumulant measurement of $v_2\{4\}/\epsilon\{4\}$ is also in better agreement with the other two methods. This indicates that the main difference in the results from the different methods could be attributed to their sensitivity to eccentricity fluctuations. In the most central events, where the eccentricity $\epsilon\{4\}$ is very small, and in the most peripheral events, where the fluctuations are large, $v_2\{4\}/\epsilon\{4\}$ deviates from the common scaling behavior. For centralities above 50% the differences between the four-particle cumulant method and the other two methods do not seem to be accounted for by the initial-state fluctuations, as described in our implementation of the Glauber model. In this centrality range, the event-by-event fluctuations in the eccentricity are non-Gaussian due to the underlying Poisson distributions from discrete nucleons [34, 38] and are more difficult to model. It has also been suggested [34, 37] that when the event-plane resolution is smaller than ≈ 0.6 , as is the case for the peripheral collisions studied in CMS, the results from the event-plane method should be evaluated using the two-particle cumulant eccentricity $\epsilon\{2\}$, rather than the

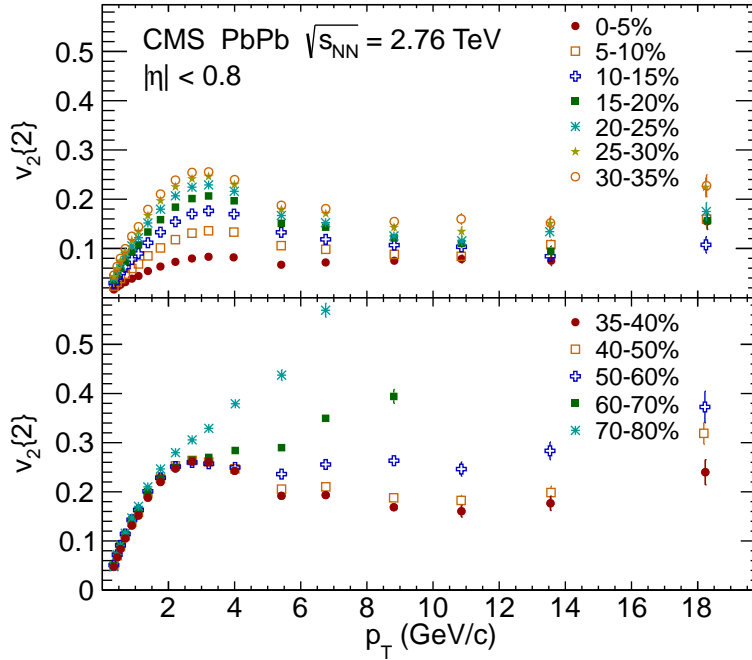


Figure 7: (Color online) Second-order cumulant results for v_2 as a function of p_T at mid-rapidity $|\eta| < 0.8$ for the 12 centrality classes given in the legend. The error bars show the statistical uncertainties only.

participant eccentricity ϵ_{part} . We have used a common definition of eccentricity (ϵ_{part}) for all centrality classes studied in our event-plane analysis. This would lower the measurements of $v_2\{\text{EP}\}/\epsilon$ by about 10% in the most peripheral collisions, which is not sufficient to reconcile the differences between the event-plane and the four-particle cumulant results.

Another model of the initial state that has been used in the literature [38, 39, 68–71], but has not been explored here, is the color glass condensate (CGC) model [72], which takes into account that at very high energies or small values of Bjorken x , the gluon density becomes very large and saturates. The CGC model predicts eccentricities that exceed the Glauber-model eccentricities by an approximately constant factor of around 1.2, with some deviation from this behavior in the most central and most peripheral collisions [38, 70]. The results presented here may give further insight into the nature of the initial-state fluctuations, especially in the regions where the eccentricity fluctuations become non-Gaussian.

3.3 Pseudorapidity dependence of v_2

The pseudorapidity dependence of the anisotropy parameter provides additional constraints on the system evolution in the longitudinal direction. To obtain the $v_2(\eta)$ distribution with the event-plane method, we first measure $v_2(p_T)$ in pseudorapidity bins of $\Delta\eta = 0.4$, and then average the results over the range $0.3 < p_T < 3 \text{ GeV}/c$, weighting with the efficiency and fake-rate-corrected spectrum.

For the cumulant and Lee–Yang zeros methods, the measurements are done using all particles in the range $|\eta| < 2.4$, and either $0.3 < p_T < 3 \text{ GeV}/c$ or $0.3 < p_T < 12 \text{ GeV}/c$ in the generating function, to obtain the reference flow, and then extracting the pseudorapidity dependence in small pseudorapidity intervals of $\Delta\eta = 0.4$. Tracking efficiency and fake-rate corrections are

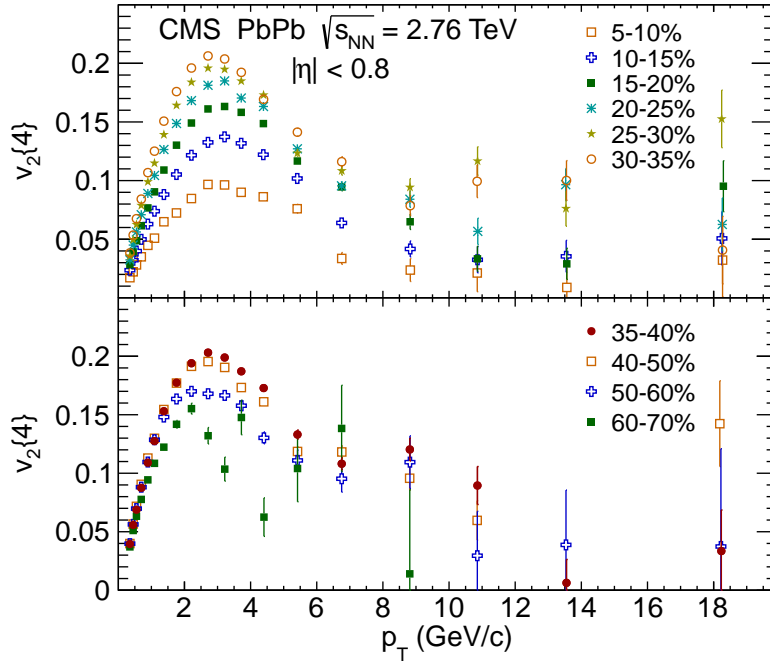


Figure 8: (Color online) Fourth-order cumulant results for v_2 as a function of p_T at mid-rapidity $|\eta| < 0.8$ for the 10 centrality classes given in the legend. The error bars show the statistical uncertainties only.

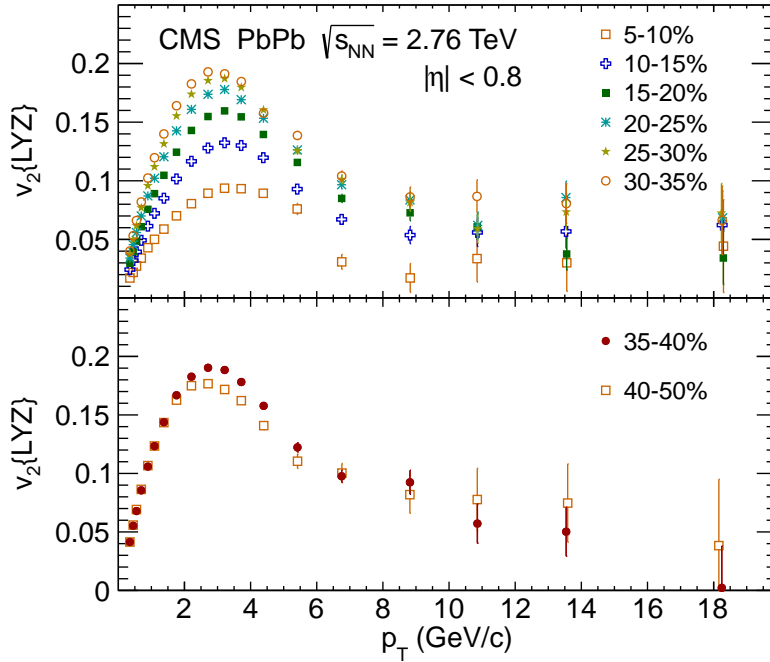


Figure 9: (Color online) Lee-Yang zeros results for v_2 as a function of p_T at mid-rapidity $|\eta| < 0.8$ for the 8 centrality classes given in the legend. The error bars show the statistical uncertainties only.

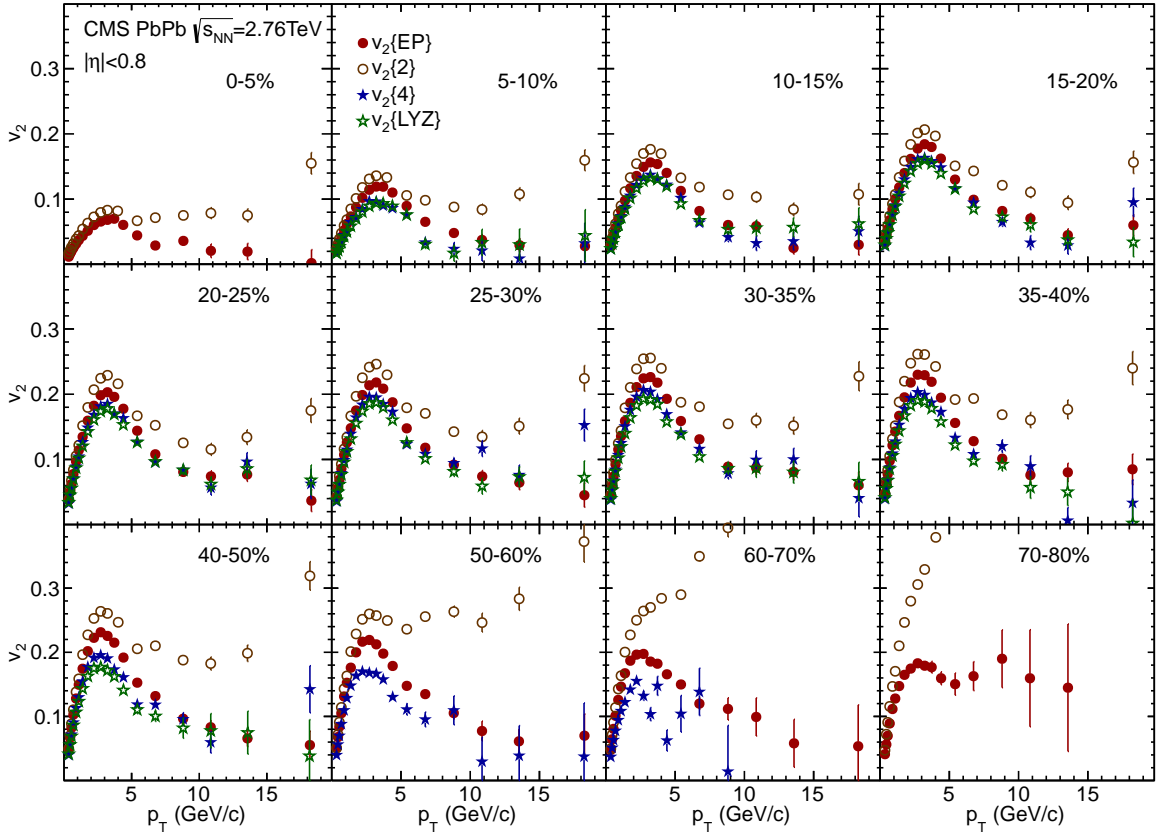


Figure 10: (Color online) Comparison of the four different methods for determining v_2 as a function of p_T at mid-rapidity ($|\eta| < 0.8$) for the 12 centrality classes given in the figures. The error bars show the statistical uncertainties only.

applied using a track-by-track weight in forming the differential generating functions. As a crosscheck, we have confirmed that at mid-rapidity the values obtained with this method agree with the ones obtained from a direct yield-weighted average of the $v_2(p_T)$ results from Figs. 7–9, within the stated systematic uncertainties.

As observed at mid-rapidity ($|\eta| < 0.8$) in Fig. 11, the values of $v_2\{4\}$ and $v_2\{LYZ\}$ are in agreement and are smaller than $v_2\{2\}$ and $v_2\{EP\}$. This behavior persists at larger pseudorapidity, as shown in Fig. 13, which suggests that similar nonflow correlations and eccentricity fluctuations affect the results over the full measured pseudorapidity range. The results show that the value of $v_2(\eta)$ is greatest at mid-rapidity and is constant or decreases very slowly at larger values of $|\eta|$. This behavior is most pronounced in peripheral collisions and for the two-particle cumulant method, which is most affected by nonflow contributions.

To assess whether the observed decrease in $v_2(\eta)$ in the forward pseudorapidity region in peripheral PbPb collisions is due to a pseudorapidity dependence in the $v_2(p_T)$ distributions or in the underlying charged-particle spectra, in Fig. 14 we examine the values of $v_2(p_T)$ obtained with the event-plane method for several pseudorapidity intervals in each of the 12 centrality classes shown in Fig. 13. From the most central events up to 35–40% centrality there is no change in the $v_2(p_T)$ distributions with pseudorapidity within the statistical uncertainties. Therefore, any change in the $v_2(\eta)$ distribution can be attributed to changes in the underlying

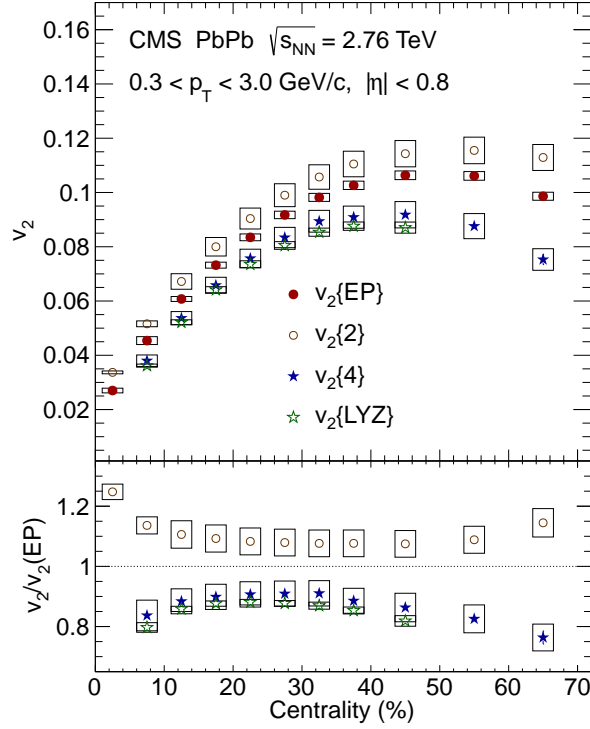


Figure 11: (Color online) Top panel: Integrated v_2 as a function of centrality at mid-rapidity $|\eta| < 0.8$ for the four methods. The boxes represent the systematic uncertainties. The magnitudes of the statistical uncertainties are smaller than the size of the symbols. Bottom panel: The values from three of the methods are divided by the results from the event-plane method. The boxes represent the systematic uncertainties excluding the sources that are common to all methods. The magnitudes of the statistical uncertainties are smaller than the size of the symbols.

charged-particle transverse momentum spectra. A gradual decrease is observed in the $v_2(p_T)$ values at forward pseudorapidity ($2.0 < |\eta| < 2.4$) in more peripheral events. For the 70–80% centrality class the values of $v_2(p_T)$ decrease by approximately 10% between the central pseudorapidity region $|\eta| < 0.4$ and the forward region $2.0 < |\eta| < 2.4$. Thus, the pseudorapidity dependence in $v_2(\eta)$ for peripheral collisions observed in Fig. 13 is caused by changes in the $v_2(p_T)$ distributions with pseudorapidity, as well as changes in the underlying transverse momentum spectra presented in Section 3.4.

3.4 Centrality and pseudorapidity dependence of the transverse momentum distributions

Elliptic flow measures the azimuthal anisotropy in the invariant yield of the final-state particles. Therefore, the charged-particle transverse momentum distributions influence the observed results. The soft-particle-production mechanism and the evolution of the expanding nuclear medium are reflected in the low- p_T range of the transverse momentum spectra. In the hydrodynamics calculations, measurements of the pseudorapidity density of charged particles produced in collisions with different centrality constrain the description of the initial entropy and the energy density distribution in the collision zone, while the mean transverse momentum of the particle spectra constrains the final temperature and the radial-flow velocity of the system. With additional input on the equation-of-state that is typically provided by lattice QCD, the hydrodynamics calculations then provide a description of the system evolution from some

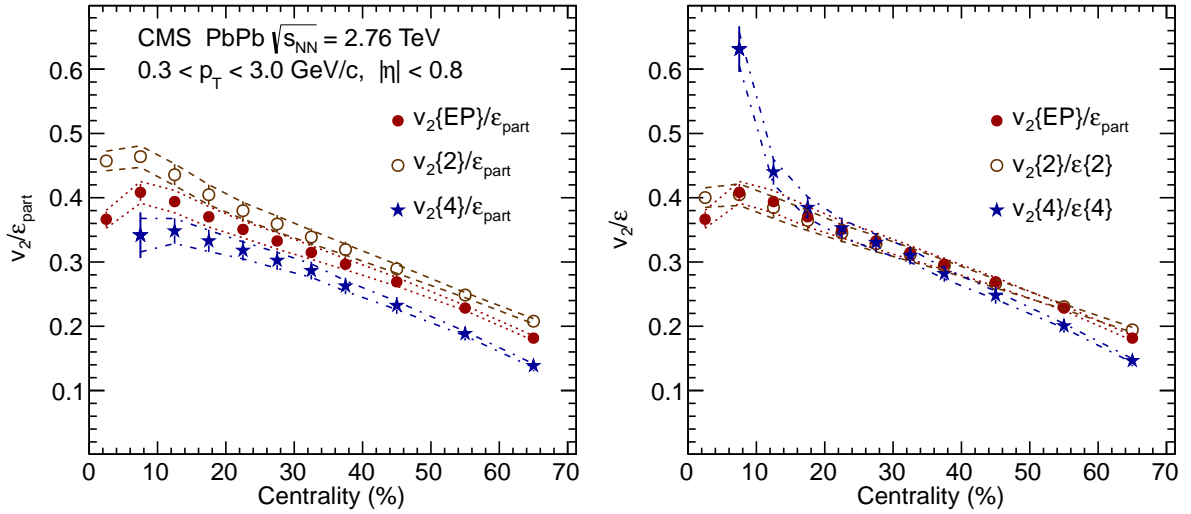


Figure 12: (Color online) Left panel: Centrality dependence of the integrated v_2 divided by the participant eccentricity, ϵ_{part} , obtained at mid-rapidity $|\eta| < 0.8$ for the event-plane and two- and four-particle cumulant methods. Right panel: The measurements of v_2 as a function of centrality are the same as in the left panel, but here the two-particle and four-particle cumulant results are divided by their corresponding moments of the participant eccentricity, $\epsilon\{2\}$ and $\epsilon\{4\}$. In both panels, the error bars show the sum in quadrature of the statistical and systematic uncertainties in the v_2 measurement, and the lines represent the systematic uncertainties in the eccentricity determination.

initial time, when local thermal equilibrium is achieved, to the “freeze-out”, when the particle interactions cease.

We have measured the charged-particle transverse momentum spectra for 12 centrality classes over the pseudorapidity range $|\eta| < 2.4$ in bins of $\Delta\eta = 0.4$. Examples of these distributions for the mid-rapidity ($|\eta| < 0.4$) and forward-rapidity ($2.0 < |\eta| < 2.4$) regions are shown in Fig. 15. These results extend the measurements of charged-particle spectra previously reported by CMS [66] down to $p_T = 0.3 \text{ GeV}/c$ and to forward pseudorapidity. The measurements presented here are in good agreement with the results in Ref. [66] in their common ranges of p_T , pseudorapidity, and centrality.

The evolution of the charged-particle spectra with centrality and pseudorapidity can be quantified in terms of the mean p_T of the transverse momentum distributions. The values of $\langle p_T \rangle$ as a function of N_{part} , which is derived from the centrality of the event, are shown in Fig. 16. In each pseudorapidity interval, the values of $\langle p_T \rangle$ increase with N_{part} up to $N_{\text{part}} \approx 150$ and then saturate, indicating that the freeze-out conditions of the produced system are similar over a broad range of collision centralities (0–35%). This behavior is in contrast to the centrality dependence in the integrated v_2 values at mid-rapidity shown in Fig. 11 that vary strongly in this centrality range. On the other hand, in more peripheral collisions (centrality greater than 35%) the $v_2(p_T)$ values do not vary much with centrality at low p_T , as shown in the bottom panels of Figs. 6–9, while the spectral shapes change, as indicated by the $\langle p_T \rangle$ measurement. This behavior is qualitatively similar at forward pseudorapidities, as shown in Figs. 14 and 16. These measurements taken together will help in understanding the early-time dynamics in the system evolution, which is reflected in the elliptic flow, and the overall evolution through the hadronic stage, which is reflected in the charged-particle spectra.

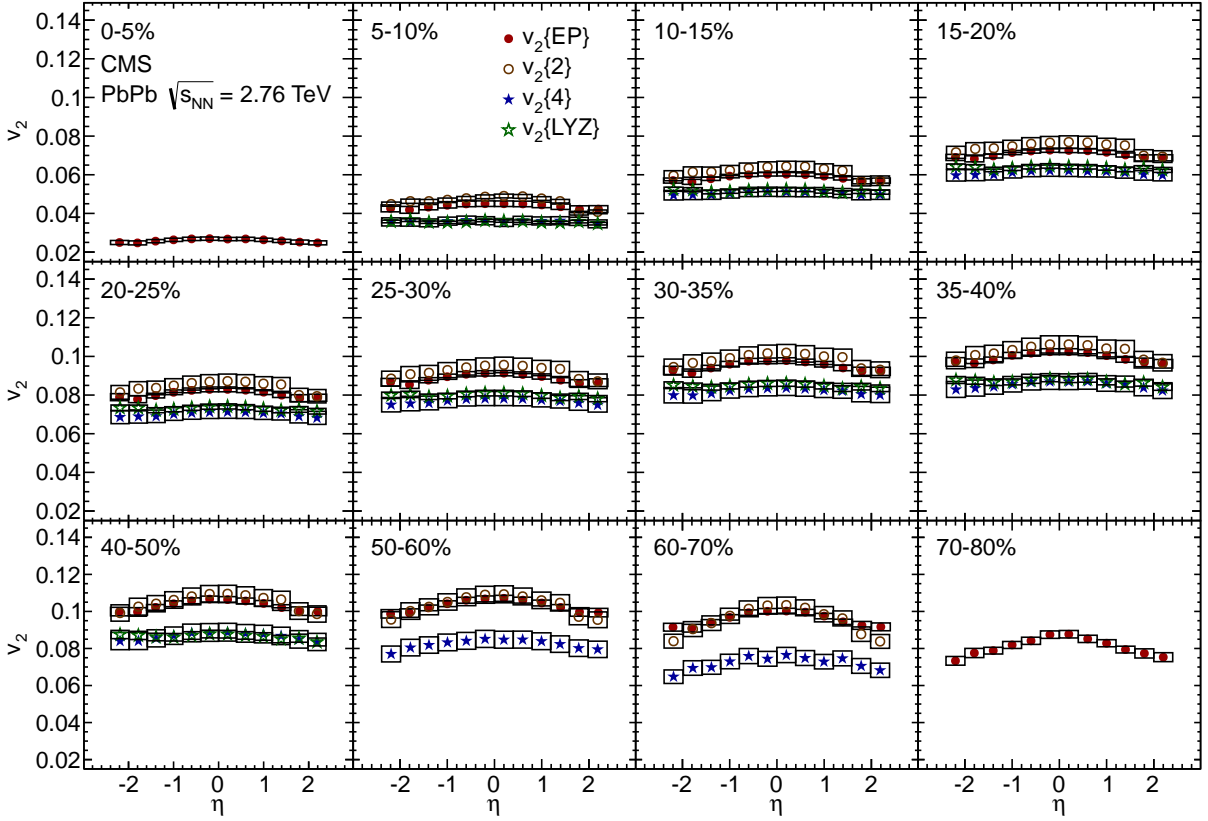


Figure 13: (Color online) Pseudorapidity dependence of v_2 for $0.3 < p_T < 3$ GeV/c with all four methods in 12 centrality classes. The boxes give the systematic uncertainties. The magnitudes of the statistical uncertainties are smaller than the size of the symbols.

3.5 Comparison with other measurements of v_2 at the LHC

Results on the elliptic anisotropy measured in PbPb collisions in $\sqrt{s_{NN}} = 2.76$ TeV have previously been reported by the ALICE [13] and ATLAS [14] experiments. A comparison of $v_2\{2\}$ and $v_2\{4\}$ as a function of p_T in the 40–50% centrality class for $|\eta| < 0.8$ from CMS and ALICE [13] is shown in Fig. 17. The error bars give the statistical uncertainties, and the boxes represent the systematic uncertainties in the CMS measurements. The two measurements are in good agreement over their common p_T range.

A comparison of $v_2(p_T)$ obtained with the event-plane method at mid-rapidity from CMS and ATLAS [14] is presented in Fig. 18 for the centrality ranges of the ATLAS measurement. The error bars show the statistical and systematic uncertainties added in quadrature. The results are in good agreement within the statistical and systematic uncertainties.

4 Discussion

We compare the CMS elliptic flow measurements presented in Section 3 with results obtained at RHIC by the PHENIX, STAR, and PHOBOS experiments. Since each method for measuring v_2 has a different sensitivity to nonflow correlations and initial-state fluctuations, we make these comparisons for measurements conducted with the same method and with similar kinematic requirements in the method's implementation. In Fig. 19 the mid-rapidity measurement

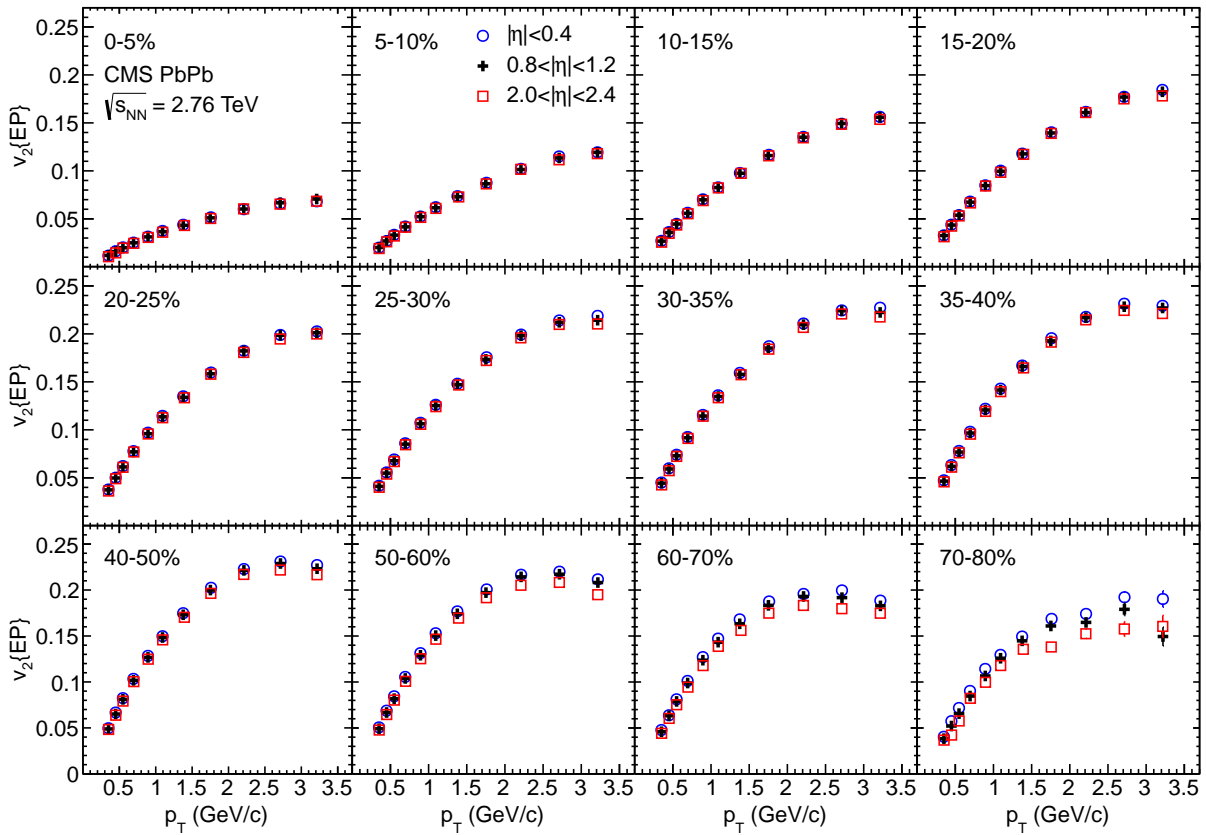


Figure 14: (Color online) Results from the event-plane method for $v_2(p_T)$ in three pseudorapidity regions and in 12 centrality classes. The error bars show the statistical uncertainties that in most cases have magnitudes smaller than the size of the symbol.

of $v_2(p_T)$ with the event-plane method in CMS is compared to results from PHENIX [73] for $\sqrt{s_{NN}} = 200$ GeV AuAu collisions. For the PHENIX measurement, the event plane was determined at forward pseudorapidities, $|\eta| = 3.1\text{--}3.9$, while the $v_2(p_T)$ measurement was performed in the pseudorapidity interval $|\eta| < 0.35$, thus providing a separation of at least 2.75 units of pseudorapidity between the charged particles used for the $v_2(p_T)$ analysis and the particles used in the event-plane determination. This procedure is comparable to the CMS approach, where a separation of at least 3 units of pseudorapidity is used. These large pseudorapidity gaps are expected [37] to suppress nonflow contributions in both measurements. The pseudorapidity interval for the CMS measurement is wider, $|\eta| < 0.8$, but since the pseudorapidity dependence of $v_2(\eta)$ was shown to be weak (see Fig. 13), this difference should not influence the comparison of the results. The top panels in Fig. 19 show the measurements of $v_2(p_T)$ from CMS (closed symbols) and PHENIX (open symbols) for several centrality classes. The error bars represent the statistical uncertainties only. The shape of the $v_2(p_T)$ distributions and the magnitude of the signals are similar, in spite of the factor of ≈ 14 increase in the center-of-mass energy. To facilitate a quantitative comparison of these results, the CMS measurements are fitted with a combination of a fifth-order polynomial function (for $p_T < 3.2$ GeV/c) and a Landau distribution (for $3 < p_T < 7$ GeV/c). There is no physical significance attributed to these functional choices, other than an attempt to analytically describe the CMS $v_2(p_T)$ distributions, so that the value of v_2 can be easily compared to results from other experiments, which have been obtained with different p_T binning. The results from the fits are plotted as solid lines in the top panels of Fig. 19. In the bottom panels, the fit function is used to evaluate $v_2(p_T)$

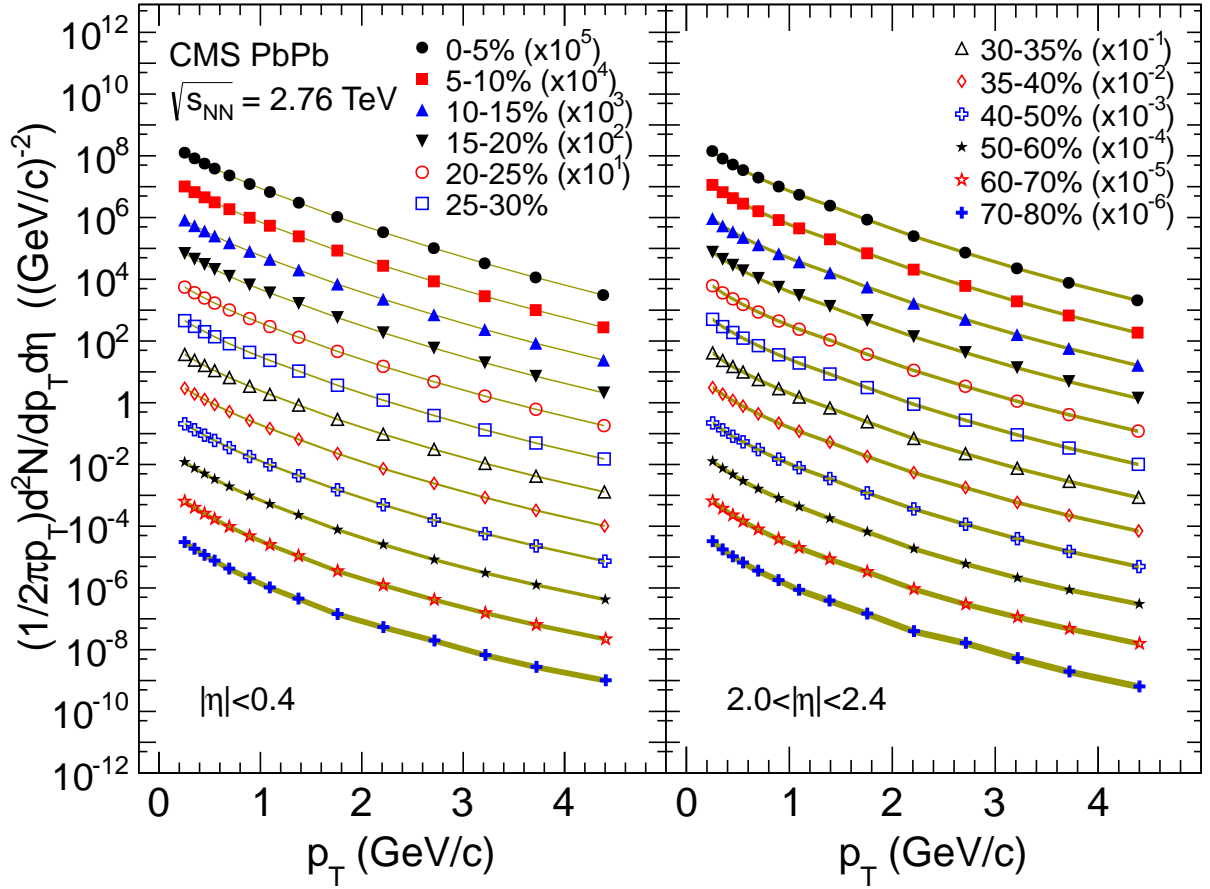


Figure 15: (Color online) Inclusive charged-particle spectra at mid-rapidity (left) and forward rapidity (right), for the 12 centrality classes given in the legend. The distributions are offset by arbitrary factors given in the legend for clarity. The shaded bands represent the statistical and systematic uncertainties added in quadrature, including the overall normalization uncertainties from the trigger efficiency estimation.

at the p_T values for each data set, and then to form the ratios between the CMS fit values and the PHENIX data, and the CMS fit to the CMS measurements. The error bars represent the statistical uncertainties. The systematic uncertainties from the CMS and PHENIX measurements are added in quadrature and plotted as shaded boxes. The $v_2(p_T)$ values measured by CMS are systematically higher than those from PHENIX in all centrality classes and over the entire transverse momentum range measured by PHENIX. The relative deviations of are the order 10%, except for the most peripheral collisions where they reach 15%.

A similar comparison is carried out for the two-particle and four-particle cumulant methods. In Fig. 20, the results from the STAR experiment [74] for AuAu collisions at $\sqrt{s_{NN}} = 200$ GeV in the 20–60% centrality range are compared with the CMS measurements. The pseudorapidity interval for the STAR measurement is $|\eta| < 1.3$, compared to $|\eta| < 0.8$ for CMS. These η ranges are within a pseudorapidity region in which the $v_2(\eta)$ values only weakly depend on the pseudorapidity. The kinematic selections imposed on the charged particles used in determining the reference flow are also similar in the CMS and STAR measurements. The top panels of Fig. 20 show the $v_2(p_T)$ distributions for the two-particle (left) and four-particle (right) cumulant method from both experiments, along with fits to the CMS data (lines). The functional form used for the fit of the CMS $v_2(p_T)$ distributions is the same as the one used in Fig. 19. The

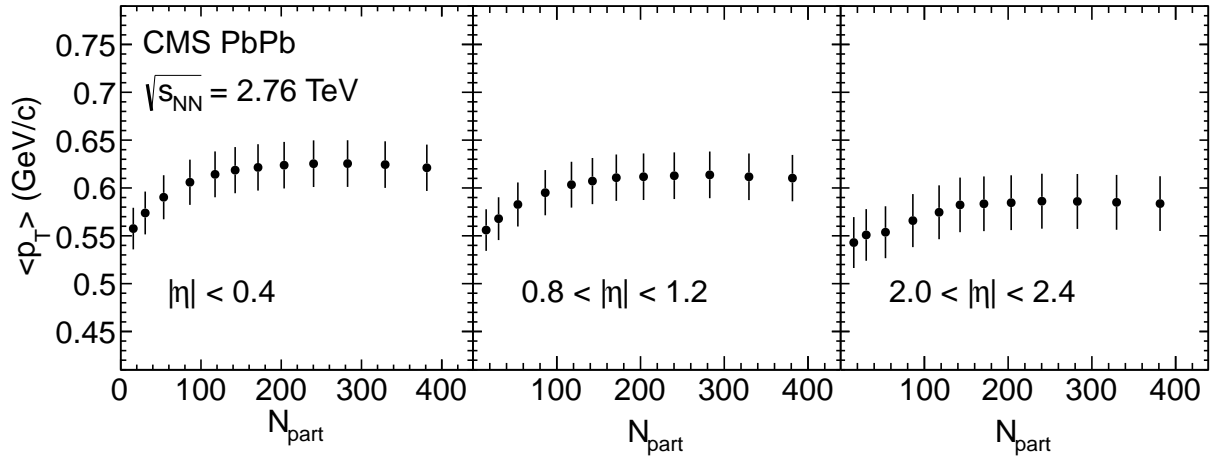


Figure 16: Mean transverse momentum of the charged-particle spectra as a function of N_{part} in three pseudorapidity intervals marked in the figure. The error bars represent the quadratic sum of the statistical and systematic uncertainties.

bottom panels in Fig. 20 show the ratios of the fits to the CMS data to the actual measurements from CMS and STAR. The error bars represent the statistical uncertainties. The systematic uncertainties from the CMS and STAR measurements are added in quadrature and plotted as shaded boxes. At low p_T , the $v_2(p_T)$ values measured by CMS are larger than in the STAR data, but the relative deviations are smaller than 5% for the four-particle cumulant method, and are of the order 10–15% for the two-particle cumulant method. Taken together, the comparisons to the RHIC results in Figs. 19 and 20 indicate only a moderate increase in $v_2(p_T)$ at low p_T from the highest RHIC energy to the LHC, despite the large increase in the center-of-mass energy.

In Fig. 21, we examine the $\sqrt{s_{NN}}$ dependence of the integrated v_2 from mid-central collisions spanning $\sqrt{s_{NN}} = 4.7$ GeV to $\sqrt{s_{NN}} = 2.76$ TeV. The CMS measurement is obtained with the event-plane method in the 20–30% centrality class by extrapolating the $v_2(p_T)$ and the charged-particle spectra down to $p_T = 0$. In the extrapolation it is assumed that $v_2(0) = 0$, and the charged-particle yield is constrained to match the $dN_{\text{ch}}/d\eta$ values measured by CMS [75]. The low-energy data are from Refs. [20, 23, 49, 76–81], as compiled in Ref. [79] and tabulated in Ref. [76]. The error bars for the low-energy data represent the statistical uncertainties. For the CMS data the error bar is the quadrature sum of the statistical and systematic uncertainties. The integrated v_2 values increase approximately logarithmically with $\sqrt{s_{NN}}$ over the full energy range, with a 20–30% increase from the highest RHIC energy to that of the LHC. This has contributions from the increase in the mean p_T of the charged-particle spectra with $\sqrt{s_{NN}}$, shown in Fig. 22, and from the moderate increase in the $v_2(p_T)$ distributions at low p_T , shown in Fig. 19. We note that the centrality selections, the collision species, and the methods employed in the integrated v_2 measurements are not identical in all experiments, so the comparison presented in Fig. 21 is only approximate. Further comparisons to results from lower energies are presented in Figs. 23–25.

In ideal hydrodynamics, the eccentricity-scaled elliptic flow is constant over a broad range of impact parameters; deviations from this behavior are expected in peripheral collisions, in which the system freezes out before the elliptic flow fully builds up and saturates [32]. A weak centrality and beam-energy dependence is expected through variations in the equation-of-state. In addition, the system is also affected by viscosity, both in the sQGP and hadronic stages [22, 68, 83, 84] of its evolution. Therefore, the centrality and $\sqrt{s_{NN}}$ dependence of v_2/ϵ

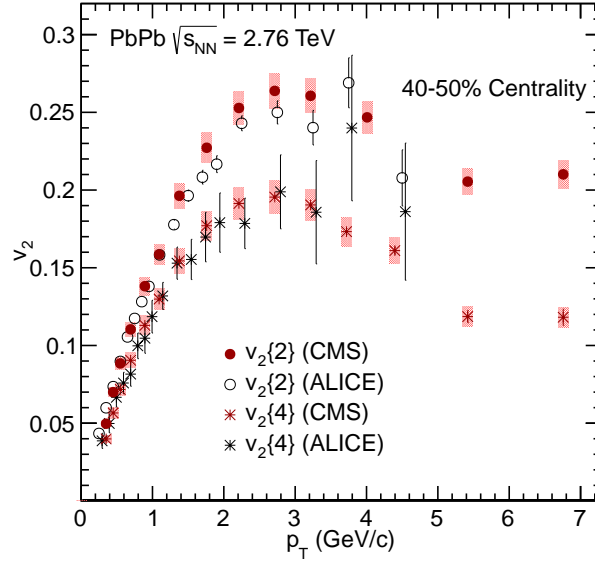


Figure 17: (Color online) The values of $v_2\{2\}$ and $v_2\{4\}$ obtained with the cumulant method, as a function of p_T from CMS (closed symbols) and ALICE (open symbols) [13], measured in the range $|\eta| < 0.8$ for the 40–50% centrality class. The error bars show the statistical uncertainties, and the boxes give the systematic uncertainties in the CMS measurement.

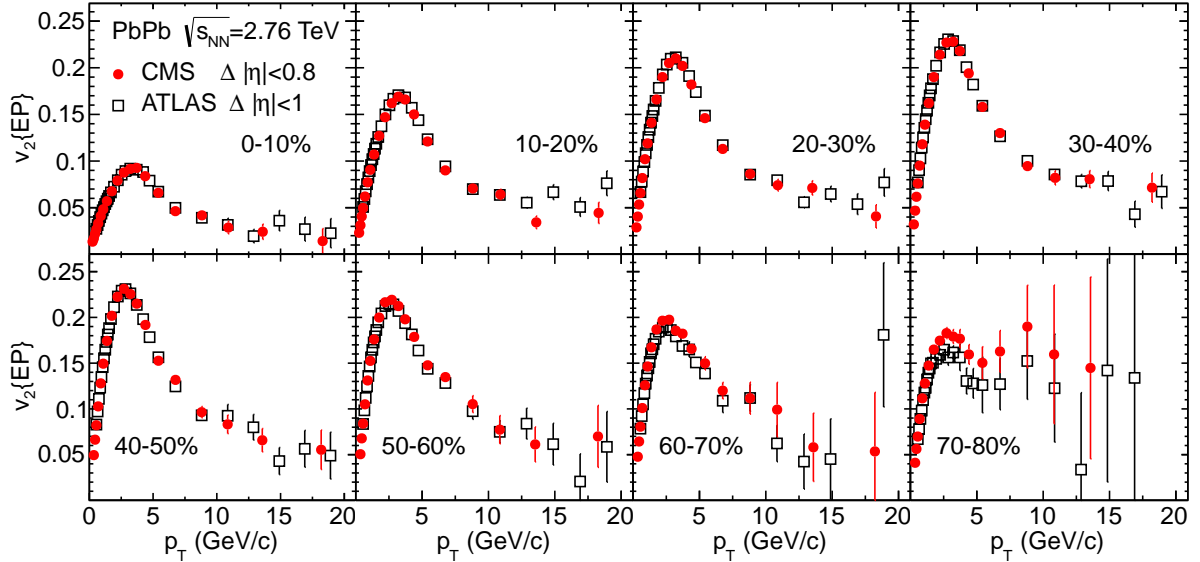


Figure 18: (Color online) Comparison of results for $v_2(p_T)$ obtained with the event-plane method from CMS (closed symbols) and ATLAS (open symbols) for the centrality classes marked in the figure. The error bars show the statistical and systematic uncertainties added in quadrature.

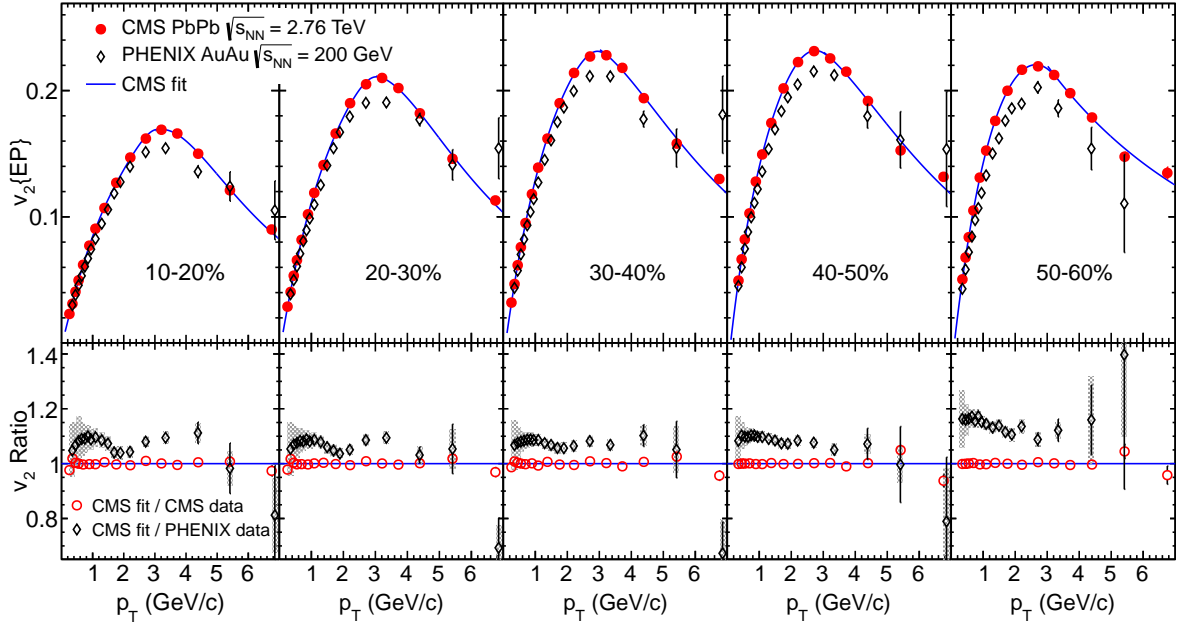


Figure 19: (Color online) Top panels: Comparison of $v_2(p_T)$ using the event-plane method as measured by CMS (solid circles) at $\sqrt{s_{NN}} = 2.76$ TeV, and PHENIX [73] (open diamonds) at $\sqrt{s_{NN}} = 200$ GeV for mid-rapidity ($|\eta| < 0.8$ and $|\eta| < 0.35$, respectively). The error bars represent the statistical uncertainties. The solid line is a fit to the CMS data. Bottom panels: Ratios of the CMS fit to the PHENIX data (open diamonds) and to the CMS data (open circles). The error bars show the statistical uncertainties, while the shaded boxes give the quadrature sum of the CMS and PHENIX systematic uncertainties.

can be used to extract the ratio of the shear viscosity to the entropy density of the system.

In Fig. 23, the integrated v_2 obtained from the event-plane method is divided by the eccentricity of the collisions and plotted as a function of N_{part} , which is derived from the centrality of the event. The result is compared to lower-energy AuAu and CuCu measurements from the PHOBOS experiment [34]. For the CMS measurement, the value of v_2 is divided by the participant eccentricity ϵ_{part} since the event-plane resolution factor shown in Fig. 4 is greater than 0.6 for all but the most central and most peripheral event selections in our analysis. It has been argued [34, 37] that for lower-resolution parameters, the event-plane method measures the r.m.s. of the azimuthal anisotropy, rather than the mean, and therefore, the relevant eccentricity parameter in this case should be the second-order cumulant eccentricity $\epsilon\{2\} \equiv \sqrt{\langle \epsilon_{\text{part}}^2 \rangle}$. Thus, the comparison with the PHOBOS v_2 results, which were obtained with low event-plane resolution, is done by implementing this scaling using the data from Ref. [34]. An approximately 25% increase in the integrated v_2 scaled by the eccentricity between RHIC and LHC energies is observed, and with a similar N_{part} dependence.

It was previously observed [34, 79, 85] that the v_2/ϵ values obtained in different collision systems and varying beam energies scale with the charged-particle rapidity density per unit transverse overlap area $(1/S)(dN_{\text{ch}}/dy)$, which is proportional to the initial entropy density. In addition, it has been pointed out [69] that in this representation the sensitivity to the modeling of the initial conditions of the heavy-ion collisions is largely removed, thus enabling the extraction of the shear viscosity to the entropy density ratio from the data through the comparison

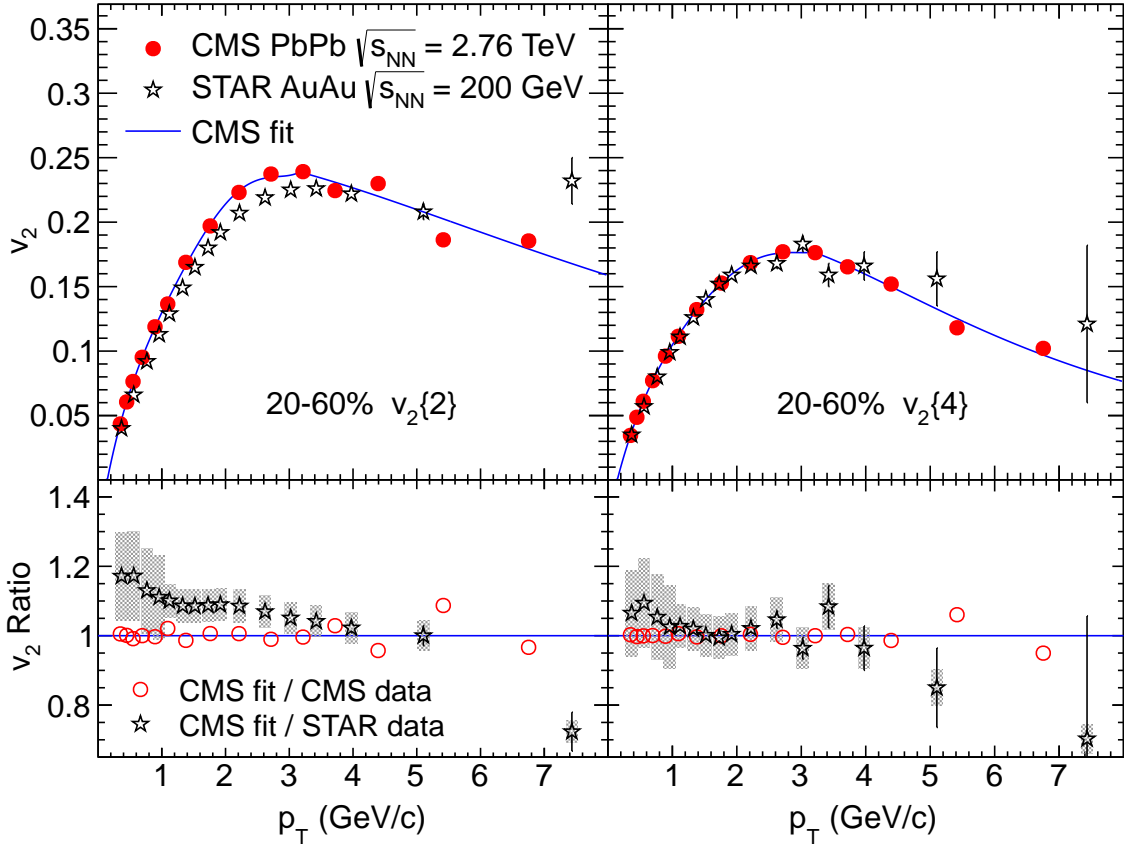


Figure 20: (Color online) Top panels: Comparison of $v_2(p_T)$ using the two-particle (left) and the four-particle (right) cumulant method as measured by CMS (solid circles) at $\sqrt{s_{NN}} = 2.76$ TeV, and STAR [74] (open stars) at $\sqrt{s_{NN}} = 200$ GeV at mid-rapidity ($|\eta| < 0.8$ and $|\eta| < 1.3$, respectively). The error bars represent the statistical uncertainties. The line is a fit to the CMS data. Bottom panels: Ratios of the CMS fit values to the STAR data (open diamonds) and to the CMS data (open circles). The error bars show the statistical uncertainties, while the shaded boxes give the quadrature sum of the CMS and STAR systematic uncertainties.

with viscous hydrodynamics calculations. With the factor of 2.1 increase in the charged-particle pseudorapidity density per participant pair, $(dN_{ch}/d\eta)/(N_{part}/2)$, from the highest RHIC energy to the LHC [75, 86], this scaling behavior can be tested over a much broader range of initial entropy densities. In Fig. 24, we compare the CMS results for v_2/ϵ from the event-plane method to results from the PHOBOS experiment [34] for CuCu and AuAu collisions with $\sqrt{s_{NN}} = 62.4$ GeV and 200 GeV.

At lower energies, the scaling has been examined using the charged-particle rapidity density dN_{ch}/dy [34, 79, 85]. However, since we do not identify the species of charged particles in this analysis, we perform the comparison using $(1/S)(dN_{ch}/d\eta)$ to avoid introducing uncertainties related to assumptions about the detailed behavior of the identified particle transverse momentum spectra that are needed to perform this conversion. In Fig. 24, the charged-particle pseudorapidity density $dN_{ch}/d\eta$ measured by CMS [75] is used, and the value of the integrated v_2 for the ranges $0 < p_T < 3$ GeV/c and $|\eta| < 0.8$. The transverse nuclear-overlap area S and the participant eccentricity are listed in Table 1. The PHOBOS results from Ref. [34] used dN_{ch}/dy , and applied two factors to perform the Jacobian transformation from $dN_{ch}/d\eta$: the x

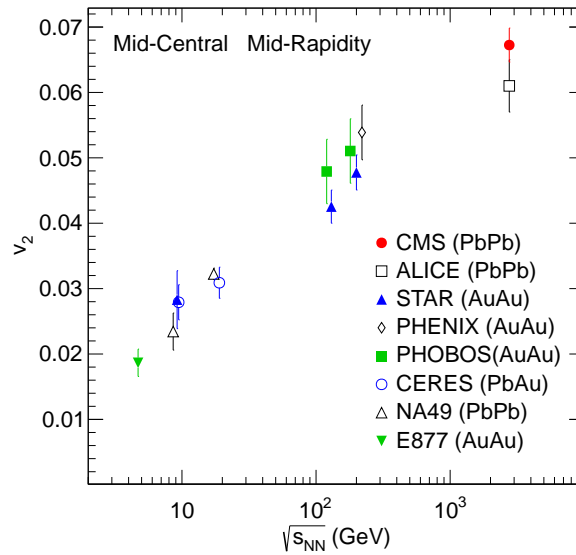


Figure 21: (Color online) The CMS integrated v_2 values for 20–30% centrality from the range $|\eta| < 0.8$ and $0 < p_T < 3 \text{ GeV}/c$ obtained using the event-plane method is compared as a function of $\sqrt{s_{NN}}$ to results at mid-rapidity and similar centrality from ALICE [13], STAR [76], PHENIX [23], PHOBOS [49, 77, 78], NA49 [79], E877 [80], and CERES [81]. The error bars for the lower-energy results represent statistical uncertainties; for the CMS and ALICE measurements the statistical and systematic uncertainties are added in quadrature.

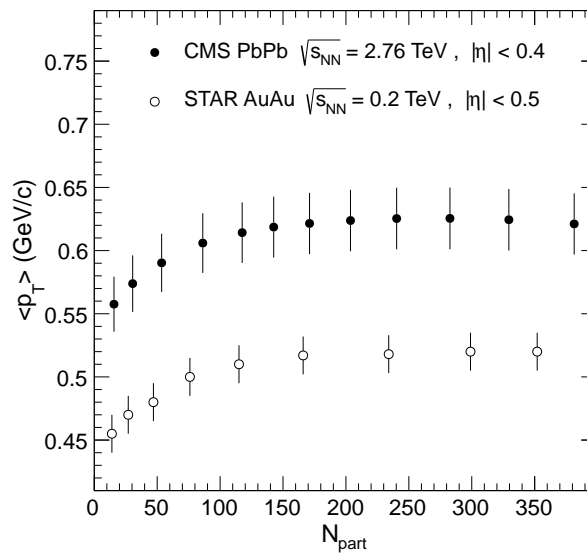


Figure 22: Mean transverse momentum of the charged-particle spectra as a function of N_{part} measured by CMS in PbPb collisions at $\sqrt{s_{NN}} = 2.76 \text{ TeV}$ (closed circles) and by STAR [82] in AuAu collisions at $\sqrt{s_{NN}} = 200 \text{ GeV}$ (open circles). The error bars represent the quadratic sum of statistical and systematic uncertainties.

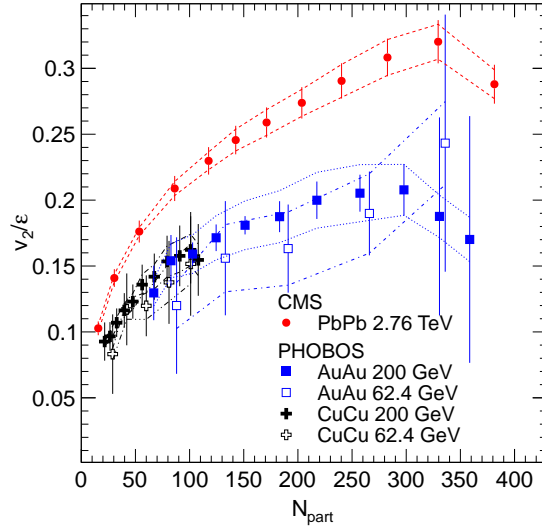


Figure 23: (Color online) The CMS integrated v_2 values from the event-plane method divided by the participant eccentricity as a function of N_{part} with $|\eta| < 0.8$ and $0 < p_T < 3 \text{ GeV}/c$. These results are compared with those from PHOBOS [34] for different nuclear species and collision energies. The PHOBOS v_2 values are divided by the cumulant eccentricity $\epsilon\{2\}$ (see text). The error bars give the statistical and systematic uncertainties in the v_2 measurements added in quadrature. The dashed lines represent the systematic uncertainties in the eccentricity determination.

axis was scaled by a factor 1.15, and the y axis by 0.9. Both of these factors are reversed in order to compare the CMS and PHOBOS measurements in Fig. 24. As in Fig. 23, the PHOBOS data are scaled by $\epsilon\{2\}$, while the CMS data are scaled by the participant eccentricity ϵ_{part} , taking into account the event-plane resolution factors in the two measurements. The CMS result extends to very peripheral collisions (70–80% centrality), which allows for a significant overlap in the transverse charged-particle density measured at RHIC and LHC. Despite the large systematic uncertainties quoted for the PHOBOS measurements, the data are in good agreement over the common $(1/S)(dN_{\text{ch}}/d\eta)$ range. A smooth increase in v_2/ϵ proportional to the transverse particle density is observed over the entire measured range, except for a small decrease in the most central collisions in both the RHIC and LHC data. The theoretical predictions [68, 71, 83] for the $\sqrt{s_{NN}}$ dependence of the transverse-particle-density scaling of v_2/ϵ differ, and do not generally predict a universal behavior. The data presented here provide constraints on the model descriptions of the dynamical evolution of the system, and thus should aid the reliable extraction of the transport properties of the hot QCD medium from data.

The $v_2(\eta)$ results can be used to test theoretical descriptions of the longitudinal dynamics in the expanding system, as they have been shown to be sensitive to the choice of the initial conditions, the event-by-event fluctuations in the eccentricity, and the viscosity in the sQGP and the hadronic stages of the system evolution [39, 87]. The PHOBOS experiment observed [41] that the elliptic flow measured over a broad range of collision energies ($\sqrt{s_{NN}} = 19.6, 62.4, 130, \text{ and } 200 \text{ GeV}$) exhibited longitudinal scaling extending over several units of pseudorapidity when viewed in the rest frame of one of the incident nuclei. A similar phenomenon for soft-particle yields and spectra is known as limiting fragmentation [88]. Furthermore, with increasing $\sqrt{s_{NN}}$, this beam-energy independence of $v_2(\eta)$ was found to extend over an increasingly wider pseudorapidity range [41]. To investigate the potential continuation of ex-

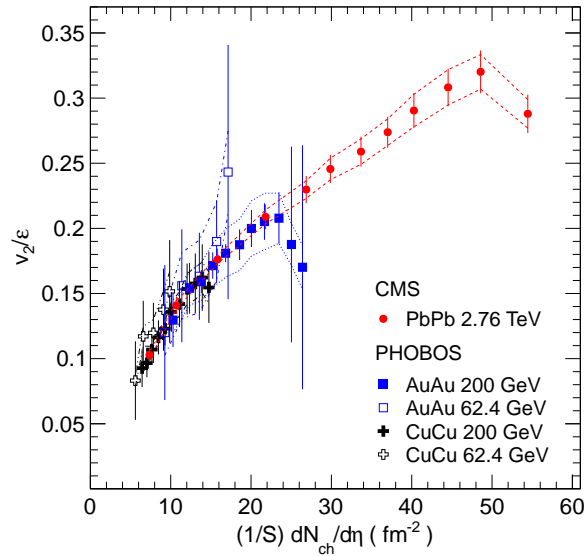


Figure 24: (Color online) Eccentricity-scaled v_2 as a function of the transverse charged-particle density from CMS and PHOBOS [34]. The error bars include both statistical and systematic uncertainties in v_2 . The dashed lines represent the systematic uncertainties in the eccentricity determination.

tended longitudinal scaling of the elliptic flow to LHC energies, in Fig. 25 we compare the pseudorapidity dependence of $v_2(\eta)$ measured by CMS with that measured by PHOBOS at $\sqrt{s_{NN}} = 200$ GeV in three centrality intervals. Neither the CMS nor the PHOBOS measurements are performed using identified particles. The pseudorapidity η^+ (η^-) of the particles in the rest frame of the nuclei moving in the positive (negative) direction is approximated by $\eta^\pm = \eta \pm y_{\text{beam}}$, where η is the pseudorapidity of the particles in the center-of-mass frame, and $y_{\text{beam}} = \text{arccosh}(E_{\text{lab}}/Am_Nc^2) \approx \ln(\sqrt{s_{NN}} [\text{GeV}])$, with E_{lab} denoting the energy of the beam in the laboratory frame, A the nuclear mass number, and m_N the nucleon mass. In Fig. 25, the left (right) half of each plot depicts v_2 in the rest frame of the beam moving in the positive (negative) lab direction. The PHOBOS $v_2(\eta)$ results are from the hit-based analysis from Fig. 4 in Ref. [77]. The CMS results are obtained with the event-plane method in 0.4-unit-wide bins of pseudorapidity by averaging the corresponding $v_2(p_T)$ distributions over the range $0 < p_T < 3$ GeV/ c and folding in the efficiency-corrected charged-particle spectra. A comparable centrality interval (2.5–15% in CMS, and 3–15% in PHOBOS) is analyzed for the most central collisions, while for mid-central (15–25%) and more peripheral (25–50%) collisions, the centrality selections are the same in both experiments. In Fig. 25, the statistical uncertainties are shown as error bars, while the systematic ones are represented by the shaded boxes surrounding the points. The CMS data cover 4.8 units of pseudorapidity, but do not overlap in pseudorapidity with the PHOBOS data when plotted in the rest frames of the colliding nuclei. The CMS results show weaker pseudorapidity dependence than observed in the PHOBOS measurement. The data suggest a nearly boost-invariant region that is several units wide for central events but considerably smaller for peripheral ones. It has been noted [89] that if the QCD matter produced at mid-rapidity at RHIC is in local equilibrium, then deviations from the triangular shape of $v_2(\eta)$ observed in the PHOBOS measurements [41] would be expected around mid-rapidity at LHC energies. Detailed comparisons of theoretical calculations to the results presented here can give new insights into the nature of the matter produced at both RHIC and LHC energies.

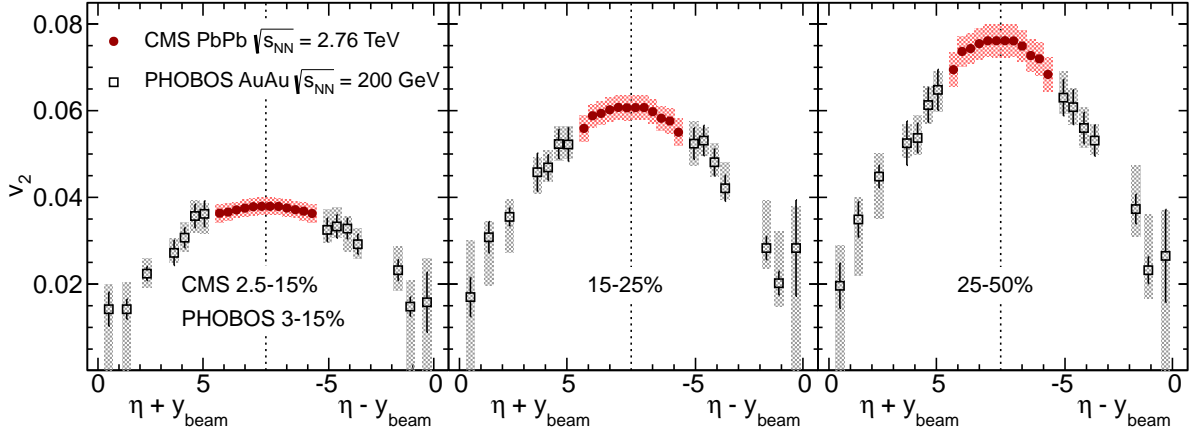


Figure 25: (Color online) Measurements of v_2 as a function of the pseudorapidity of particles in the rest frame of the colliding nuclei $\eta \pm y_{\text{beam}}$ from CMS (closed symbols) and PHOBOS (open symbols) [77] in three centrality intervals. The error bars show the statistical uncertainties and the boxes give the systematic ones.

5 Summary

Detailed measurements of the charged-particle azimuthal anisotropies in $\sqrt{s_{NN}} = 2.76$ TeV PbPb collisions and comparisons to lower collision energy results have been presented. The results cover a broad kinematic range: $0.3 < p_T < 20$ GeV/c, $|\eta| < 2.4$, and 12 centrality classes from 0 to 80%. The measurements employ four different methods that have different sensitivities to fluctuations in the initial conditions and nonflow correlations. The systematic comparison between the methods provides the possibility to explore the underlying physics processes that cause these differences.

The elliptic anisotropy parameter $v_2(p_T)$ for $|\eta| < 0.8$ is found to increase with p_T up to $p_T \approx 3$ GeV/c, and then to decrease in the range $3 < p_T < 10$ GeV/c. For transverse momenta of $10 < p_T < 20$ GeV/c, no strong dependence of v_2 on p_T is observed. The study of the high- p_T azimuthal anisotropy in charged-particle production may constrain the theoretical descriptions of parton energy loss and its dependence on the path-length traveled through the medium.

The shapes of the $v_2(p_T)$ distributions are found to be similar to those measured at RHIC. At low p_T , only a moderate increase (5–15%) is observed in the comparison between results obtained at the highest RHIC energy and the LHC, despite the large increase in the center-of-mass energy. The integrated v_2 at mid-rapidity and in mid-central collisions (20–30% centrality) increases approximately logarithmically with $\sqrt{s_{NN}}$. An increase by 20–30% from the highest RHIC energy to that of the LHC is observed, which is mostly due to the increase in the mean p_T of the underlying charged-particle spectra. The integrated v_2 signal increases from the most central collisions to the 40–50% centrality range, after which a decrease is observed. Conversely, the values of $\langle p_T \rangle$ increase with N_{part} up to $N_{\text{part}} \approx 150$ (from the most peripheral collisions up to centrality $\approx 35\%$) and then saturate, indicating similar freeze-out conditions in the more central collisions. The different methods of measuring v_2 give consistent results over a broad range of centrality, when scaled by their respective participant eccentricity moments. Deviations from this scaling are observed in the most central collisions and in peripheral (centrality above 50%) collisions. The eccentricity-scaled v_2 at mid-rapidity is measured to be approximately linear in the transverse particle density, and a universal scaling is observed in the comparison of re-

sults from different collision systems and center-of-mass energies measured at RHIC and the LHC. The value of $v_2(\eta)$ is found to be weakly dependent on pseudorapidity in central collisions; for peripheral collisions the values of $v_2(\eta)$ gradually decrease as the pseudorapidity increases. The results presented here provide further input to the theoretical models of relativistic nucleus-nucleus collisions and will aid in determining the initial conditions of the system, the degree of equilibration, and the transport properties of hot QCD matter produced in heavy-ion collisions.

Acknowledgments

We congratulate our colleagues in the CERN accelerator departments for the excellent performance of the LHC and thank the technical and administrative staffs at CERN and at other CMS institutes for their contributions to the success of the CMS effort. In addition, we gratefully acknowledge the computing centres and personnel of the Worldwide LHC Computing Grid for delivering so effectively the computing infrastructure essential to our analyses. Finally, we acknowledge the enduring support for the construction and operation of the LHC and the CMS detector provided by the following funding agencies: the Austrian Federal Ministry of Science and Research; the Belgian Fonds de la Recherche Scientifique, and Fonds voor Wetenschappelijk Onderzoek; the Brazilian Funding Agencies (CNPq, CAPES, FAPERJ, and FAPESP); the Bulgarian Ministry of Education, Youth and Science; CERN; the Chinese Academy of Sciences, Ministry of Science and Technology, and National Natural Science Foundation of China; the Colombian Funding Agency (COLCIENCIAS); the Croatian Ministry of Science, Education and Sport; the Research Promotion Foundation, Cyprus; the Ministry of Education and Research, Recurrent financing contract SF0690030s09 and European Regional Development Fund, Estonia; the Academy of Finland, Finnish Ministry of Education and Culture, and Helsinki Institute of Physics; the Institut National de Physique Nucléaire et de Physique des Particules / CNRS, and Commissariat à l'Énergie Atomique et aux Énergies Alternatives / CEA, France; the Bundesministerium für Bildung und Forschung, Deutsche Forschungsgemeinschaft, and Helmholtz-Gemeinschaft Deutscher Forschungszentren, Germany; the General Secretariat for Research and Technology, Greece; the National Scientific Research Foundation, and National Office for Research and Technology, Hungary; the Department of Atomic Energy and the Department of Science and Technology, India; the Institute for Studies in Theoretical Physics and Mathematics, Iran; the Science Foundation, Ireland; the Istituto Nazionale di Fisica Nucleare, Italy; the Korean Ministry of Education, Science and Technology and the World Class University program of NRF, Korea; the Lithuanian Academy of Sciences; the Mexican Funding Agencies (CINVESTAV, CONACYT, SEP, and UASLP-FAI); the Ministry of Science and Innovation, New Zealand; the Pakistan Atomic Energy Commission; the Ministry of Science and Higher Education and the National Science Centre, Poland; the Fundação para a Ciência e a Tecnologia, Portugal; JINR (Armenia, Belarus, Georgia, Ukraine, Uzbekistan); the Ministry of Education and Science of the Russian Federation, the Federal Agency of Atomic Energy of the Russian Federation, Russian Academy of Sciences, and the Russian Foundation for Basic Research; the Ministry of Science and Technological Development of Serbia; the Secretaría de Estado de Investigación, Desarrollo e Innovación and Programa Consolider-Ingenio 2010, Spain; the Swiss Funding Agencies (ETH Board, ETH Zurich, PSI, SNF, UniZH, Canton Zurich, and SER); the National Science Council, Taipei; the Thailand Center of Excellence in Physics, the Institute for the Promotion of Teaching Science and Technology and National Electronics and Computer Technology Center; the Scientific and Technical Research Council of Turkey, and Turkish Atomic Energy Authority; the Science and Technology Facilities Council, UK; the US Department of Energy, and the US National Science Foundation.

Individuals have received support from the Marie-Curie programme and the European Research Council (European Union); the Leventis Foundation; the A. P. Sloan Foundation; the Alexander von Humboldt Foundation; the Belgian Federal Science Policy Office; the Fonds pour la Formation à la Recherche dans l'Industrie et dans l'Agriculture (FRIA-Belgium); the Agentschap voor Innovatie door Wetenschap en Technologie (IWT-Belgium); the Ministry of Education, Youth and Sports (MEYS) of Czech Republic; the Council of Science and Industrial Research, India; the Compagnia di San Paolo (Torino); and the HOMING PLUS programme of Foundation for Polish Science, cofinanced from European Union, Regional Development Fund.

References

- [1] PHENIX Collaboration, "Formation of dense partonic matter in relativistic nucleus-nucleus collisions at RHIC: Experimental evaluation by the PHENIX collaboration", *Nucl. Phys. A* **757** (2005) 184, doi:10.1016/j.nuclphysa.2005.03.086.
- [2] STAR Collaboration, "Experimental and theoretical challenges in the search for the quark gluon plasma: The STAR Collaboration's critical assessment of the evidence from RHIC collisions", *Nucl. Phys. A* **757** (2005) 102, doi:10.1016/j.nuclphysa.2005.03.085.
- [3] PHOBOS Collaboration, "The PHOBOS perspective on discoveries at RHIC", *Nucl. Phys. A* **757** (2005) 28, doi:10.1016/j.nuclphysa.2005.03.084.
- [4] E. V. Shuryak, "What RHIC experiments and theory tell us about properties of quark-gluon plasma?", *Nucl. Phys. A* **750** (2005) 64, doi:10.1016/j.nuclphysa.2004.10.022.
- [5] M. Gyulassy and L. McLerran, "New forms of QCD matter discovered at RHIC", *Nucl. Phys. A* **750** (2005) 30, doi:10.1016/j.nuclphysa.2004.10.034.
- [6] A. M. Poskanzer and S. A. Voloshin, "Methods for analyzing anisotropic flow in relativistic nuclear collisions", *Phys. Rev. C* **58** (1998) 1671, doi:10.1103/PhysRevC.58.1671.
- [7] J.-Y. Ollitrault, "Anisotropy as a signature of transverse collective flow", *Phys. Rev. D* **46** (1992) 229, doi:10.1103/PhysRevD.46.229.
- [8] H. Sorge, "Highly sensitive centrality dependence of elliptic flow: A novel signature of the phase transition in QCD", *Phys. Rev. Lett.* **82** (1999) 2048, doi:10.1103/PhysRevLett.82.2048.
- [9] PHENIX Collaboration, "Saturation of azimuthal anisotropy in Au + Au collisions at $\sqrt{s_{NN}} = 62$ GeV to 200 GeV", *Phys. Rev. Lett.* **94** (2005) 232302, doi:10.1103/PhysRevLett.94.232302.
- [10] STAR Collaboration, "Directed and elliptic flow of charged particles in Cu+Cu collisions at $\sqrt{s_{NN}} = 22.4$ GeV", *Phys. Rev. C* **85** (2012) 014901, doi:10.1103/PhysRevC.85.014901.
- [11] U. Heinz and P. F. Kolb, "Early thermalization at RHIC", *Nucl. Phys. A* **702** (2002) 269, doi:10.1016/S0375-9474(02)00714-5.

- [12] P. F. Kolb and U. Heinz, "Hydrodynamic description of ultrarelativistic heavy-ion collisions", in *Quark-Gluon Plasma*, R. Hwa and X.-N. Wang, eds., p. 634. World Scientific, Singapore, 2004.
- [13] ALICE Collaboration, "Elliptic Flow of Charged Particles in Pb-Pb Collisions at $\sqrt{s_{NN}} = 2.76$ TeV", *Phys. Rev. Lett.* **105** (2010) 252302, doi:10.1103/PhysRevLett.105.252302.
- [14] ATLAS Collaboration, "Measurement of the pseudorapidity and transverse momentum dependence of the elliptic flow of charged particles in lead-lead collisions at $\sqrt{s_{NN}} = 2.76$ TeV with the ATLAS detector", *Phys. Lett. B* **707** (2012) 330, doi:10.1016/j.physletb.2011.12.056.
- [15] D. A. Teaney, "Viscous Hydrodynamics and the Quark Gluon Plasma", in *Quark-Gluon Plasma 4*, R. Hwa and X.-N. Wang, eds., p. 207. World Scientific, Singapore, 2010.
- [16] P. Romatschke, "New Developments in Relativistic Viscous Hydrodynamics", *Int. J. Mod. Phys. E* **19** (2010) 1, doi:10.1142/S0218301310014613.
- [17] PHENIX Collaboration, "Elliptic Flow of Identified Hadrons in Au+Au Collisions at $\sqrt{s_{NN}} = 200$ GeV", *Phys. Rev. Lett.* **91** (2003) 182301, doi:10.1103/PhysRevLett.91.182301.
- [18] STAR Collaboration, "Particle dependence of azimuthal anisotropy and nuclear modification of particle production at moderate p_T in Au + Au collisions at $\sqrt{s_{NN}} = 200$ GeV", *Phys. Rev. Lett.* **92** (2004) 052302, doi:10.1103/PhysRevLett.92.052302.
- [19] PHENIX Collaboration, "Elliptic flow for phi mesons and (anti)deuterons in Au + Au collisions at $\sqrt{s_{NN}} = 200$ GeV", *Phys. Rev. Lett.* **99** (2007) 052301, doi:10.1103/PhysRevLett.99.052301.
- [20] STAR Collaboration, "Mass, quark-number, and $\sqrt{s_{NN}}$ dependence of the second and fourth flow harmonics in ultra-relativistic nucleus nucleus collisions", *Phys. Rev. C* **75** (2007) 054906, doi:10.1103/PhysRevC.75.054906.
- [21] P. Huovinen and P. V. Ruuskanen, "Hydrodynamic Models for Heavy Ion Collisions", *Ann. Rev. Nucl. Part. Sci.* **56** (2006) 163, doi:10.1146/annurev.nucl.54.070103.181236.
- [22] U. W. Heinz, "Early collective expansion: Relativistic hydrodynamics and the transport properties of QCD matter", in *Relativistic Heavy Ion Physics, Landolt-Boernstein New Series, Vol. I/23*, R. Stock, ed., ch. 5. Springer Verlag, New York, 2010.
- [23] PHENIX Collaboration, "Scaling Properties of Azimuthal Anisotropy in Au+Au and Cu+Cu Collisions at $\sqrt{s_{NN}} = 200$ GeV", *Phys. Rev. Lett.* **98** (2007) 162301, doi:10.1103/PhysRevLett.98.162301.
- [24] V. Greco, C. M. Ko, and P. Lévai, "Partonic coalescence in relativistic heavy ion collisions", *Phys. Rev. C* **68** (2003) 034904, doi:10.1103/PhysRevC.68.034904.
- [25] R. J. Fries et al., "Hadron production in heavy ion collisions: Fragmentation and recombination from a dense parton phase", *Phys. Rev. C* **68** (2003) 044902, doi:10.1103/PhysRevC.68.044902.

- [26] R. C. Hwa and C. B. Yang, "Recombination of shower partons in fragmentation processes", *Phys. Rev. C* **70** (2004) 024904, doi:10.1103/PhysRevC.70.024904.
- [27] B. Müller, "Hadronic signals of deconfinement at RHIC", *Nucl. Phys. A* **750** (2005) 84, doi:10.1016/j.nuclphysa.2004.12.067.
- [28] M. Gyulassy, I. Vitev, and X.-N. Wang, "High p_T Azimuthal Asymmetry in Noncentral A+A at RHIC", *Phys. Rev. Lett.* **86** (2001) 2537, doi:10.1103/PhysRevLett.86.2537.
- [29] PHENIX Collaboration, "High- p_T π^0 production with respect to the reaction plane in Au+Au collisions at $\sqrt{s_{NN}} = 200$ GeV", *Phys. Rev. C* **80** (2009) 054907, doi:10.1103/PhysRevC.80.054907.
- [30] PHENIX Collaboration, "Azimuthal anisotropy of neutral pion production in Au+Au collisions at $\sqrt{s_{NN}} = 200$ GeV: Path-length dependence of jet quenching and the role of initial geometry", *Phys. Rev. Lett.* **105** (2010) 142301, doi:10.1103/PhysRevLett.105.142301.
- [31] S. A. Bass et al., "Systematic comparison of jet energy-loss schemes in a realistic hydrodynamic medium", *Phys. Rev. C* **79** (2009) 024901, doi:10.1103/PhysRevC.79.024901.
- [32] P. F. Kolb, J. Sollfrank, and U. W. Heinz, "Anisotropic transverse flow and the quark hadron phase transition", *Phys. Rev. C* **62** (2000) 054909, doi:10.1103/PhysRevC.62.054909.
- [33] PHOBOS Collaboration, "Event-by-Event Fluctuations of Azimuthal Particle Anisotropy in Au + Au Collisions at $\sqrt{s_{NN}} = 200$ GeV", *Phys. Rev. Lett.* **104** (2010) 142301, doi:10.1103/PhysRevLett.104.142301.
- [34] PHOBOS Collaboration, "Importance of correlations and fluctuations on the initial source eccentricity in high-energy nucleus-nucleus collisions", *Phys. Rev. C* **77** (2008) 014906, doi:10.1103/PhysRevC.77.014906.
- [35] R. S. Bhalerao and J.-Y. Ollitrault, "Eccentricity fluctuations and elliptic flow at RHIC", *Phys. Lett. B* **641** (2006) 260, doi:10.1016/j.physletb.2006.08.055.
- [36] S. A. Voloshin et al., "Elliptic flow in the Gaussian model of eccentricity fluctuations", *Phys. Lett. B* **659** (2008) 537, doi:10.1016/j.physletb.2007.11.043.
- [37] J.-Y. Ollitrault, A. M. Poskanzer, and S. A. Voloshin, "Effect of flow fluctuations and nonflow on elliptic flow methods", *Phys. Rev. C* **80** (2009) 014904, doi:10.1103/PhysRevC.80.014904.
- [38] Z. Qiu and U. W. Heinz, "Event-by-event shape and flow fluctuations of relativistic heavy-ion collision fireballs", *Phys. Rev. C* **84** (2011) 024911, doi:10.1103/PhysRevC.84.024911.
- [39] T. Hirano et al., "Hadronic dissipative effects on elliptic flow in ultrarelativistic heavy-ion collisions.", *Phys. Lett. B* **636** (2006) 299, doi:10.1016/j.physletb.2006.03.060.
- [40] W. Busza, "Extended Longitudinal Scaling: Direct evidence of saturation", *Nucl. Phys. A* **854** (2011) 57, doi:10.1016/j.nuclphysa.2010.12.015.

- [41] PHOBOS Collaboration, "Energy dependence of elliptic flow over a large pseudorapidity range in Au + Au collisions at RHIC", *Phys. Rev. Lett.* **94** (2005) 122303, doi:10.1103/PhysRevLett.94.122303.
- [42] N. Borghini, P. M. Dinh, and J.-Y. Ollitrault, "Flow analysis from multiparticle azimuthal correlations", *Phys. Rev. C* **64** (2001) 054901, doi:10.1103/PhysRevC.64.054901.
- [43] R. S. Bhalerao, N. Borghini, and J.-Y. Ollitrault, "Analysis of anisotropic flow with Lee-Yang zeroes", *Nucl. Phys. A* **727** (2003) 373, doi:10.1016/j.nuclphysa.2003.08.007.
- [44] N. Borghini, R. S. Bhalerao, and J.-Y. Ollitrault, "Anisotropic flow from Lee-Yang zeroes: A practical guide", *J. Phys. G* **30** (2004) S1213, doi:10.1088/0954-3899/30/8/092.
- [45] CMS Collaboration, "The CMS experiment at the CERN LHC", *JINST* **3** (2008) S08004, doi:10.1088/1748-0221/3/08/S08004.
- [46] Ø. Djuvsland and J. Nystrand, "Single and double photonuclear excitations in Pb+Pb collisions at $\sqrt{s_{NN}} = 2.76$ TeV at the CERN Large Hadron Collider", *Phys. Rev. C* **83** (2011) 041901, doi:10.1103/PhysRevC.83.041901.
- [47] CMS Collaboration, "Transverse-momentum and pseudorapidity distributions of charged hadrons in pp collisions at $\sqrt{s} = 7$ TeV", *Phys. Rev. Lett.* **105** (2010) 022002, doi:10.1103/PhysRevLett.105.022002.
- [48] M. L. Miller et al., "Glauber Modeling in High Energy Nuclear Collisions", *Ann. Rev. Nucl. Part. Sci.* **57** (2007) 205, doi:10.1146/annurev.nucl.57.090506.123020.
- [49] PHOBOS Collaboration, "System Size, Energy, Pseudorapidity, and Centrality Dependence of Elliptic Flow", *Phys. Rev. Lett.* **98** (2007) 242302, doi:10.1103/PhysRevLett.98.242302.
- [50] B. Alver et al., "The PHOBOS Glauber Monte Carlo", (2008). arXiv:0805.4411.
- [51] H. De Vries, C. W. De Jager, and C. De Vries, "Nuclear charge and magnetization density distribution parameters from elastic electron scattering", *Atom. Data Nucl. Data Tabl.* **36** (1987) 495, doi:10.1016/S0092-640X(74)80002-1.
- [52] Particle Data Group Collaboration, "Review of particle physics", *J. Phys. G* **37** (2010) 075021, doi:10.1088/0954-3899/37/7A/075021.
- [53] CMS Collaboration, "Observation and studies of jet quenching in PbPb collisions at nucleon-nucleon center-of-mass energy = 2.76 TeV", *Phys. Rev. C* **84** (2011) 024906, doi:10.1103/PhysRevC.84.024906.
- [54] Z.-W. Lin et al., "A Multi-phase transport model for relativistic heavy ion collisions", *Phys. Rev. C* **72** (2005) 064901, doi:10.1103/PhysRevC.72.064901.
- [55] CMS Collaboration, "Track reconstruction in the CMS tracker", CMS Note NOTE-2006-041, (2006).
- [56] CMS Collaboration, "CMS tracking performance results from early LHC operation", *Eur. Phys. J. C* **70** (2010) 1165, doi:10.1140/epjc/s10052-010-1491-3.

- [57] I. P. Lokhtin and A. M. Snigirev, "A model of jet quenching in ultrarelativistic heavy ion collisions and high- p_T hadron spectra at RHIC", *Eur. Phys. J. C* **45** (2006) 211, doi:10.1140/epjc/s2005-02426-3.
- [58] C. Tsallis, "Possible generalization of Boltzmann-Gibbs statistics", *J. Stat. Phys.* **52** (1988) 479, doi:10.1007/BF01016429.
- [59] G. Wilk and Z. Włodarczyk, "Power laws in elementary and heavy-ion collisions: A Story of fluctuations and nonextensivity?", *Eur. Phys. J. A* **40** (2009) 299, doi:10.1140/epja/i2009-10803-9.
- [60] T. S. Biró, G. Purcsel, and K. Ürmössy, "Non-Extensive Approach to Quark Matter", *Eur. Phys. J. A* **40** (2009) 325, doi:10.1140/epja/i2009-10806-6, arXiv:0812.2104.
- [61] H. Holopainen, H. Niemi, and K. J. Eskola, "Event-by-event hydrodynamics and elliptic flow from fluctuating initial state", *Phys. Rev. C* **83** (2011) 034901, doi:10.1103/PhysRevC.83.034901.
- [62] H. Petersen et al., "Triangular flow in event-by-event ideal hydrodynamics in Au + Au collisions at $\sqrt{s_{NN}} = 200A$ GeV", *Phys. Rev. C* **82** (2010) 041901, doi:10.1103/PhysRevC.82.041901.
- [63] F. G. Gardim et al., "Mapping the hydrodynamic response to the initial geometry in heavy-ion collisions", *Phys. Rev. C* **85** (2012) 024908, doi:10.1103/PhysRevC.85.024908.
- [64] E877 Collaboration, "Proton and pion production relative to the reaction plane in Au + Au collisions at 11 AGeV/c", *Phys. Rev. C* **56** (1997) 3254, doi:10.1103/PhysRevC.56.3254.
- [65] M. Luzum and P. Romatschke, "Conformal Relativistic Viscous Hydrodynamics: Applications to RHIC results at $\sqrt{s_{NN}} = 200$ GeV", *Phys. Rev. C* **78** (2008) 034915, doi:10.1103/PhysRevC.78.034915.
- [66] CMS Collaboration, "Study of high- p_T charged particle suppression in PbPb compared to pp collisions at $\sqrt{s_{NN}} = 2.76$ TeV", *Eur. Phys. J. C* **72** (2012) 1945, doi:10.1140/epjc/s10052-012-1945-x.
- [67] STAR Collaboration, "Centrality dependence of charged hadron and strange hadron elliptic flow from $\sqrt{s_{NN}} = 200$ GeV Au+Au collisions", *Phys. Rev. C* **77** (2008) 054901, doi:10.1103/PhysRevC.77.054901.
- [68] T. Hirano, P. Huovinen, and Y. Nara, "Elliptic flow in U+U collisions at $\sqrt{s_{NN}} = 200$ GeV and in Pb+Pb collisions at $\sqrt{s_{NN}} = 2.76$ TeV: Prediction from a hybrid approach", *Phys. Rev. C* **83** (2011) 021902, doi:10.1103/PhysRevC.83.021902.
- [69] H. Song et al., "200 A GeV Au+Au collisions serve a nearly perfect quark-gluon liquid", *Phys. Rev. Lett.* **106** (2011) 192301, doi:10.1103/PhysRevLett.106.192301.
- [70] J. L. Nagle, I. G. Bearden, and W. A. Zajc, "Quark-Gluon Plasma at RHIC and the LHC: Perfect Fluid too Perfect?", *New J. Phys.* **13** (2011) 075004, doi:10.1088/1367-2630/13/7/075004.

- [71] C. Shen et al., “Radial and elliptic flow in Pb+Pb collisions at the Large Hadron Collider from viscous hydrodynamics”, *Phys. Rev. C* **84** (2011) 044903, doi:10.1103/PhysRevC.84.044903.
- [72] H.-J. Drescher and Y. Nara, “Eccentricity fluctuations from the color glass condensate in ultrarelativistic heavy ion collisions”, *Phys. Rev. C* **76** (2007) 041903, doi:10.1103/PhysRevC.76.041903.
- [73] PHENIX Collaboration, “Systematic Studies of Elliptic Flow Measurements in Au+Au Collisions at $\sqrt{s_{NN}} = 200$ GeV”, *Phys. Rev. C* **80** (2009) 024909, doi:10.1103/PhysRevC.80.024909.
- [74] STAR Collaboration, “Azimuthal anisotropy and correlations at large transverse momenta in p+p and Au+Au collisions at $\sqrt{s_{NN}} = 200$ GeV”, *Phys. Rev. Lett.* **93** (2004) 252301, doi:10.1103/PhysRevLett.93.252301.
- [75] CMS Collaboration, “Dependence on pseudorapidity and centrality of charged hadron production in PbPb collisions at a nucleon-nucleon centre-of-mass energy of 2.76 TeV”, *JHEP* **08** (2011) 141, doi:10.1007/JHEP08(2011)141.
- [76] STAR Collaboration, “Identified particle production, azimuthal anisotropy, and interferometry measurements in Au+Au collisions at $\sqrt{s_{NN}} = 9.2$ GeV”, *Phys. Rev. C* **81** (2010) 024911, doi:10.1103/PhysRevC.81.024911.
- [77] PHOBOS Collaboration, “Centrality and pseudorapidity dependence of elliptic flow for charged hadrons in Au+Au collisions at $\sqrt{s_{NN}} = 200$ GeV”, *Phys. Rev. C* **72** (2005) 051901, doi:10.1103/PhysRevC.72.051901.
- [78] PHOBOS Collaboration, “Pseudorapidity and Centrality Dependence of the Collective Flow of Charged Particles in Au+Au Collisions at $\sqrt{s_{NN}} = 130$ GeV”, *Phys. Rev. Lett.* **89** (2002) 222301, doi:10.1103/PhysRevLett.89.222301.
- [79] PHOBOS Collaboration, “Directed and elliptic flow of charged pions and protons in Pb+Pb collisions at 40A and 158A GeV”, *Phys. Rev. C* **68** (2003) 034903, doi:10.1103/PhysRevC.68.034903.
- [80] E877 Collaboration, “Energy and charged particle flow in 10.8A GeV/c Au+Au collisions”, *Phys. Rev. C* **55** (1997) 1420, doi:10.1103/PhysRevC.55.1420.
- [81] CERES Collaboration, “New results from CERES”, *Nucl. Phys. A* **698** (2002) 253, doi:10.1016/S0375-9474(01)01371-9.
- [82] STAR Collaboration, “Measurements of transverse energy distributions in Au + Au collisions at $\sqrt{s_{NN}} = 200$ GeV”, *Phys. Rev. C* **70** (2004) 054907, doi:10.1103/PhysRevC.70.054907.
- [83] M. Luzum and P. Romatschke, “Viscous Hydrodynamic Predictions for Nuclear Collisions at the LHC”, *Phys. Rev. Lett.* **103** (2009) 262302, doi:10.1103/PhysRevLett.103.262302.
- [84] C. Shen and U. Heinz, “Hydrodynamic flow in heavy-ion collisions with large hadronic viscosity”, *Phys. Rev. C* **83** (2011) 044909, doi:10.1103/PhysRevC.83.044909.

- [85] STAR Collaboration, "Elliptic flow from two and four particle correlations in Au+Au collisions at $\sqrt{s_{NN}} = 130$ GeV", *Phys. Rev. C* **66** (2002) 034904, doi:10.1103/PhysRevC.66.034904.
- [86] ALICE Collaboration, "Centrality dependence of the charged-particle multiplicity density at mid-rapidity in Pb-Pb collisions at $\sqrt{s_{NN}} = 2.76$ TeV", *Phys. Rev. Lett.* **106** (2011) 032301, doi:10.1103/PhysRevLett.106.032301.
- [87] R. Andrade et al., "On the necessity to include event-by-event fluctuations in experimental evaluation of elliptical flow", *Phys. Rev. Lett.* **97** (2006) 202302, doi:10.1103/PhysRevLett.97.202302.
- [88] J. Benecke et al., "Hypothesis of Limiting Fragmentation in High-Energy Collisions", *Phys. Rev.* **188** (1969) 2159, doi:10.1103/PhysRev.188.2159.
- [89] N. Borghini and U. A. Wiedemann, "Predictions for the LHC heavy ion programme", *J. Phys. G* **35** (2008) 023001, doi:10.1088/0954-3899/35/2/023001.

A The CMS Collaboration

Yerevan Physics Institute, Yerevan, Armenia

S. Chatrchyan, V. Khachatryan, A.M. Sirunyan, A. Tumasyan

Institut für Hochenergiephysik der OeAW, Wien, Austria

W. Adam, T. Bergauer, M. Dragicevic, J. Erö, C. Fabjan, M. Friedl, R. Frühwirth, V.M. Ghete, J. Hammer¹, N. Hörmann, J. Hrubec, M. Jeitler, W. Kiesenhofer, M. Krammer, D. Liko, I. Mikulec, M. Pernicka[†], B. Rahbaran, C. Rohringer, H. Rohringer, R. Schöffbeck, J. Strauss, A. Taurok, F. Teischinger, P. Wagner, W. Waltenberger, G. Walzel, E. Widl, C.-E. Wulz

National Centre for Particle and High Energy Physics, Minsk, Belarus

V. Mossolov, N. Shumeiko, J. Suarez Gonzalez

Universiteit Antwerpen, Antwerpen, Belgium

S. Bansal, K. Cerny, T. Cornelis, E.A. De Wolf, X. Janssen, S. Luyckx, T. Maes, L. Mucibello, S. Ochesanu, B. Roland, R. Rougny, M. Selvaggi, H. Van Haevermaet, P. Van Mechelen, N. Van Remortel, A. Van Spilbeeck

Vrije Universiteit Brussel, Brussel, Belgium

F. Blekman, S. Blyweert, J. D'Hondt, R. Gonzalez Suarez, A. Kalogeropoulos, M. Maes, A. Olbrechts, W. Van Doninck, P. Van Mulders, G.P. Van Onsem, I. Villella

Université Libre de Bruxelles, Bruxelles, Belgium

O. Charaf, B. Clerbaux, G. De Lentdecker, V. Dero, A.P.R. Gay, T. Hreus, A. Léonard, P.E. Marage, T. Reis, L. Thomas, C. Vander Velde, P. Vanlaer

Ghent University, Ghent, Belgium

V. Adler, K. Bernaert, A. Cimmino, S. Costantini, G. Garcia, M. Grunewald, B. Klein, J. Lellouch, A. Marinov, J. McCartin, A.A. Ocampo Rios, D. Ryckbosch, N. Strobbe, F. Thyssen, M. Tytgat, L. Vanelderen, P. Verwilligen, S. Walsh, E. Yazgan, N. Zaganidis

Université Catholique de Louvain, Louvain-la-Neuve, Belgium

S. Basesmez, G. Bruno, L. Ceard, C. Delaere, T. du Pree, D. Favart, L. Forthomme, A. Giammanco², J. Hollar, V. Lemaitre, J. Liao, O. Militaru, C. Nuttens, D. Pagano, A. Pin, K. Piotrkowski, N. Schul

Université de Mons, Mons, Belgium

N. Belyi, T. Caebergs, E. Daubie, G.H. Hammad

Centro Brasileiro de Pesquisas Fisicas, Rio de Janeiro, Brazil

G.A. Alves, M. Correa Martins Junior, D. De Jesus Damiao, T. Martins, M.E. Pol, M.H.G. Souza

Universidade do Estado do Rio de Janeiro, Rio de Janeiro, Brazil

W.L. Aldá Júnior, W. Carvalho, A. Custódio, E.M. Da Costa, C. De Oliveira Martins, S. Fonseca De Souza, D. Matos Figueiredo, L. Mundim, H. Nogima, V. Oguri, W.L. Prado Da Silva, A. Santoro, S.M. Silva Do Amaral, L. Soares Jorge, A. Sznajder

Instituto de Fisica Teorica, Universidade Estadual Paulista, Sao Paulo, Brazil

T.S. Anjos³, C.A. Bernardes³, F.A. Dias⁴, T.R. Fernandez Perez Tomei, E. M. Gregores³, C. Lagana, F. Marinho, P.G. Mercadante³, S.F. Novaes, Sandra S. Padula

Institute for Nuclear Research and Nuclear Energy, Sofia, Bulgaria

V. Genchev¹, P. Iaydjiev¹, S. Piperov, M. Rodozov, S. Stoykova, G. Sultanov, V. Tcholakov, R. Trayanov, M. Vutova

University of Sofia, Sofia, Bulgaria

A. Dimitrov, R. Hadjiiska, V. Kozhuharov, L. Litov, B. Pavlov, P. Petkov

Institute of High Energy Physics, Beijing, China

J.G. Bian, G.M. Chen, H.S. Chen, C.H. Jiang, D. Liang, S. Liang, X. Meng, J. Tao, J. Wang, J. Wang, X. Wang, Z. Wang, H. Xiao, M. Xu, J. Zang, Z. Zhang

State Key Lab. of Nucl. Phys. and Tech., Peking University, Beijing, China

C. Asawatangtrakuldee, Y. Ban, S. Guo, Y. Guo, W. Li, S. Liu, Y. Mao, S.J. Qian, H. Teng, S. Wang, B. Zhu, W. Zou

Universidad de Los Andes, Bogota, Colombia

C. Avila, B. Gomez Moreno, A.F. Osorio Oliveros, J.C. Sanabria

Technical University of Split, Split, Croatia

N. Godinovic, D. Lelas, R. Plestina⁵, D. Polic, I. Puljak¹

University of Split, Split, Croatia

Z. Antunovic, M. Dzelalija, M. Kovac

Institute Rudjer Boskovic, Zagreb, Croatia

V. Brigljevic, S. Duric, K. Kadija, J. Luetic, S. Morovic

University of Cyprus, Nicosia, Cyprus

A. Attikis, M. Galanti, G. Mavromanolakis, J. Mousa, C. Nicolaou, F. Ptochos, P.A. Razis

Charles University, Prague, Czech Republic

M. Finger, M. Finger Jr.

Academy of Scientific Research and Technology of the Arab Republic of Egypt, Egyptian Network of High Energy Physics, Cairo, Egypt

Y. Assran⁶, S. Elgammal, A. Ellithi Kamel⁷, S. Khalil⁸, M.A. Mahmoud⁹, A. Radi^{8,10}

National Institute of Chemical Physics and Biophysics, Tallinn, Estonia

M. Kadastik, M. Müntel, M. Raidal, L. Rebane, A. Tiko

Department of Physics, University of Helsinki, Helsinki, Finland

V. Azzolini, P. Eerola, G. Fedi, M. Voutilainen

Helsinki Institute of Physics, Helsinki, Finland

J. Härkönen, A. Heikkinen, V. Karimäki, R. Kinnunen, M.J. Kortelainen, T. Lampén, K. Lassila-Perini, S. Lehti, T. Lindén, P. Luukka, T. Mäenpää, T. Peltola, E. Tuominen, J. Tuominiemi, E. Tuovinen, D. Ungaro, L. Wendland

Lappeenranta University of Technology, Lappeenranta, Finland

K. Banzuzi, A. Korpela, T. Tuuva

DSM/IRFU, CEA/Saclay, Gif-sur-Yvette, France

M. Besancon, S. Choudhury, M. Dejardin, D. Denegri, B. Fabbro, J.L. Faure, F. Ferri, S. Ganjour, A. Givernaud, P. Gras, G. Hamel de Monchenault, P. Jarry, E. Locci, J. Malcles, L. Millischer, A. Nayak, J. Rander, A. Rosowsky, I. Shreyber, M. Titov

Laboratoire Leprince-Ringuet, Ecole Polytechnique, IN2P3-CNRS, Palaiseau, France

S. Baffioni, F. Beaudette, L. Benhabib, L. Bianchini, M. Bluj¹¹, C. Broutin, P. Busson, C. Charlot, N. Daci, T. Dahms, L. Dobrzynski, R. Granier de Cassagnac, M. Haguener, P. Miné, C. Mironov, C. Ochando, P. Paganini, D. Sabes, R. Salerno, Y. Sirois, C. Veelken, A. Zabi

Institut Pluridisciplinaire Hubert Curien, Université de Strasbourg, Université de Haute Alsace Mulhouse, CNRS/IN2P3, Strasbourg, France

J.-L. Agram¹², J. Andrea, D. Bloch, D. Bodin, J.-M. Brom, M. Cardaci, E.C. Chabert, C. Collard, E. Conte¹², F. Drouhin¹², C. Ferro, J.-C. Fontaine¹², D. Gelé, U. Goerlach, P. Juillot, M. Karim¹², A.-C. Le Bihan, P. Van Hove

Centre de Calcul de l'Institut National de Physique Nucleaire et de Physique des Particules (IN2P3), Villeurbanne, France

F. Fassi, D. Mercier

Université de Lyon, Université Claude Bernard Lyon 1, CNRS-IN2P3, Institut de Physique Nucléaire de Lyon, Villeurbanne, France

S. Beauceron, N. Beaupere, O. Bondu, G. Boudoul, H. Brun, J. Chasserat, R. Chierici¹, D. Contardo, P. Depasse, H. El Mamouni, J. Fay, S. Gascon, M. Gouzevitch, B. Ille, T. Kurca, M. Lethuillier, L. Mirabito, S. Perries, V. Sordini, S. Tosi, Y. Tschudi, P. Verdier, S. Viret

Institute of High Energy Physics and Informatization, Tbilisi State University, Tbilisi, Georgia

Z. Tsamalaidze¹³

RWTH Aachen University, I. Physikalisches Institut, Aachen, Germany

G. Anagnostou, S. Beranek, M. Edelhoff, L. Feld, N. Heracleous, O. Hindrichs, R. Jussen, K. Klein, J. Merz, A. Ostapchuk, A. Perieanu, F. Raupach, J. Sammet, S. Schael, D. Sprenger, H. Weber, B. Wittmer, V. Zhukov¹⁴

RWTH Aachen University, III. Physikalisches Institut A, Aachen, Germany

M. Ata, J. Caudron, E. Dietz-Laursonn, D. Duchardt, M. Erdmann, A. Güth, T. Hebbeker, C. Heidemann, K. Hoepfner, T. Klimkovich, D. Klingebiel, P. Kreuzer, D. Lanske[†], J. Lingemann, C. Magass, M. Merschmeyer, A. Meyer, M. Olschewski, P. Papacz, H. Pieta, H. Reithler, S.A. Schmitz, L. Sonnenschein, J. Steggemann, D. Teyssier, M. Weber

RWTH Aachen University, III. Physikalisches Institut B, Aachen, Germany

M. Bontenackels, V. Cherepanov, M. Davids, G. Flügge, H. Geenen, M. Geisler, W. Haj Ahmad, F. Hoehle, B. Kargoll, T. Kress, Y. Kuessel, A. Linn, A. Nowack, L. Perchalla, O. Pooth, J. Rennefeld, P. Sauerland, A. Stahl

Deutsches Elektronen-Synchrotron, Hamburg, Germany

M. Aldaya Martin, J. Behr, W. Behrenhoff, U. Behrens, M. Bergholz¹⁵, A. Bethani, K. Borras, A. Burgmeier, A. Cakir, L. Calligaris, A. Campbell, E. Castro, F. Costanza, D. Dammann, G. Eckerlin, D. Eckstein, D. Fischer, G. Flucke, A. Geiser, I. Glushkov, S. Habib, J. Hauk, H. Jung¹, M. Kasemann, P. Katsas, C. Kleinwort, H. Kluge, A. Knutsson, M. Krämer, D. Krücker, E. Kuznetsova, W. Lange, W. Lohmann¹⁵, B. Lutz, R. Mankel, I. Marfin, M. Marienfeld, I.-A. Melzer-Pellmann, A.B. Meyer, J. Mnich, A. Mussgiller, S. Naumann-Emme, J. Olzem, H. Perrey, A. Petrukhin, D. Pitzl, A. Raspereza, P.M. Ribeiro Cipriano, C. Riedl, M. Rosin, J. Salfeld-Nebgen, R. Schmidt¹⁵, T. Schoerner-Sadenius, N. Sen, A. Spiridonov, M. Stein, R. Walsh, C. Wissing

University of Hamburg, Hamburg, Germany

C. Autermann, V. Blobel, S. Bobrovskiy, J. Draeger, H. Enderle, J. Erfle, U. Gebbert, M. Görner, T. Hermanns, R.S. Höing, K. Kaschube, G. Kaussen, H. Kirschenmann, R. Klanner, J. Lange, B. Mura, F. Nowak, N. Pietsch, D. Rathjens, C. Sander, H. Schettler, P. Schleper, E. Schlieckau, A. Schmidt, M. Schröder, T. Schum, M. Seidel, H. Stadie, G. Steinbrück, J. Thomsen

Institut für Experimentelle Kernphysik, Karlsruhe, Germany

C. Barth, J. Berger, T. Chwalek, W. De Boer, A. Dierlamm, M. Feindt, M. Guthoff¹, C. Hackstein, F. Hartmann, M. Heinrich, H. Held, K.H. Hoffmann, S. Honc, U. Husemann, I. Katkov¹⁴, J.R. Komaragiri, D. Martschei, S. Mueller, Th. Müller, M. Niegel, A. Nürnberg, O. Oberst, A. Oehler, J. Ott, T. Peiffer, G. Quast, K. Rabbertz, F. Ratnikov, N. Ratnikova, S. Röcker, C. Saout, A. Scheurer, F.-P. Schilling, M. Schmanau, G. Schott, H.J. Simonis, F.M. Stober, D. Troendle, R. Ulrich, J. Wagner-Kuhr, T. Weiler, M. Zeise, E.B. Ziebarth

Institute of Nuclear Physics "Demokritos", Aghia Paraskevi, Greece

G. Daskalakis, T. Gerasis, S. Kesisoglou, A. Kyriakis, D. Loukas, I. Manolakos, A. Markou, C. Markou, C. Mavrommatis, E. Ntomari

University of Athens, Athens, Greece

L. Gouskos, T.J. Mertzimekis, A. Panagiotou, N. Saoulidou

University of Ioánnina, Ioánnina, Greece

I. Evangelou, C. Foudas¹, P. Kokkas, N. Manthos, I. Papadopoulos, V. Patras

KFKI Research Institute for Particle and Nuclear Physics, Budapest, Hungary

G. Bencze, C. Hajdu¹, P. Hidas, D. Horvath¹⁶, K. Krajczar¹⁷, B. Radics, F. Sikler¹, V. Veszpremi, G. Vesztergombi¹⁷

Institute of Nuclear Research ATOMKI, Debrecen, Hungary

N. Beni, S. Czellar, J. Molnar, J. Palinkas, Z. Szillasi

University of Debrecen, Debrecen, Hungary

J. Karancsi, P. Raics, Z.L. Trocsanyi, B. Ujvari

Panjab University, Chandigarh, India

S.B. Beri, V. Bhatnagar, N. Dhingra, R. Gupta, M. Jindal, M. Kaur, J.M. Kohli, M.Z. Mehta, N. Nishu, L.K. Saini, A. Sharma, J. Singh, S.P. Singh

University of Delhi, Delhi, India

S. Ahuja, B.C. Choudhary, A. Kumar, A. Kumar, S. Malhotra, M. Naimuddin, K. Ranjan, V. Sharma, R.K. Shivpuri

Saha Institute of Nuclear Physics, Kolkata, India

S. Banerjee, S. Bhattacharya, S. Dutta, B. Gomber, Sa. Jain, Sh. Jain, R. Khurana, S. Sarkar

Bhabha Atomic Research Centre, Mumbai, India

A. Abdulsalam, R.K. Choudhury, D. Dutta, S. Kailas, V. Kumar, A.K. Mohanty¹, L.M. Pant, P. Shukla

Tata Institute of Fundamental Research - EHEP, Mumbai, India

T. Aziz, S. Ganguly, M. Guchait¹⁸, A. Gurtu¹⁹, M. Maity²⁰, G. Majumder, K. Mazumdar, G.B. Mohanty, B. Parida, K. Sudhakar, N. Wickramage

Tata Institute of Fundamental Research - HECR, Mumbai, India

S. Banerjee, S. Dugad

Institute for Research in Fundamental Sciences (IPM), Tehran, Iran

H. Arfaei, H. Bakhshiansohi²¹, S.M. Etesami²², A. Fahim²¹, M. Hashemi, H. Hesari, A. Jafari²¹, M. Khakzad, A. Mohammadi²³, M. Mohammadi Najafabadi, S. Paktinat Mehdiabadi, B. Safarzadeh²⁴, M. Zeinali²²

INFN Sezione di Bari ^a, Università di Bari ^b, Politecnico di Bari ^c, Bari, Italy

M. Abbrescia^{a,b}, L. Barbone^{a,b}, C. Calabria^{a,b,1}, S.S. Chhibra^{a,b}, A. Colaleo^a, D. Creanza^{a,c}, N. De Filippis^{a,c,1}, M. De Palma^{a,b}, L. Fiore^a, G. Iaselli^{a,c}, L. Lusito^{a,b}, G. Maggi^{a,c}, M. Maggi^a, B. Marangelli^{a,b}, S. My^{a,c}, S. Nuzzo^{a,b}, N. Pacifico^{a,b}, A. Pompili^{a,b}, G. Pugliese^{a,c}, G. Selvaggi^{a,b}, L. Silvestris^a, G. Singh^{a,b}, G. Zito^a

INFN Sezione di Bologna ^a, Università di Bologna ^b, Bologna, Italy

G. Abbiendi^a, A.C. Benvenuti^a, D. Bonacorsi^{a,b}, S. Braibant-Giacomelli^{a,b}, L. Brigliadori^{a,b}, P. Capiluppi^{a,b}, A. Castro^{a,b}, F.R. Cavallo^a, M. Cuffiani^{a,b}, G.M. Dallavalle^a, F. Fabbri^a, A. Fanfani^{a,b}, D. Fasanella^{a,b,1}, P. Giacomelli^a, C. Grandi^a, L. Guiducci, S. Marcellini^a, G. Masetti^a, M. Meneghelli^{a,b,1}, A. Montanari^a, F.L. Navarria^{a,b}, F. Odorici^a, A. Perrotta^a, F. Primavera^{a,b}, A.M. Rossi^{a,b}, T. Rovelli^{a,b}, G. Siroli^{a,b}, R. Travaglini^{a,b}

INFN Sezione di Catania ^a, Università di Catania ^b, Catania, Italy

S. Albergo^{a,b}, G. Cappello^{a,b}, M. Chiorboli^{a,b}, S. Costa^{a,b}, R. Potenza^{a,b}, A. Tricomi^{a,b}, C. Tuve^{a,b}

INFN Sezione di Firenze ^a, Università di Firenze ^b, Firenze, Italy

G. Barbagli^a, V. Ciulli^{a,b}, C. Civinini^a, R. D'Alessandro^{a,b}, E. Focardi^{a,b}, S. Frosali^{a,b}, E. Gallo^a, S. Gonzi^{a,b}, M. Meschini^a, S. Paoletti^a, G. Sguazzoni^a, A. Tropiano^{a,1}

INFN Laboratori Nazionali di Frascati, Frascati, Italy

L. Benussi, S. Bianco, S. Colafranceschi²⁵, F. Fabbri, D. Piccolo

INFN Sezione di Genova, Genova, Italy

P. Fabbriatore, R. Musenich

INFN Sezione di Milano-Bicocca ^a, Università di Milano-Bicocca ^b, Milano, Italy

A. Benaglia^{a,b,1}, F. De Guio^{a,b}, L. Di Matteo^{a,b,1}, S. Fiorendi^{a,b}, S. Gennai^{a,1}, A. Ghezzi^{a,b}, S. Malvezzi^a, R.A. Manzoni^{a,b}, A. Martelli^{a,b}, A. Massironi^{a,b,1}, D. Menasce^a, L. Moroni^a, M. Paganoni^{a,b}, D. Pedrini^a, S. Ragazzi^{a,b}, N. Redaelli^a, S. Sala^a, T. Tabarelli de Fatis^{a,b}

INFN Sezione di Napoli ^a, Università di Napoli "Federico II" ^b, Napoli, Italy

S. Buontempo^a, C.A. Carrillo Montoya^{a,1}, N. Cavallo^{a,26}, A. De Cosa^{a,b}, O. Dogangun^{a,b}, F. Fabozzi^{a,26}, A.O.M. Iorio^{a,1}, L. Lista^a, S. Meola^{a,27}, M. Merola^{a,b}, P. Paolucci^a

INFN Sezione di Padova ^a, Università di Padova ^b, Università di Trento (Trento) ^c, Padova, Italy

P. Azzi^a, N. Bacchetta^{a,1}, P. Bellan^{a,b}, M. Biasotto^{a,28}, D. Bisello^{a,b}, A. Branca^{a,1}, P. Checchia^a, T. Dorigo^a, U. Dosselli^a, F. Gasparini^{a,b}, A. Gozzelino^a, M. Gulmini^{a,28}, K. Kanishchev^{a,c}, S. Lacaprara^a, I. Lazzizzera^{a,c}, M. Margoni^{a,b}, G. Maron^{a,28}, A.T. Meneguzzo^{a,b}, L. Perrozzi^a, N. Pozzobon^{a,b}, P. Ronchese^{a,b}, F. Simonetto^{a,b}, E. Torassa^a, M. Tosi^{a,b,1}, S. Vanini^{a,b}

INFN Sezione di Pavia ^a, Università di Pavia ^b, Pavia, Italy

M. Gabusi^{a,b}, S.P. Ratti^{a,b}, C. Riccardi^{a,b}, P. Torre^{a,b}, P. Vitulo^{a,b}

INFN Sezione di Perugia ^a, Università di Perugia ^b, Perugia, Italy

G.M. Bilei^a, L. Fano^{a,b}, P. Lariccia^{a,b}, A. Lucaroni^{a,b,1}, G. Mantovani^{a,b}, M. Menichelli^a, A. Nappi^{a,b}, F. Romeo^{a,b}, A. Saha, A. Santocchia^{a,b}, S. Taroni^{a,b,1}

INFN Sezione di Pisa ^a, Università di Pisa ^b, Scuola Normale Superiore di Pisa ^c, Pisa, Italy

P. Azzurri^{a,c}, G. Bagliesi^a, T. Boccali^a, G. Broccolo^{a,c}, R. Castaldi^a, R.T. D'Agnolo^{a,c}, R. Dell'Orso^a, F. Fiori^{a,b,1}, L. Foà^{a,c}, A. Giassi^a, A. Kraan^a, F. Ligabue^{a,c}, T. Lomtadze^a, L. Martini^{a,29}, A. Messineo^{a,b}, F. Palla^a, F. Palmonari^a, A. Rizzi^{a,b}, A.T. Serban^{a,30}, P. Spagnolo^a, P. Squillacioti¹, R. Tenchini^a, G. Tonelli^{a,b,1}, A. Venturi^{a,1}, P.G. Verdini^a

INFN Sezione di Roma ^a, Università di Roma "La Sapienza" ^b, Roma, Italy

L. Barone^{a,b}, F. Cavallari^a, D. Del Re^{a,b,1}, M. Diemoz^a, C. Fanelli^{a,b}, M. Grassi^{a,1}, E. Longo^{a,b}, P. Meridiani^{a,1}, F. Micheli^{a,b}, S. Nourbakhsh^a, G. Organtini^{a,b}, F. Pandolfi^{a,b}, R. Paramatti^a, S. Rahatlou^{a,b}, M. Sigamani^a, L. Soffi^{a,b}

INFN Sezione di Torino ^a, Università di Torino ^b, Università del Piemonte Orientale (Novara) ^c, Torino, Italy

N. Amapane^{a,b}, R. Arcidiacono^{a,c}, S. Argiro^{a,b}, M. Arneodo^{a,c}, C. Biino^a, C. Botta^{a,b}, N. Cartiglia^a, R. Castello^{a,b}, M. Costa^{a,b}, N. Demaria^a, A. Graziano^{a,b}, C. Mariotti^{a,1}, S. Maselli^a, E. Migliore^{a,b}, V. Monaco^{a,b}, M. Musich^{a,1}, M.M. Obertino^{a,c}, N. Pastrone^a, M. Pelliccioni^a, A. Potenza^{a,b}, A. Romero^{a,b}, M. Ruspai^{a,c}, R. Sacchi^{a,b}, V. Sola^{a,b}, A. Solano^{a,b}, A. Staiano^a, A. Vilela Pereira^a

INFN Sezione di Trieste ^a, Università di Trieste ^b, Trieste, Italy

S. Belforte^a, F. Cossutti^a, G. Della Ricca^{a,b}, B. Gobbo^a, M. Marone^{a,b,1}, D. Montanino^{a,b,1}, A. Penzo^a, A. Schizzi^{a,b}

Kangwon National University, Chunchon, Korea

S.G. Heo, T.Y. Kim, S.K. Nam

Kyungpook National University, Daegu, Korea

S. Chang, J. Chung, D.H. Kim, G.N. Kim, D.J. Kong, H. Park, S.R. Ro, D.C. Son, T. Son

Chonnam National University, Institute for Universe and Elementary Particles, Kwangju, Korea

J.Y. Kim, Zero J. Kim, S. Song

Konkuk University, Seoul, Korea

H.Y. Jo

Korea University, Seoul, Korea

S. Choi, D. Gyun, B. Hong, M. Jo, H. Kim, T.J. Kim, K.S. Lee, D.H. Moon, S.K. Park, E. Seo

University of Seoul, Seoul, Korea

M. Choi, S. Kang, H. Kim, J.H. Kim, C. Park, I.C. Park, S. Park, G. Ryu

Sungkyunkwan University, Suwon, Korea

Y. Cho, Y. Choi, Y.K. Choi, J. Goh, M.S. Kim, E. Kwon, B. Lee, J. Lee, S. Lee, H. Seo, I. Yu

Vilnius University, Vilnius, Lithuania

M.J. Bilinskas, I. Grigelionis, M. Janulis, A. Juodagalvis

Centro de Investigacion y de Estudios Avanzados del IPN, Mexico City, Mexico

H. Castilla-Valdez, E. De La Cruz-Burelo, I. Heredia-de La Cruz, R. Lopez-Fernandez, R. Magaña Villalba, J. Martínez-Ortega, A. Sánchez-Hernández, L.M. Villasenor-Cendejas

Universidad Iberoamericana, Mexico City, Mexico

S. Carrillo Moreno, F. Vazquez Valencia

Benemerita Universidad Autonoma de Puebla, Puebla, Mexico

H.A. Salazar Ibarguen

Universidad Autónoma de San Luis Potosí, San Luis Potosí, Mexico

E. Casimiro Linares, A. Morelos Pineda, M.A. Reyes-Santos

University of Auckland, Auckland, New Zealand

D. Krofcheck

University of Canterbury, Christchurch, New Zealand

A.J. Bell, P.H. Butler, R. Doesburg, S. Reucroft, H. Silverwood

National Centre for Physics, Quaid-I-Azam University, Islamabad, Pakistan

M. Ahmad, M.I. Asghar, H.R. Hoorani, S. Khalid, W.A. Khan, T. Khurshid, S. Qazi, M.A. Shah, M. Shoaib

Institute of Experimental Physics, Faculty of Physics, University of Warsaw, Warsaw, Poland

G. Brona, K. Bunkowski, M. Cwiok, W. Dominik, K. Doroba, A. Kalinowski, M. Konecki, J. Krolikowski

Soltan Institute for Nuclear Studies, Warsaw, Poland

H. Bialkowska, B. Boimska, T. Frueboes, R. Gokieli, M. Górski, M. Kazana, K. Nawrocki, K. Romanowska-Rybinska, M. Szleper, G. Wrochna, P. Zalewski

Laboratório de Instrumentação e Física Experimental de Partículas, Lisboa, Portugal

N. Almeida, P. Bargassa, A. David, P. Faccioli, P.G. Ferreira Parracho, M. Gallinaro, P. Musella, J. Seixas, J. Varela, P. Vischia

Joint Institute for Nuclear Research, Dubna, Russia

S. Afanasiev, I. Belotelov, P. Bunin, M. Gavrilenko, I. Golutvin, A. Kamenev, V. Karjavin, G. Kozlov, A. Lanev, A. Malakhov, P. Moisenz, V. Palichik, V. Perelygin, S. Shmatov, V. Smirnov, A. Volodko, A. Zarubin

Petersburg Nuclear Physics Institute, Gatchina (St Petersburg), Russia

S. Evstyukhin, V. Golovtsov, Y. Ivanov, V. Kim, P. Levchenko, V. Murzin, V. Oreshkin, I. Smirnov, V. Sulimov, L. Uvarov, S. Vavilov, A. Vorobyev, An. Vorobyev

Institute for Nuclear Research, Moscow, Russia

Yu. Andreev, A. Dermenev, S. Gninenko, N. Golubev, M. Kirsanov, N. Krasnikov, V. Matveev, A. Pashenkov, D. Tlisov, A. Toropin

Institute for Theoretical and Experimental Physics, Moscow, Russia

V. Epshteyn, M. Erofeeva, V. Gavrilov, M. Kossov¹, N. Lychkovskaya, V. Popov, G. Safronov, S. Semenov, V. Stolin, E. Vlasov, A. Zhokin

Moscow State University, Moscow, Russia

A. Belyaev, E. Boos, A. Ershov, A. Gribushin, V. Klyukhin, O. Kodolova, V. Korotkikh, I. Lokhtin, A. Markina, S. Obraztsov, M. Perfilov, S. Petrushanko, L. Sarycheva[†], V. Savrin, A. Snigirev, I. Vardanyan

P.N. Lebedev Physical Institute, Moscow, Russia

V. Andreev, M. Azarkin, I. Dremin, M. Kirakosyan, A. Leonidov, G. Mesyats, S.V. Rusakov, A. Vinogradov

State Research Center of Russian Federation, Institute for High Energy Physics, Protvino, Russia

I. Azhgirey, I. Bayshev, S. Bitioukov, V. Grishin¹, V. Kachanov, D. Konstantinov, A. Korablev, V. Krychkin, V. Petrov, R. Ryutin, A. Sobol, L. Tourtchanovitch, S. Troshin, N. Tyurin, A. Uzunian, A. Volkov

University of Belgrade, Faculty of Physics and Vinca Institute of Nuclear Sciences, Belgrade, Serbia

P. Adzic³¹, M. Djordjevic, M. Ekmedzic, D. Krpic³¹, J. Milosevic

Centro de Investigaciones Energéticas Medioambientales y Tecnológicas (CIEMAT), Madrid, Spain

M. Aguilar-Benitez, J. Alcaraz Maestre, P. Arce, C. Battilana, E. Calvo, M. Cerrada, M. Chamizo Llatas, N. Colino, B. De La Cruz, A. Delgado Peris, C. Diez Pardos, D. Domínguez Vázquez, C. Fernandez Bedoya, J.P. Fernández Ramos, A. Ferrando, J. Flix, M.C. Fouz, P. Garcia-Abia, O. Gonzalez Lopez, S. Goy Lopez, J.M. Hernandez, M.I. Josa, G. Merino, J. Puerta Pelayo, I. Redondo, L. Romero, J. Santaolalla, M.S. Soares, C. Willmott

Universidad Autónoma de Madrid, Madrid, Spain

C. Albajar, G. Codispoti, J.F. de Trocóniz

Universidad de Oviedo, Oviedo, Spain

J. Cuevas, J. Fernandez Menendez, S. Folgueras, I. Gonzalez Caballero, L. Lloret Iglesias, J. Piedra Gomez³², J.M. Vizan Garcia

Instituto de Física de Cantabria (IFCA), CSIC-Universidad de Cantabria, Santander, Spain

J.A. Brochero Cifuentes, I.J. Cabrillo, A. Calderon, S.H. Chuang, J. Duarte Campderros, M. Felcini³³, M. Fernandez, G. Gomez, J. Gonzalez Sanchez, C. Jorda, P. Lobelle Pardo, A. Lopez Virto, J. Marco, R. Marco, C. Martinez Rivero, F. Matorras, F.J. Munoz Sanchez, T. Rodrigo, A.Y. Rodríguez-Marrero, A. Ruiz-Jimeno, L. Scodellaro, M. Sobron Sanudo, I. Vila, R. Vilar Cortabitarte

CERN, European Organization for Nuclear Research, Geneva, Switzerland

D. Abbaneo, E. Auffray, G. Auzinger, P. Baillon, A.H. Ball, D. Barney, C. Bernet⁵, G. Bianchi, P. Bloch, A. Bocci, A. Bonato, H. Breuker, T. Camporesi, G. Cerminara, T. Christiansen, J.A. Coarasa Perez, D. D'Enterria, A. De Roeck, S. Di Guida, M. Dobson, N. Dupont-Sagorin, A. Elliott-Peisert, B. Frisch, W. Funk, G. Georgiou, M. Giffels, D. Gigi, K. Gill, D. Giordano, M. Giunta, F. Glege, R. Gomez-Reino Garrido, P. Govoni, S. Gowdy, R. Guida, M. Hansen, P. Harris, C. Hartl, J. Harvey, B. Hegner, A. Hinzmann, V. Innocente, P. Janot, K. Kaadze, E. Karavakis, K. Kousouris, P. Lecoq, P. Lenzi, C. Lourenço, T. Mäki, M. Malberti, L. Malgeri, M. Mannelli, L. Masetti, F. Meijers, S. Mersi, E. Meschi, R. Moser, M.U. Mozer, M. Mulders, E. Nesvold, M. Nguyen, T. Orimoto, L. Orsini, E. Palencia Cortezon, E. Perez, A. Petrilli, A. Pfeiffer, M. Pierini, M. Pimiä, D. Piparo, G. Polese, L. Quertenmont, A. Racz, W. Reece, J. Rodrigues Antunes, G. Rolandi³⁴, T. Rommerskirchen, C. Rovelli³⁵, M. Rovere, H. Sakulin, F. Santanastasio, C. Schäfer, C. Schwick, I. Segoni, S. Sekmen, A. Sharma, P. Siegrist, P. Silva, M. Simon, P. Sphicas³⁶, D. Spiga, M. Spiropulu⁴, M. Stoye, A. Tsiros, G.I. Veres¹⁷, J.R. Vlimant, H.K. Wöhri, S.D. Worm³⁷, W.D. Zeuner

Paul Scherrer Institut, Villigen, Switzerland

W. Bertl, K. Deiters, W. Erdmann, K. Gabathuler, R. Horisberger, Q. Ingram, H.C. Kaestli, S. König, D. Kotlinski, U. Langenegger, F. Meier, D. Renker, T. Rohe, J. Sibille³⁸

Institute for Particle Physics, ETH Zurich, Zurich, Switzerland

L. Bäni, P. Bortignon, M.A. Buchmann, B. Casal, N. Chanon, Z. Chen, A. Deisher, G. Dissertori, M. Dittmar, M. Dünser, J. Eugster, K. Freudenreich, C. Grab, P. Lecomte, W. Luster, A.C. Marini, P. Martinez Ruiz del Arbol, N. Mohr, F. Moortgat, C. Nägeli³⁹, P. Nef, F. Nessi-Tedaldi, L. Pape, F. Pauss, M. Peruzzi, F.J. Ronga, M. Rossini, L. Sala, A.K. Sanchez, A. Starodumov⁴⁰, B. Stieger, M. Takahashi, L. Tauscher[†], A. Thea, K. Theofilatos, D. Treille, C. Urscheler, R. Wallny, H.A. Weber, L. Wehrli

Universität Zürich, Zurich, Switzerland

E. Aguilo, C. AMSLER, V. Chiochia, S. De Visscher, C. Favaro, M. Ivova Rikova, B. Millan Mejias, P. Otiougova, P. Robmann, H. Snoek, S. Tuppusti, M. Verzetti

National Central University, Chung-Li, Taiwan

Y.H. Chang, K.H. Chen, A. Go, C.M. Kuo, S.W. Li, W. Lin, Z.K. Liu, Y.J. Lu, D. Mekterovic, A.P. Singh, R. Volpe, S.S. Yu

National Taiwan University (NTU), Taipei, Taiwan

P. Bartalini, P. Chang, Y.H. Chang, Y.W. Chang, Y. Chao, K.F. Chen, C. Dietz, U. Grundler, W.-S. Hou, Y. Hsiung, K.Y. Kao, Y.J. Lei, R.-S. Lu, D. Majumder, E. Petrakou, X. Shi, J.G. Shiu, Y.M. Tzeng, M. Wang

Cukurova University, Adana, Turkey

A. Adiguzel, M.N. Bakirci⁴¹, S. Cerci⁴², C. Dozen, I. Dumanoglu, E. Eskut, S. Girgis, G. Gokbulut, I. Hos, E.E. Kangal, G. Karapinar, A. Kayis Topaksu, G. Onengut, K. Ozdemir, S. Ozturk⁴³, A. Polatoz, K. Sogut⁴⁴, D. Sunar Cerci⁴², B. Tali⁴², H. Topakli⁴¹, L.N. Vergili, M. Vergili

Middle East Technical University, Physics Department, Ankara, Turkey

I.V. Akin, T. Aliev, B. Bilin, S. Bilmis, M. Deniz, H. Gamsizkan, A.M. Guler, K. Ocalan, A. Ozpineci, M. Serin, R. Sever, U.E. Surat, M. Yalvac, E. Yildirim, M. Zeyrek

Bogazici University, Istanbul, Turkey

M. Deliomeroğlu, E. Gülmez, B. Isildak, M. Kaya⁴⁵, O. Kaya⁴⁵, S. Ozkorucuklu⁴⁶, N. Sonmez⁴⁷

Istanbul Technical University, Istanbul, Turkey

K. Cankocak

National Scientific Center, Kharkov Institute of Physics and Technology, Kharkov, Ukraine

L. Levchuk

University of Bristol, Bristol, United Kingdom

F. Bostock, J.J. Brooke, E. Clement, D. Cussans, H. Flacher, R. Frazier, J. Goldstein, M. Grimes, G.P. Heath, H.F. Heath, L. Kreczko, S. Metson, D.M. Newbold³⁷, K. Nirunpong, A. Poll, S. Senkin, V.J. Smith, T. Williams

Rutherford Appleton Laboratory, Didcot, United Kingdom

L. Basso⁴⁸, A. Belyaev⁴⁸, C. Brew, R.M. Brown, D.J.A. Cockerill, J.A. Coughlan, K. Harder, S. Harper, J. Jackson, B.W. Kennedy, E. Olaiya, D. Petyt, B.C. Radburn-Smith, C.H. Shepherd-Themistocleous, I.R. Tomalin, W.J. Womersley

Imperial College, London, United Kingdom

R. Bainbridge, G. Ball, R. Beuselinck, O. Buchmuller, D. Colling, N. Cripps, M. Cutajar, P. Dauncey, G. Davies, M. Della Negra, W. Ferguson, J. Fulcher, D. Futyan, A. Gilbert, A. Guneratne Bryer, G. Hall, Z. Hatherell, J. Hays, G. Iles, M. Jarvis, G. Karapostoli, L. Lyons, A.-M. Magnan, J. Marrouche, B. Mathias, R. Nandi, J. Nash, A. Nikitenko⁴⁰, A. Papageorgiou, J. Pela¹, M. Pesaresi, K. Petridis, M. Pioppi⁴⁹, D.M. Raymond, S. Rogerson, N. Rompotis, A. Rose, M.J. Ryan, C. Seez, P. Sharp[†], A. Sparrow, A. Tapper, M. Vazquez Acosta, T. Virdee, S. Wakefield, N. Wardle, T. Whyntie

Brunel University, Uxbridge, United Kingdom

M. Barrett, M. Chadwick, J.E. Cole, P.R. Hobson, A. Khan, P. Kyberd, D. Leggat, D. Leslie, W. Martin, I.D. Reid, P. Symonds, L. Teodorescu, M. Turner

Baylor University, Waco, USA

K. Hatakeyama, H. Liu, T. Scarborough

The University of Alabama, Tuscaloosa, USA

C. Henderson, P. Rumerio

Boston University, Boston, USA

A. Avetisyan, T. Bose, C. Fantasia, A. Heister, J. St. John, P. Lawson, D. Lazic, J. Rohlf, D. Sperka, L. Sulak

Brown University, Providence, USA

J. Alimena, S. Bhattacharya, D. Cutts, A. Ferapontov, U. Heintz, S. Jabeen, G. Kukartsev, G. Landsberg, M. Luk, M. Narain, D. Nguyen, M. Segala, T. Sinthuprasith, T. Speer, K.V. Tsang

University of California, Davis, Davis, USA

R. Breedon, G. Breto, M. Calderon De La Barca Sanchez, S. Chauhan, M. Chertok, J. Conway, R. Conway, P.T. Cox, J. Dolen, R. Erbacher, M. Gardner, R. Houtz, W. Ko, A. Kopecky, R. Lander, O. Mall, T. Miceli, R. Nelson, D. Pellett, B. Rutherford, M. Searle, J. Smith, M. Squires, M. Tripathi, R. Vasquez Sierra

University of California, Los Angeles, Los Angeles, USA

V. Andreev, D. Cline, R. Cousins, J. Duris, S. Erhan, P. Everaerts, C. Farrell, J. Hauser, M. Ignatenko, C. Plager, G. Rakness, P. Schlein[†], J. Tucker, V. Valuev, M. Weber

University of California, Riverside, Riverside, USA

J. Babb, R. Clare, M.E. Dinardo, J. Ellison, J.W. Gary, F. Giordano, G. Hanson, G.Y. Jeng⁵⁰, H. Liu, O.R. Long, A. Luthra, H. Nguyen, S. Paramesvaran, J. Sturdy, S. Sumowidagdo, R. Wilken, S. Wimpenny

University of California, San Diego, La Jolla, USA

W. Andrews, J.G. Branson, G.B. Cerati, S. Cittolin, D. Evans, F. Golf, A. Holzner, R. Kelley, M. Lebourgeois, J. Letts, I. Macneill, B. Mangano, J. Muelmenstaedt, S. Padhi, C. Palmer, G. Petrucciani, M. Pieri, R. Ranieri, M. Sani, V. Sharma, S. Simon, E. Sudano, M. Tadel, Y. Tu, A. Vartak, S. Wasserbaech⁵¹, F. Würthwein, A. Yagil, J. Yoo

University of California, Santa Barbara, Santa Barbara, USA

D. Barge, R. Bellan, C. Campagnari, M. D'Alfonso, T. Danielson, K. Flowers, P. Geffert, J. Incandela, C. Justus, P. Kalavase, S.A. Koay, D. Kovalskyi¹, V. Krutelyov, S. Lowette, N. Mccoll, V. Pavlunin, F. Rebassoo, J. Ribnik, J. Richman, R. Rossin, D. Stuart, W. To, C. West

California Institute of Technology, Pasadena, USA

A. Apresyan, A. Bornheim, Y. Chen, E. Di Marco, J. Duarte, M. Gataullin, Y. Ma, A. Mott, H.B. Newman, C. Rogan, V. Timciuc, P. Traczyk, J. Veverka, R. Wilkinson, Y. Yang, R.Y. Zhu

Carnegie Mellon University, Pittsburgh, USA

B. Akgun, R. Carroll, T. Ferguson, Y. Iiyama, D.W. Jang, Y.F. Liu, M. Paulini, H. Vogel, I. Vorobiev

University of Colorado at Boulder, Boulder, USA

J.P. Cumalat, B.R. Drell, C.J. Edelmaier, W.T. Ford, A. Gaz, B. Heyburn, E. Luiggi Lopez, J.G. Smith, K. Stenson, K.A. Ulmer, S.R. Wagner

Cornell University, Ithaca, USA

L. Agostino, J. Alexander, A. Chatterjee, N. Eggert, L.K. Gibbons, B. Heltsley, W. Hopkins, A. Khukhunaishvili, B. Kreis, N. Mirman, G. Nicolas Kaufman, J.R. Patterson, A. Ryd, E. Salvati, W. Sun, W.D. Teo, J. Thom, J. Thompson, J. Vaughan, Y. Weng, L. Winstrom, P. Wittich

Fairfield University, Fairfield, USA

D. Winn

Fermi National Accelerator Laboratory, Batavia, USA

S. Abdullin, M. Albrow, J. Anderson, L.A.T. Bauerdick, A. Beretvas, J. Berryhill, P.C. Bhat, I. Bloch, K. Burkett, J.N. Butler, V. Chetluru, H.W.K. Cheung, F. Chlebana, V.D. Elvira, I. Fisk, J. Freeman, Y. Gao, D. Green, O. Gutsche, A. Hahn, J. Hanlon, R.M. Harris, J. Hirschauer, B. Hooberman, S. Jindariani, M. Johnson, U. Joshi, B. Kilminster, B. Klima, S. Kunori, S. Kwan, D. Lincoln, R. Lipton, L. Lueking, J. Lykken, K. Maeshima, J.M. Marraffino, S. Maruyama, D. Mason, P. McBride, K. Mishra, S. Mrenna, Y. Musienko⁵², C. Newman-Holmes, V. O'Dell, O. Prokofyev, E. Sexton-Kennedy, S. Sharma, W.J. Spalding, L. Spiegel, P. Tan, L. Taylor, S. Tkaczyk, N.V. Tran, L. Uplegger, E.W. Vaandering, R. Vidal, J. Whitmore, W. Wu, F. Yang, F. Yumiceva, J.C. Yun

University of Florida, Gainesville, USA

D. Acosta, P. Avery, D. Bourilkov, M. Chen, S. Das, M. De Gruttola, G.P. Di Giovanni, D. Dobur, A. Drozdetskiy, R.D. Field, M. Fisher, Y. Fu, I.K. Furic, J. Gartner, J. Hugon, B. Kim, J. Konigsberg, A. Korytov, A. Kropivnitskaya, T. Kypreos, J.F. Low, K. Matchev, P. Milenovic⁵³, G. Mitselmakher, L. Muniz, R. Remington, A. Rinkevicius, P. Sellers, N. Skhirtladze, M. Snowball, J. Yelton, M. Zakaria

Florida International University, Miami, USA

V. Gaultney, L.M. Lebolo, S. Linn, P. Markowitz, G. Martinez, J.L. Rodriguez

Florida State University, Tallahassee, USA

T. Adams, A. Askew, J. Bochenek, J. Chen, B. Diamond, S.V. Gleyzer, J. Haas, S. Hagopian, V. Hagopian, M. Jenkins, K.F. Johnson, H. Prosper, V. Veeraraghavan, M. Weinberg

Florida Institute of Technology, Melbourne, USA

M.M. Baarmand, B. Dorney, M. Hohlmann, H. Kalakhety, I. Vodopyanov

University of Illinois at Chicago (UIC), Chicago, USA

M.R. Adams, I.M. Anghel, L. Apanasevich, Y. Bai, V.E. Bazterra, R.R. Betts, J. Callner, R. Cavanaugh, C. Dragoiu, O. Evdokimov, E.J. Garcia-Solis, L. Gauthier, C.E. Gerber, D.J. Hofman, S. Khalatyan, F. Lacroix, M. Malek, C. O'Brien, C. Silkworth, D. Strom, N. Varelas

The University of Iowa, Iowa City, USA

U. Akgun, E.A. Albayrak, B. Bilki⁵⁴, K. Chung, W. Clarida, F. Duru, S. Griffiths, C.K. Lae, J.-P. Merlo, H. Mermerkaya⁵⁵, A. Mestvirishvili, A. Moeller, J. Nachtman, C.R. Newsom, E. Norbeck, J. Olson, Y. Onel, F. Ozok, S. Sen, E. Tiras, J. Wetzel, T. Yetkin, K. Yi

Johns Hopkins University, Baltimore, USA

B.A. Barnett, B. Blumenfeld, S. Bolognesi, D. Fehling, G. Giurgiu, A.V. Gritsan, Z.J. Guo, G. Hu, P. Maksimovic, S. Rappoccio, M. Swartz, A. Whitbeck

The University of Kansas, Lawrence, USA

P. Baringer, A. Bean, G. Benelli, O. Grachov, R.P. Kenny Iii, M. Murray, D. Noonan, V. Radicci, S. Sanders, R. Stringer, G. Tinti, J.S. Wood, V. Zhukova

Kansas State University, Manhattan, USA

A.F. Barfuss, T. Bolton, I. Chakaberia, A. Ivanov, S. Khalil, M. Makouski, Y. Maravin, S. Shrestha, I. Svintradze

Lawrence Livermore National Laboratory, Livermore, USA

J. Gronberg, D. Lange, D. Wright

University of Maryland, College Park, USA

A. Baden, M. Boutemour, B. Calvert, S.C. Eno, J.A. Gomez, N.J. Hadley, R.G. Kellogg, M. Kirn, T. Kolberg, Y. Lu, M. Marionneau, A.C. Mignerey, A. Peterman, K. Rossato, A. Skuja, J. Temple, M.B. Tonjes, S.C. Tonwar, E. Twedt

Massachusetts Institute of Technology, Cambridge, USA

G. Bauer, J. Bendavid, W. Busza, E. Butz, I.A. Cali, M. Chan, V. Dutta, G. Gomez Ceballos, M. Goncharov, K.A. Hahn, Y. Kim, M. Klute, Y.-J. Lee, W. Li, P.D. Luckey, T. Ma, S. Nahn, C. Paus, D. Ralph, C. Roland, G. Roland, M. Rudolph, G.S.F. Stephans, F. Stöckli, K. Sumorok, K. Sung, D. Velicanu, E.A. Wenger, R. Wolf, B. Wyslouch, S. Xie, M. Yang, Y. Yilmaz, A.S. Yoon, M. Zanetti

University of Minnesota, Minneapolis, USA

S.I. Cooper, P. Cushman, B. Dahmes, A. De Benedetti, G. Franzoni, A. Gude, J. Haupt, S.C. Kao, K. Klapoetke, Y. Kubota, J. Mans, N. Pastika, R. Rusack, M. Sasseville, A. Singovsky, N. Tambe, J. Turkewitz

University of Mississippi, University, USA

L.M. Cremaldi, R. Kroeger, L. Perera, R. Rahmat, D.A. Sanders

University of Nebraska-Lincoln, Lincoln, USA

E. Avdeeva, K. Bloom, S. Bose, J. Butt, D.R. Claes, A. Dominguez, M. Eads, P. Jindal, J. Keller, I. Kravchenko, J. Lazo-Flores, H. Malbouisson, S. Malik, G.R. Snow

State University of New York at Buffalo, Buffalo, USA

U. Baur, A. Godshalk, I. Iashvili, S. Jain, A. Kharchilava, A. Kumar, S.P. Shipkowski, K. Smith

Northeastern University, Boston, USA

G. Alverson, E. Barberis, D. Baumgartel, M. Chasco, J. Haley, D. Trocino, D. Wood, J. Zhang

Northwestern University, Evanston, USA

A. Anastassov, A. Kubik, N. Mucia, N. Odell, R.A. Ofierzynski, B. Pollack, A. Pozdnyakov, M. Schmitt, S. Stoynev, M. Velasco, S. Won

University of Notre Dame, Notre Dame, USA

L. Antonelli, D. Berry, A. Brinkerhoff, M. Hildreth, C. Jessop, D.J. Karmgard, J. Kolb, K. Lannon, W. Luo, S. Lynch, N. Marinelli, D.M. Morse, T. Pearson, R. Ruchti, J. Slaunwhite, N. Valls, J. Warchol, M. Wayne, M. Wolf, J. Ziegler

The Ohio State University, Columbus, USA

B. Bylsma, L.S. Durkin, C. Hill, R. Hughes, P. Killewald, K. Kotov, T.Y. Ling, D. Puigh, M. Rodenburg, C. Vuosalo, G. Williams, B.L. Winer

Princeton University, Princeton, USA

N. Adam, E. Berry, P. Elmer, D. Gerbaudo, V. Halyo, P. Hebda, J. Hegeman, A. Hunt, E. Laird, D. Lopes Pegna, P. Lujan, D. Marlow, T. Medvedeva, M. Mooney, J. Olsen, P. Piroué, X. Quan, A. Raval, H. Saka, D. Stickland, C. Tully, J.S. Werner, A. Zuranski

University of Puerto Rico, Mayaguez, USA

J.G. Acosta, X.T. Huang, A. Lopez, H. Mendez, S. Oliveros, J.E. Ramirez Vargas, A. Zatserklyaniy

Purdue University, West Lafayette, USA

E. Alagoz, V.E. Barnes, D. Benedetti, G. Bolla, D. Bortoletto, M. De Mattia, A. Everett, Z. Hu, M. Jones, O. Koybasi, M. Kress, A.T. Laasanen, N. Leonardo, V. Maroussov, P. Merkel,

D.H. Miller, N. Neumeister, I. Shipsey, D. Silvers, A. Svyatkovskiy, M. Vidal Marono, H.D. Yoo, J. Zablocki, Y. Zheng

Purdue University Calumet, Hammond, USA

S. Guragain, N. Parashar

Rice University, Houston, USA

A. Adair, C. Boulahouache, V. Cuplov, K.M. Ecklund, F.J.M. Geurts, B.P. Padley, R. Redjimi, J. Roberts, J. Zabel

University of Rochester, Rochester, USA

B. Betchart, A. Bodek, Y.S. Chung, R. Covarelli, P. de Barbaro, R. Demina, Y. Eshaq, A. Garcia-Bellido, P. Goldenzweig, Y. Gotra, J. Han, A. Harel, S. Korjenevski, D.C. Miner, D. Vishnevskiy, M. Zielinski

The Rockefeller University, New York, USA

A. Bhatti, R. Ciesielski, L. Demortier, K. Goulios, G. Lungu, S. Malik, C. Mesropian

Rutgers, the State University of New Jersey, Piscataway, USA

S. Arora, A. Barker, J.P. Chou, C. Contreras-Campana, E. Contreras-Campana, D. Duggan, D. Ferencek, Y. Gershtein, R. Gray, E. Halkiadakis, D. Hidas, D. Hits, A. Lath, S. Panwalkar, M. Park, R. Patel, V. Rekovic, A. Richards, J. Robles, K. Rose, S. Salur, S. Schnetzer, C. Seitz, S. Somalwar, R. Stone, S. Thomas

University of Tennessee, Knoxville, USA

G. Cerizza, M. Hollingsworth, S. Spanier, Z.C. Yang, A. York

Texas A&M University, College Station, USA

R. Eusebi, W. Flanagan, J. Gilmore, T. Kamon⁵⁶, V. Khotilovich, R. Montalvo, I. Osipenkov, Y. Pakhotin, A. Perloff, J. Roe, A. Safonov, T. Sakuma, S. Sengupta, I. Suarez, A. Tatarinov, D. Toback

Texas Tech University, Lubbock, USA

N. Akchurin, J. Damgov, P.R. Duderov, C. Jeong, K. Kovitanggoon, S.W. Lee, T. Libeiro, Y. Roh, I. Volobouev

Vanderbilt University, Nashville, USA

E. Appelt, D. Engh, C. Florez, S. Greene, A. Gurrola, W. Johns, P. Kurt, C. Maguire, A. Melo, P. Sheldon, B. Snook, S. Tuo, J. Velkovska

University of Virginia, Charlottesville, USA

M.W. Arenton, M. Balazs, S. Boutle, B. Cox, B. Francis, J. Goodell, R. Hirosky, A. Ledovskoy, C. Lin, C. Neu, J. Wood, R. Yohay

Wayne State University, Detroit, USA

S. Gollapinni, R. Harr, P.E. Karchin, C. Kottachchi Kankanamge Don, P. Lamichhane, A. Sakharov

University of Wisconsin, Madison, USA

M. Anderson, M. Bachtis, D. Belknap, L. Borrello, D. Carlsmith, M. Cepeda, S. Dasu, L. Gray, K.S. Grogg, M. Grothe, R. Hall-Wilton, M. Herndon, A. Hervé, P. Klabbers, J. Klukas, A. Lanaro, C. Lazaridis, J. Leonard, R. Loveless, A. Mohapatra, I. Ojalvo, G.A. Pierro, I. Ross, A. Savin, W.H. Smith, J. Swanson

†: Deceased

1: Also at CERN, European Organization for Nuclear Research, Geneva, Switzerland

- 2: Also at National Institute of Chemical Physics and Biophysics, Tallinn, Estonia
- 3: Also at Universidade Federal do ABC, Santo Andre, Brazil
- 4: Also at California Institute of Technology, Pasadena, USA
- 5: Also at Laboratoire Leprince-Ringuet, Ecole Polytechnique, IN2P3-CNRS, Palaiseau, France
- 6: Also at Suez Canal University, Suez, Egypt
- 7: Also at Cairo University, Cairo, Egypt
- 8: Also at British University, Cairo, Egypt
- 9: Also at Fayoum University, El-Fayoum, Egypt
- 10: Now at Ain Shams University, Cairo, Egypt
- 11: Also at Soltan Institute for Nuclear Studies, Warsaw, Poland
- 12: Also at Université de Haute-Alsace, Mulhouse, France
- 13: Now at Joint Institute for Nuclear Research, Dubna, Russia
- 14: Also at Moscow State University, Moscow, Russia
- 15: Also at Brandenburg University of Technology, Cottbus, Germany
- 16: Also at Institute of Nuclear Research ATOMKI, Debrecen, Hungary
- 17: Also at Eötvös Loránd University, Budapest, Hungary
- 18: Also at Tata Institute of Fundamental Research - HECR, Mumbai, India
- 19: Now at King Abdulaziz University, Jeddah, Saudi Arabia
- 20: Also at University of Visva-Bharati, Santiniketan, India
- 21: Also at Sharif University of Technology, Tehran, Iran
- 22: Also at Isfahan University of Technology, Isfahan, Iran
- 23: Also at Shiraz University, Shiraz, Iran
- 24: Also at Plasma Physics Research Center, Science and Research Branch, Islamic Azad University, Teheran, Iran
- 25: Also at Facoltà Ingegneria Università di Roma, Roma, Italy
- 26: Also at Università della Basilicata, Potenza, Italy
- 27: Also at Università degli Studi Guglielmo Marconi, Roma, Italy
- 28: Also at Laboratori Nazionali di Legnaro dell' INFN, Legnaro, Italy
- 29: Also at Università degli studi di Siena, Siena, Italy
- 30: Also at University of Bucharest, Bucuresti-Magurele, Romania
- 31: Also at Faculty of Physics of University of Belgrade, Belgrade, Serbia
- 32: Also at University of Florida, Gainesville, USA
- 33: Also at University of California, Los Angeles, Los Angeles, USA
- 34: Also at Scuola Normale e Sezione dell' INFN, Pisa, Italy
- 35: Also at INFN Sezione di Roma; Università di Roma "La Sapienza", Roma, Italy
- 36: Also at University of Athens, Athens, Greece
- 37: Also at Rutherford Appleton Laboratory, Didcot, United Kingdom
- 38: Also at The University of Kansas, Lawrence, USA
- 39: Also at Paul Scherrer Institut, Villigen, Switzerland
- 40: Also at Institute for Theoretical and Experimental Physics, Moscow, Russia
- 41: Also at Gaziosmanpasa University, Tokat, Turkey
- 42: Also at Adiyaman University, Adiyaman, Turkey
- 43: Also at The University of Iowa, Iowa City, USA
- 44: Also at Mersin University, Mersin, Turkey
- 45: Also at Kafkas University, Kars, Turkey
- 46: Also at Suleyman Demirel University, Isparta, Turkey
- 47: Also at Ege University, Izmir, Turkey
- 48: Also at School of Physics and Astronomy, University of Southampton, Southampton, United Kingdom

49: Also at INFN Sezione di Perugia; Università di Perugia, Perugia, Italy

50: Also at University of Sydney, Sydney, Australia

51: Also at Utah Valley University, Orem, USA

52: Also at Institute for Nuclear Research, Moscow, Russia

53: Also at University of Belgrade, Faculty of Physics and Vinca Institute of Nuclear Sciences, Belgrade, Serbia

54: Also at Argonne National Laboratory, Argonne, USA

55: Also at Erzincan University, Erzincan, Turkey

56: Also at Kyungpook National University, Daegu, Korea